A New Attempt on Measurement of the $^{19}F(p,\alpha)^{16}O$ Reaction Cross Section Towards Elucidating Nucleosynthesis of Fluorine

by

Preetinder Kaur Jassal

A Thesis Submitted to Saint Mary's University, Halifax, Nova Scotia in Partial Fulfillment of the Requirements for the Degree of Doctor of Philosophy in Astronomy (Department of Astronomy and Physics)

2020, Halifax, Nova Scotia

Approved: Dr. Rituparna Kanungo

(Supervisor)

Approved: Dr. Ian Short

(Examiner)

Approved: Dr. Adam Sarty

(Examiner)

Approved: Dr. Chris Ruiz

(External Examiner)

Date: April 21, 2020

Acknowledgements

Thank you, Ritu !

Contents

List of Figures

List of Tables

Abstract

Galactic fluorine abundance is strongly dependent on the conditions in the astrophysical sites. This feature makes it useful to probe different nucleosynthesis scenarios, mainly in the AGB stars. It is also important in understanding s-process elements production and mixing processes in AGB stars. The observed upper limit of fluorine abundance is much lower than the one predicted with most recent AGB models, hinting at some catalytic material activating fluorine destruction via reactions involving fluorine, in particular ^{19}F(p,α)^{16}O. Therefore, it is of vital importance to get an insight into this destruction channel. Despite of its importance, the astrophysical S-factor of this reaction is poorly known from previous studies, at astrophysical energies.

In this work, observations and data analysis on ^{19}F(p,α)^{16}O will be discussed. This reaction was measured in inverse kinematics at the ISAC rare isotope beam facility at TRIUMF. The ^{19}F beam, at mid-target E_{cm} = 2.35 MeV, was impinged on a solid hydrogen target at IRIS spectroscopy station. In an attempt to identify the ground state in ^{16}O, missing mass spectrum technique is used in the analysis.

Chapter 1

Introduction

Where does all the matter in the Universe come from? Everything that we see around us is made up of matter. From times immemorial, humans wished to know more about the universe surrounding them, and in particular, to understand the origin of matter. The matter around us is essentially composed of a great variety of elements and their isotopes. Each isotopic form of an element contains a nucleus which has its own characteristic properties which are different from those of all other nuclei. Protons and neutrons are the building blocks of a nucleus and a nuclear process can be understood as either a rearrangement of nucleons or an interchange of neutrons and protons between reacting nuclei. It is important to keep this picture of the structure and interactions of nuclei of the elements in mind while attempting to explain their origin in nature (M. E. Burbidge et al., 1957)

The elements that we find on Earth today were created in a variety of nucleosyn-

thesis events throughout the history of the universe. Starting from the time of formation of the universe, the Big Bang Nucleosynthesis is thought to have produced mostly the lightest isotope of Hydrogen ^{1}H, most of the universe's Helium ^{4}He, along with small amounts of the hydrogen isotope Deuterium ^{2}H and a very small amount of Lithium ^{7}Li. Essentially all of the elements heavier than Lithium were created much later, by stellar nucleosynthesis, in evolving and exploding stars. Many of these were ejected into the interstellar medium sometime later. In 1936, Atkinson proposed the fusion of two hydrogen nuclei to deuterium as a source of stellar energy generation. Later, it was verified that this reaction gives indeed an energy generation of correct order of magnitude for the Sun (H. A. Bethe and C L. Critchfield, 1938). This confirmation led to the development of the theory that stars undergo nuclear fusion reactions in their cores. This finding also guided towards the idea that these nuclear reactions are a must to synthesize most of the elements, provide energy for stars to shine and determine the evolution of stars. The proton-proton chain of reactions is one of the two sets of fusion reactions by which stars convert hydrogen to helium, dominating in stars with masses comparable to or lesser than that of sun. The other reaction is the CNO cycle which predominantly occurs in stars more massive than 1.5 times the mass of the sun. The energy production in stars via the CNO cycle was independently discovered by von Weizsacker (1938) and Bethe (1939) (C. Illiadis, 2010).

As the understanding progressed with time, it was proposed in theory that once the star has burned its hydrogen fuel completely, gravitational contraction leads to increase in temperature. At this point, the temperature is just enough to ignite the helium which

provides fuel for next burning stages in nucleosynthesis for massive stars. However, this simple formulation in theory did have to face challenges. The helium burning faced a hindrance because it was firmly established at that time that no stable nucleus of mass number 5 or 8 existed, so how nature bypasses that gap was a mystery in itself. In 1951, Saltpeter came to rescue and suggested that unstable ^{8}Be could capture another alpha to form stable ^{12}C, and named this process "triple alpha reaction". Adding to this, Hoyle suggested the existence of a resonant state which would enhance the triple alpha process. Later, this state was experimentally verified at 7.654 MeV, thus establishing the triple alpha reaction as the mechanism to overcome the gaps due to mass numbers 5 and 8. In the late 1950s, thanks to the pioneering work of M. E. Burbidge et al., 1957 (the famous B^2FH), the basic principles of explaining the origin of the elements in the stars were laid down in the theory of nucleosynthesis, explaining the mechanism for synthesis of elements heavier than Nickel. Nuclei heavier than mass number $A > 60$ require different mechanism because the higher Coulomb barrier hinders fusion of charged nuclei. Therefore, the heavier elements were proposed to be synthesized by neutron capture via two distinct processes i.e. s-process and r-process. First, neutrons react with stable seed nuclei until a number of these neutrons have been captured creating unstable isotopes. The subsequent beta decays of these isotopes increase the atomic numbers making further neutron captures possible to create heavier elements. The s-process creates roughly half of the elements heavier than iron and the other half are created in the r-process. As of today, we have unambiguous direct evidence for the nucleosynthesis in stars mainly the observation of radioactive Technetium, ^{99}Tc, in stellar spectra. This s-process element serves as a direct observational evidence of a new heavy

element produced in a star (P. W. Merrill, 1952). In addition to this, gamma rays from radioactive ^{26}Al were also discovered in the interstellar medium by spectrometers on-board satellites (W. A. Mahoney, et al., 1982). These events corroborate the postulates of the nucleosynthesis theory (R. Diehl et al., 1995, 2006). While the astrophysical site(s) of the r-process is not yet completely known, it must occur in environments with such large neutron densities that very exotic neutron-rich nuclei are created. Thousands of nuclei are believed to be involved in the r-process, and their properties and reaction/decay rates determine the final abundances that are produced. The exact sites of the r-process are an active area of research. On the other hand, the s-process is proposed to occur in Asymptotic Giant Branch (AGB) stars and helium cores of massive stars. The primary source of neutrons in the s-process are the reactions ^{13}C(α,n)^{16}O and ^{22}Ne(α,n)^{25}Mg.

A deeper understanding of the nucleosynthesis in the framework of stellar evolution can be gained by getting an insight into the stellar composition at a given time of interest. If a star consists exclusively of hydrogen and helium, significant energy can only be generated during the hydrogen burning stage via the operation of the p-p chain of reactions. Most stars consist of gas that contains heavier nuclides, particularly those in C, N, and O mass region. Hence, these heavier nuclei can participate in hydrogen burning too, such processes are named as CNO cycles. There are 4 CNO cycles and the end result of each process is the same as for the p-p chains i.e. $\mathrm{H} \rightarrow \mathrm{He}$ with each of C, N, O or F nuclei acting as catalysts. The various CNO cycles exist because for the proton-induced reactions on the nuclei ^{15}N, ^{17}O, ^{18}O and ^{19}F both the (p,γ) and (p,α) channels are energetically allowed, in contrast to

the proton-induced reactions on the nuclei ^{12}C, ^{13}C, ^{14}N, and ^{16}O that can only proceed via the (p,γ) reaction. The reactions of the four CNO cycle are shown in Figure 1.1

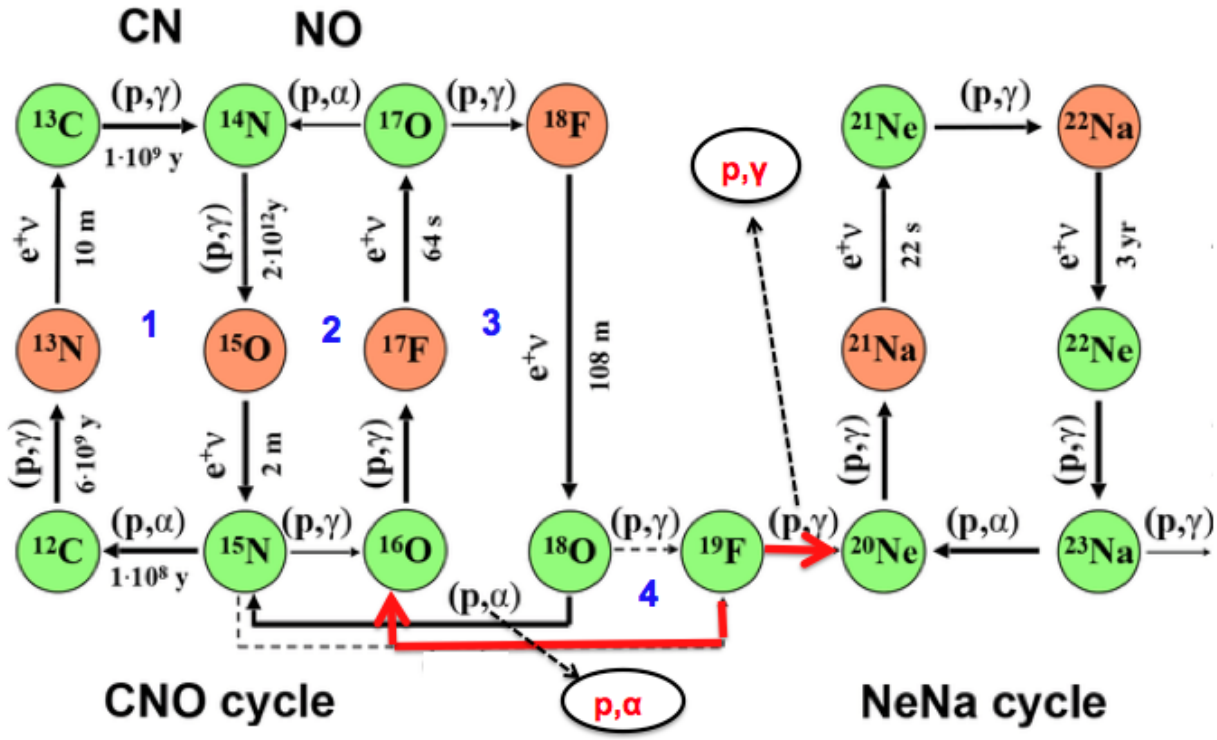

Figure 1.1: Representation of the four CNO cycles. Each reaction cycle effectively fuses four protons to one ^{4}He nucleus (Figure adapted from A. Boeltzig et al., 2015)

Figure 1.1 shows how the reactions flow in the CNO cycles. CNO1 corresponds to the CN cycle, the main energy producing cycle. CNO2, with CNO3 together form the CNO bicycle. CNO3 and CNO4 are much slower than the bicycle, but when activated, do affect the abundances of the nuclei involved i.e. they tend to destroy ^{18}O and ^{19}F. The (p,α) reaction will convert a heavier nucleus back to a lighter one, thereby giving rise to a cycle of nuclear processes. At each of the branch point nuclei ^{15}N, ^{17}O, ^{18}O, and ^{19}F, the

(p,α) reaction competes with the (p,γ) reaction. The last branch point (p,α) plays a crucial role because it acts as a branching point between CNO cycles and the NeNa one, and the amount of catalytic material, ^{19}F, that is lost from CNO cycles to activate the NeNa one is regulated by the competition between the ^{19}F(p,α) and ^{19}F(p,γ) reactions.

The low temperature NeNa cycle proceeds via the reaction sequence

$$^{20}\mathrm{Ne(p,}\gamma)^{21}\mathrm{Na(e}^{+},\nu)^{21}\mathrm{Ne(p,}\gamma)^{22}\mathrm{Na(e}^{+},\nu)^{22}\mathrm{Ne(p,}\gamma)^{23}\mathrm{Na(p,}\alpha)^{20}\mathrm{Ne}$$

The cycle is closed because of the β^{+} waiting points at ^{21}Na and ^{22}Na, and also because of the fact that the ^{23}Na(p,α)^{20}Ne reaction is more probable than the ^{23}Na(p,γ)^{24}Mg reaction at low temperatures. At still higher temperature, the ^{23}Na(p,γ)^{24}Mg reaction becomes faster than the ^{23}Na(p,α)^{20}Na reaction (M. Arnould et al., 1999). When this happens, the NeNa cycle leaks into the MgAl cycle which proceeds via the sequence,

$$^{24}\mathrm{Mg(p,}\gamma)^{25}\mathrm{Al(e}^{+},\nu)^{25}\mathrm{Mg(p,}\gamma)^{26}\mathrm{Al(e}^{+},\nu)^{26Mg}\mathrm{(p,}\gamma)^{27}\mathrm{Al(p,}\alpha)^{24}\mathrm{Mg}$$

This reaction is also closed by (p,α) reaction, which competes with a (p,γ) reaction at higher temperatures, where the possibility of breakout from the cycle becomes likely. Figure 1.2 shows two solid lines in the panel which represent the currently accepted upper and lower limits of the branching ratio $B_{p\alpha}/_{p\gamma}$ i.e. the ratio of probabilities of the occurrence of the (p,α) and (p,γ) reactions. This is given by the ratio of the corresponding reaction rates as $B_{p\alpha}/_{p\gamma} = \mathrm{N}_A\langle\sigma\mathrm{v}\rangle_(p,\alpha)/N_A\langle\sigma\mathrm{v}\rangle_(p,\gamma)$

The area between the solid lines represents the uncertainty in $B_{p\alpha}/_{p\gamma}$ that is caused

by unknown contributions to the (p,α) and (p,γ) reaction rates (C. Iliadis, 2010).

By modeling of the nuclear reaction rates, one can gain an insight into multiple simultaneous processes contributing to the abundance of nuclear species and therefore also, evolution of a star. In general, the time evolution of the abundance of a given isotope can be described by a sum of 'source' and 'sink' terms. The sink terms result from processes such as nuclear decay or photodisintegration that destroy a given species while source terms represent nuclear reactions that create it or nuclear decays that might produce it. In a formal manner, the abundance of a given nuclide $'i'$, is given as

$$Y_i = N_i M_i / \rho N_A$$

where, N_i is the number density of the ith isotope, ρ is the total mass density at the point of interest, and N_A is Avogadro's number i.e the number of atoms of species i which makes M_i grams. The time evolution of the abundance can then be described as

$$dY_i/dt = \rho N_A(-\sum_j Y_i Y_j < \sigma v >_{ij} + \sum_l Y_l Y_k < \sigma v >_{lk} - Y_i \lambda_i(\beta) + Y_m \lambda_m(\beta))$$

where the sum includes all the nuclear transformations creating or destroying nucleus i. The first term has a velocity-averaged cross section $< \sigma v >$ represents the two-body reactions destroying the nucleus i, and the second term is a sum over all two-body reactions

leading to formation of nucleus i. The next two terms show the production and destruction of nuclei i with λ describing β-decay constant. These reaction rates only depend on the abundance of a single nuclide e.g. decays and photodisintegration (D. W. Bardayan, 2016).

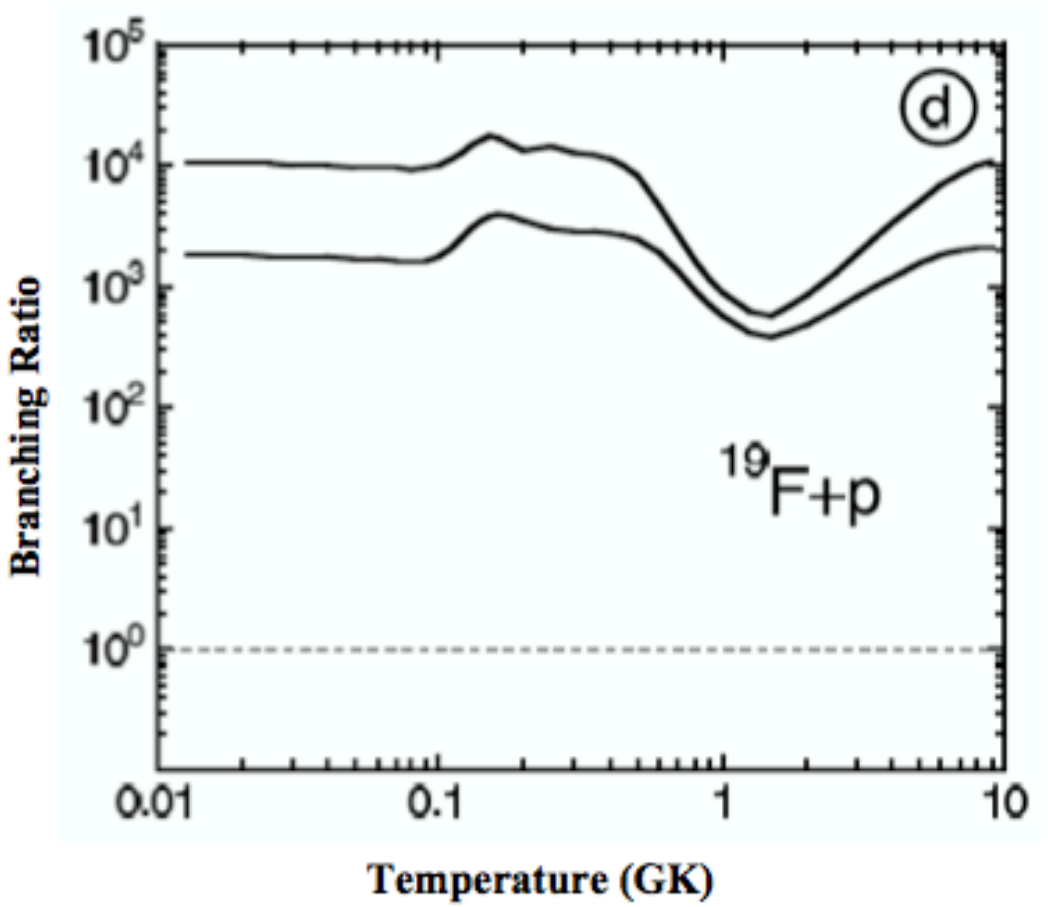

Figure 1.2: Branching Ratio $B_{p\alpha}/_{p\gamma}$ vs temperature for the reaction ^{19}F +p. The area between the solid lines represents the uncertainty in $B_{p\alpha}/_{p\gamma}$, caused by unknown contributions to the respective reaction rates. (Figure adapted from C. Iliadis, 2010)

1.1 Motivation For this Work

Fluorine is a key element for astrophysics. Its abundance is very sensitive to the physical conditions within stars and for the same reason it becomes useful as a probe to understand its nucleosynthesis scenarios (S. Lucatello et al., 2011). The production and destruction of the only existing stable isotope of fluorine, ^{19}F, is deeply connected to the environment and physical conditions in stars. Therefore, fluorine abundances place a very strong constraint on the stellar structure and stellar evolution (I. Indelicato et al., 2017). Fluorine is one of the few chemical elements whose nucleosynthesis origin is still much debated, primarily because of two reasons. Firstly, due to the fragility of the nuclide, which is readily destroyed by proton or alpha captures in stellar interiors (C. Abia et al., 2015). Secondly, due to difficulty of observing of fluorine in stellar spectra due to lack of accessible atomic and molecular lines in the region in the spectrum, suitable for abundance studies (A. Jorissen et al., 1992). Several sites and mechanisms for the production of fluorine have been proposed. The most likely environments where the production of fluorine can take place are - during core collapse of Type-II supernovae, in Wolf-Rayet stars, and in Asymptotic Giant Branch (AGB) stars. Out of all these proposed scenarios, however, the direct proof of fluorine production has only been in AGB stars via spectroscopic detections of [F/Fe] enhancements (A. Jorissen et al. 1992; C. Abia et al. 2009, 2010, 2015).

From an observational point of view, the stars can be divided into groups based on optical spectra. Those stars in which TiO bands dominate are classified as M stars; if C2 or CN bands dominate then the star is a C (carbon) star. If together with TiO bands, molecular

features associated with ZrO are found as well, the star is of type MS. If the molecular features of ZrO dominate over TiO, then the star is classified as of type S. For a star to be of type SC, it must display strong sodium D lines and no ZrO lines. In 1992, A. Jorissen et al., provided the first evidence of fluorine production in AGB stars. They determined the fluorine abundances from infrared rotational-vibrational lines of molecule HF, in stars of near solar metallicity, in giants of type M, MS, S and K and a couple of cool barium stars, SC, N and J stars. They used the lines of this molecule to measure fluorine abundances outside the solar system for the first time. This study found very high ^{19}F surface enrichments (upto 30 times solar) in N-type C stars and a clear correlation between the C/O ratio and fluorine enhancement. This suggested the He-burning site, where carbon is produced by the triple alpha reaction, to be same as where fluorine is synthesized. While these N-type C stars are low-mass stars close to the AGB stars, this occurrence was accepted as a clear evidence of fluorine synthesis by AGB stars. Through the correlation with the abundance of carbon, it was established that AGB stars are indeed producers of flourine. These observations not only confirmed that fluorine is produced in a He-burning site but were also able to constrain models of AGB stars. AGB stars are among the most significant polluters of the interstellar medium because they eject both light (C, N, F, Na) and heavy elements. Up to now, theoretical models overproduce fluorine abundances in AGB stars with respect to the observed values (I. Indelicato et al., 2017). Although those differences are small at solar metallicity, low metallicity AGB stellar models predict fluorine surface abundances up to one order of magnitude larger than the observed ones (S. Cristallo et al., 2014). This could possibly be coming from discrepancy in reactions involving fluorine, thus calling for further

experimental investigation of the reactions involving fluorine. Because nucleosynthesis in the framework of stellar evolution is an active research field, it is worthwhile to keep in mind the uncertainties in the model calculations. These reflect our incomplete knowledge of certain processes in stars, including the treatments of energy transport via convection, mass loss, and mixing. Nonetheless, nuclear reaction rates are important ingredients in nucleosynthesis models. In particular, ^{19}F(p,α)^{16}O reaction is the main destruction channel of fluorine in proton-rich environments in AGB stars. If the hydrogen burning of ^{19}F proceeds predominantly through ^{19}F(p,α)^{16}O reaction, the CNO catalytic material will remain in the cycle, leading to the fourth branch cycle in CNO hydrogen burning (I. Lombardo et al., 2014). This reaction closes the CNOF cycle in the hydrogen-burning phase of massive stars.

$$^{16}\mathrm{O(p,}\gamma)^{17}\mathrm{F}(\beta^{+},\nu)^{17}\mathrm{O(p,}\gamma)^{18}\mathrm{F}(\beta^{+},\nu)^{18}O(\mathrm{p,}\gamma)^{19}\mathrm{F(p,}\alpha)^{16}\mathrm{O}$$

This reaction, in fact, represents the branching point between CNO cycles and the NeNa one. On the other other hand, if the competing reaction ^{19}F(p,γ)^{20}Ne cannot be neglected, the CNO catalytic material will be lost completely through this reaction. In this scenario, various CNO cycles could eventually cease to be an energy source in hydrogen burning. This implies that the amount of catalytic material that is lost from the CNO cycles to activate the NeNa one is regulated by the competition between the ^{19}F(p,α) and ^{19}F(p,γ) (C. Rolfs and W. S. Rodney, 1988)

The main focus of this research, therefore, is to constrain the nuclear physics input for ^{19}F(p,α)^{16}O. This reaction is the main destruction channel of fluorine destruction in AGB

stars (K. Syprou et al., 2000). Nevertheless, fluorine is an element far from being abundant in nature. This readily indicates that either fluorine is very hard to nucleosynthesize or it is extremely fragile in stellar environments.

The aim of this work is to constrain the $^{19}F(p,\alpha)^{16}O$ reaction cross section. This is done by a direct measurement of the reaction in the laboratory, by observing the alpha particles and is combined with nuclear reaction theory to derive the unobserved fraction of the reaction product.

1.1.1 The AGB star scenario - Evolution of a star to AGB Phase

Observational evidence tells that there is a direct correlation between the mass and luminosity of a star, which in turn is also related to the surface temperature of the star. The correlation of stellar luminosity and effective surface temperature of a star can be studied pictorially by constructing a Hertzsprung-Russel (H-R) Diagram, or a color-magnitude diagram. The latter name comes from the fact that surface temperature can be expressed in terms of the color of the star, while luminosity is related to the absolute visual magnitude. The vast majority of stars occupy different areas on the plot based on their properties, mainly initial mass. Figure 1.3 shows the color-magnitude diagram for globular cluster M3. Theoretical models of stars are constructed in the simplest case by solving a set of four partial differential equations, for radius, luminosity, pressure, and temperature, that describe the structure of a star as a function of the distance from the center and as a function of time. It is known at this point that energy is generated in the stars via nuclear reactions

and gravitational contraction, and energy is lost from stellar surface via emission of photons. These particles become the light that astronomers receive from a star, thus providing information on the stellar interiors. The temperature of the atmospheric layers from which these photons escape determines the features of the star's spectrum. Due to gravitational contraction, when the central temperature in the star reaches several million kelvin, the fusion of hydrogen to helium starts to occur and contributes an increasing fraction to total energy output. The star, at this point, is said to be in hydrostatic and thermal equilibrium. The location of a star in the H-R Diagram is at the Zero Age Main Sequence (ZAMS). The evolution of star from ZAMS to AGB phase is highly dependent on both the initial mass and metallicity.

A low mass star of 1 $M_{\odot}$ burns hydrogen into helium in the central core while being on the Main Sequence (MS). Due to the increasing mean molecular weight in the core, the density of the core rises. Due to this increase in the density, the temperature rises with it. When the hydrogen is completely burned into helium in the core, the core starts growing by burning hydrogen in a shell around it but the density keeps increasing until the central core becomes partially electron degenerate. Matter becomes degenerate at relatively high densities because of the Pauli Exclusion Principle. A degenerate gas strongly resists further compression because electrons cannot move into lower energy levels that are already occupied. Unlike an ideal gas (classical), the pressure exerted by a degenerate gas is independent of temperature. In a normal gas, the extra energy release would cause an expansion. That is a star's mechanism to adjust to an increase of energy in their interior;

allowing them to stabilize. In a degenerate gas, the increase in temperature does not affect the pressure. Since the core is composed of degenerate gas, even if the temperature inside the core is continuously increasing, the pressure there is unaffected. The outer layers of the star still have classical behaviour. At this point, the outer layers of the star respond to the increasing temperature in the core by expanding and cooling down; they become convective and star leaves the main sequence at this point to go to Red Giant Branch (RGB) i.e. MS into RGB. At this point, depending on the mass of the star, the star evolution can proceed in a number of ways. A succession of core ignition, core exhaustion, contraction and reheating phases can occur, burning the ashes of the previous burning stage until an onion-skin-like structure is reached. The heaviest product which is synthesized in this process, inside the stars, again depends on the mass, but the absolute endpoint is the synthesis of iron, as beyond this mass, all possible reactions are endothermic i.e they consume energy. It is important to mention here that, in general, a normal star radiates energy which is produced by nuclear reactions in the interior. This energy is transported outward by convection and radiation, driven by the temperature gradient inside the stars. In radiative transfer, energy is transported without any material motion. Convection, on the other hand, involves up and down motions of the gas. Once the convective envelope deepens, it reaches into layers that have been partially processed by hydrogen burning. This pulls the material to the surface, altering the surface composition. Such events are named as dredge-ups, named so, as these dredge (bring up/drag) the products from the core. In other words, a dredge-up is a period in the evolution of a star where a surface convection zone extends down to the layers where material has undergone nuclear fusion. As a result, the fusion products are mixed into the

outer layers of the stellar atmosphere where they can appear in the spectrum of the star. When convective region in the star extends down to the upper

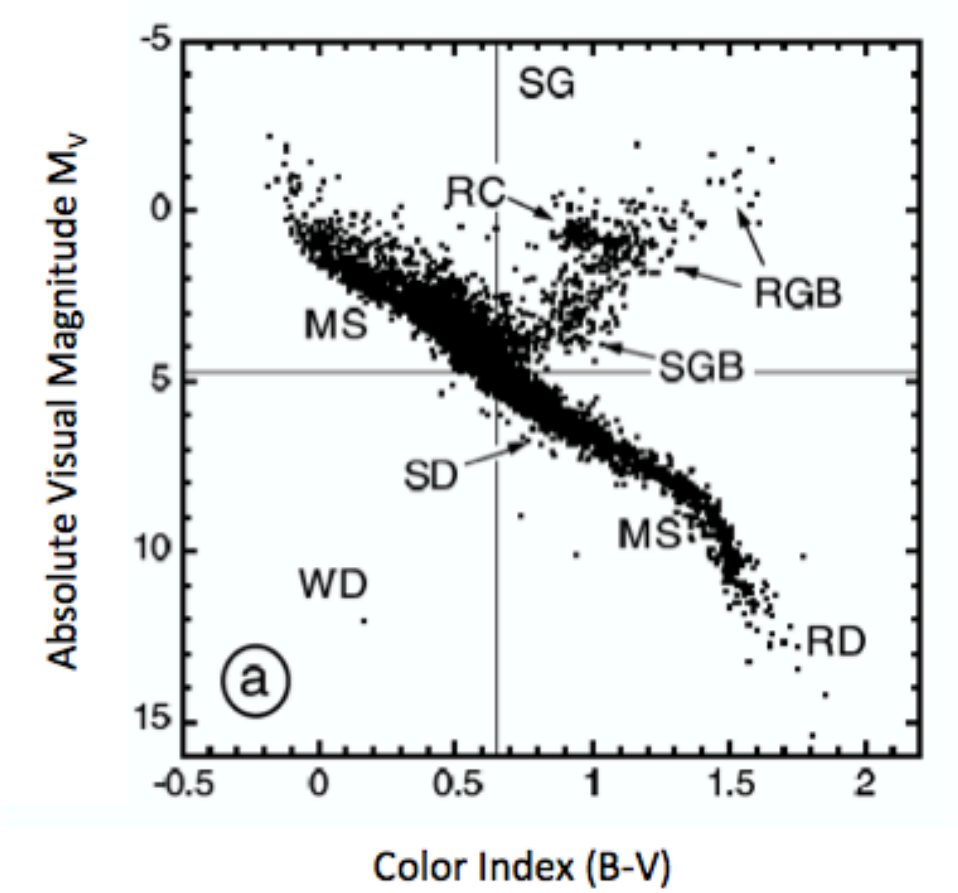

Figure 1.3: Color-Magnitude Diagram showing absolute magnitude on the y-axis versus color index on the x-axis, for globular cluster M3. (Figure adapted from C. Iliadis, 2010)

layers of the helium-rich region, some of the nuclei produced from hydrogen burning such as ^{4}He, ^{13}C, and ^{14}N are then moved up to the stellar surface. This event is called the first dredge-up. The first dredge-up occurs when a main-sequence star enters the red-giant branch. The He-rich core is inert at this time of evolution but keeps contracting and heating. The core becomes electron degenerate and will not cool down by expanding so the temperature rises dramatically and He-burning is ignited (S. C. Yoon et al., 2004).

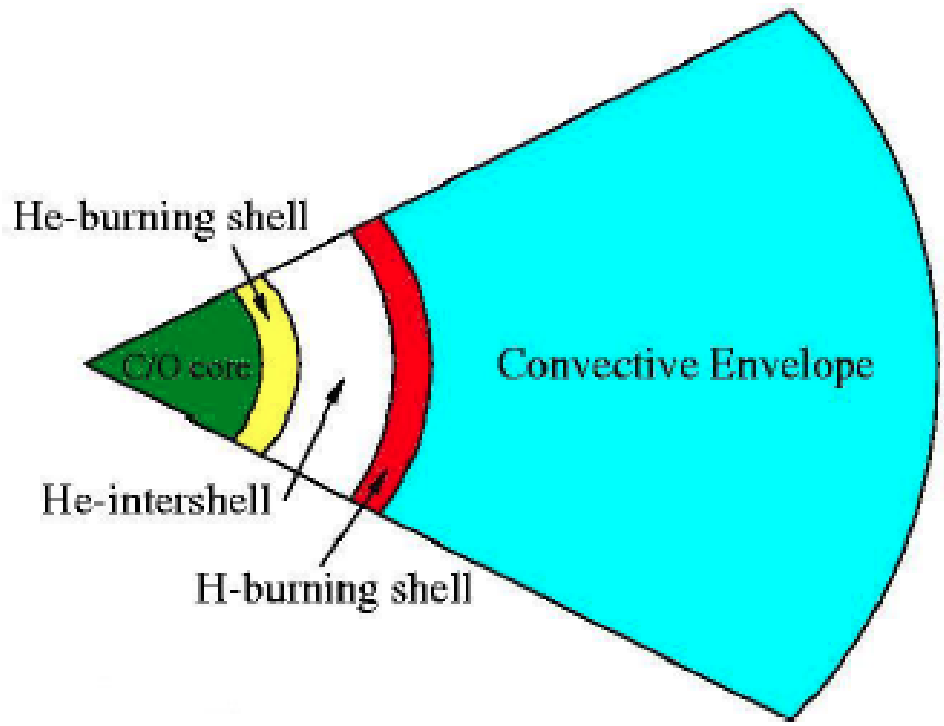

Figure 1.4: Structure of a 7 $M_{\odot}$ star in the AGB phase (Figure adapted from R. J. Stancliffe Thesis, 2005)

The core undergoes a partial thermonuclear runaway and hence the star flashes, or in simpler words, thermal pulse occurs.

After the flash the star cools down and starts burning helium in a convective core and hydrogen in a shell around it. When the helium is exhausted in the core, the star expands its envelope and increasing its luminosity again. The C-O core becomes electron degenerate and, the star now burns nuclear fuel in two shells, helium in a shell surrounding the carbon-oxygen core, and hydrogen in a shell surrounding the helium burning region. The two shells are separated by an intershell consisting mainly of helium. The star then enters the asymptotic giant branch phase (AGB).

A star with a higher mass ($>4M_{\odot}$), behaves different as after the first dredge-up He-burning establishes at its center in non-degenerate conditions with a hydrogen-burning shell above the core. Once the helium is exhausted in the core, it starts burning in a shell outside of core. When helium fusion comes to an end at the core, convection mixes the products of the CNO cycle. This event is called second dredge up and it results in an increase in surface abundance of ^{4}He and ^{14}N. After the second dredge-up the hydrogen shell reignites and the star progresses in the AGB phase. At this point, the structure of an AGB star can be understood as composed of an electron degenerate carbon-oxygen (C-O) core. Above the core is a He-burning shell, an intershell, and a H-burning shell. Finally, the outermost layer of the star is the convective envelope. Figure 1.4 shows the structure of a star in AGB phase with different evolutionary layers shown.

The intershell is an interesting site where rich and diverse nucleosynthesis occurs. While the intershell is a site for both He-burning and H-burning, at the same time, it is thin enough for the temperature to increase without any change in pressure. This property makes

the intershell a very unstable region, hence, the stars starts pulsating (M. Schwarzschild R. Harm, 1965). An increase in temperature will cause the rate for the triple alpha reaction to go up abruptly. For a shell source to become thermally unstable, two requirements must be fulfilled. First, if the energy from the nuclear burning is dumped into the shell, then the temperature must rise. Second, the increased radiative loss due to the raising of the shell temperature must not carry energy away from the shell faster than it is being generated. If both these conditions are satisfied, then the temperature in the shell continues to build up and a thermonuclear runaway results. A higher rate for triple alpha reaction means more energy is produced in the intershell, which in effect leads to an increase in temperature gradient. It happens until energy is dumped in the intershell faster than the rate at which it is lost. Radiation is not that effective and enough cooling is not achieved. So convection starts, the region becomes unstable and a pulse is triggered. After this pulse generation, the region becomes radiative again, and this time the convective envelope penetrates the upper region of the intershell. Infact, as the pulses become more and more violent, the convective envelope of the star moves deeper and deeper into the star as it recovers from each thermal pulse. This deepening of the envelope brings out the freshly made nuclei to the surface of the star, called Third Dredge Up (TDU) (I. Iben, 1975, 1976). The TDU is repeated several times as hydrogen is brought down to a hotter region where it can be burned, starting the heating up of the region all over again. Third dredge up is an extremely important process as it allows material processed by nuclear reactions in the depths of a star to reach the surface where they can be observed and also returned to the interstellar medium via mass loss. This dredge-up causes helium, carbon and the s-process elements be brought to the

surface. This results in an increase in the abundance of carbon relative to oxygen, which can create a carbon star. Because of the recurring nature of thermal pulses TDUP can possibly happen multiple times over and so greatly influence the composition of the star. AGB stars are a fascinating and complex phase of evolution that some stars pass through towards the end of their lives. An unstable arrangement of two thin burning shells, one of helium and one of hydrogen, leads to interesting periodic behavior and rich nucleosynthesis. This makes AGB stars a valuable area of study from the point of view of Galactic Chemical Evolution (C. Iliadis, 2010)

There are still open questions linked to the nuclear physics in the stellar evolution modeling. The uncertainties due to nuclear physics are linked with the rates of reactions. As for the impact of uncertainties owing to stellar evolution modeling, the determination of the size of the convective core and, more in general, of the mixing regions represents one major source of uncertainties. Because the deep-convective mixing episodes taking place during the third dredge-up brings material from the intershell up through the hydrogen burning shell, the nucleosynthesis of certain species can be affected by both regions. For example, ^{19}F can be synthesized by the intershell by the He burning but may also be destroyed via the ^{19}F(p,α)^{16}O reaction at the branching point. The highest values of the observed ^{19}F enhancements in the stellar atmosphere are not matched by standard AGB models and require additional mixing, since the original fluorine at the surface can be brought down to depth where it is destroyed. This discrepancy requires a revision of the nuclear reaction rates involved in the production and destruction of fluorine in AGB stars. This might provide

an alternative explanation for the known inconsistencies between model predictions and observations.

1.1.2 Nucleosynthesis in AGB stars

With the occurence of TDUP process, AGB stars offer a prospect that material synthesized during thermal pulses could be brought to the surface where it might be observed. With the existence of complex nucleosynthesis, AGB stars become a valuable area of study from point of view of Galactic Chemical Evolution (I. Iben, 1975). The intershell of an AGB star is a rich site for the nucleosynthesis of light elements. It was in 1989, when Goriely et al. proposed that AGB stars could be a site for the synthesis of ^{19}F, providing a hint on possible origin of of this element. Because TDUP brings material from the intershell up through the hydrogen burning shell, the nucleosynthesis of certain species can be affected by both regions. It is important to mention here that ^{19}F is synthesized in the intershell by He burning as outlined above but may also be destroyed in the H shell via the reaction ^{19}F(p,γ)^{20}Ne (M. Forestini et al., 1992). In addition to the nucleosynthesis of light elements, AGB stars are also the site for the production of the s-process elements. There have been many attempts to explain the origin of Galactic fluorine but due to the lack of observational data, most of them remain inconclusive. Because of the long timescales involved for a full thermal pulse cycle, no direct observation of an AGB star undergoing a thermal pulse has ever been made.

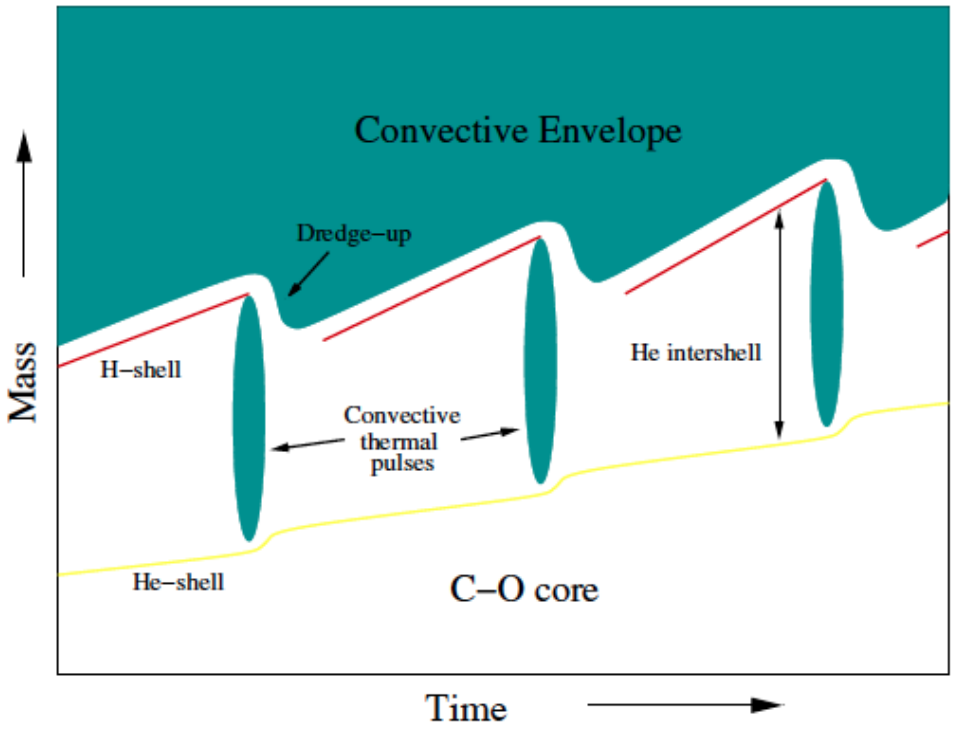

Figure 1.5: Representation of the evolution of the interior of a TP-AGB star of 7 $M_{\odot}$, showing thermal pulses and third dredge-up. Convective regions are shown in green, hydrogen burning shell is the red line and the helium burnig shell is the yellow line, (Figure adapted from R. J. Stancliffe Thesis, 2005)

1.1.3 Production of Fluorine in AGB stars

Fluorine nucleosynthesis in AGB stars takes place in the intershell region where ^{14}N from CNO cycle captures a ^{4}He from the He-rich environment. The resultant nucleus is ^{18}F which decays to ^{18}O . At this point, ^{18}O could capture a proton or a ^{4}He nucleus. If a proton is captured, a ^{15}N and an alpha particle is produced. When ^{15}N captures an alpha particle, fluorine is produced, via the chain as shown below

$^{14}\mathrm{N}(\alpha,\gamma)^{18}\mathrm{F}(\beta^{+})^{18}\mathrm{O}(\mathrm{p},\alpha)^{15}\mathrm{N}(\alpha,\gamma)^{19}F$

The most efficient mechanism for the production of protons is the ^{14}N(n,p)^{14}C reaction. The neutrons required for this reaction come from $^{13}\mathrm{C}(\alpha,\mathrm{n})^{16}O$. Mowlavi (N. Mowlavi et al., 1996) found that massive AGB stars will not produce large fluorine abundances. In addition, they found that low metallicity stars have less fluorine dredged up to the surface than solar metallicity stars. The formation of the ^{13}C-rich region is one of the most important and interesting problems in AGB stellar structure. It is postulated that during the third dredge up the protons are brought into the helium intershell and eventually lead to the making of ^{13}C as $^{12}\mathrm{C}(\mathrm{p},\gamma)^{13}\mathrm{N}(\beta,\nu)$ where ^{12}C originally comes from helium burning. The abundance of ^{19}F is determined by the reaction rates associated with this rather complex production path and by the ^{19}F destruction reaction in the helium intershell (H. Jonsson et al., 2017).

1.1.4 Summary of previous measurements of $^{19}\mathrm{F}(\mathrm{p},\alpha)^{16}\mathrm{O}$

There has been a considerable effort in the determination of the $^{19}\mathrm{F}(\mathrm{p},\alpha)^{16}O$ nuclear reaction rate. Until past few years, the low-energy values of $^{19}\mathrm{F}(\mathrm{p},\alpha)^{16}O$ astrophysical factor $S(E)$ have been collected in NACRE (Nuclear Astrophysics Compilation of Reaction Rates) and came from several works as a mix of absolute and normalized data at a broad energy range of E_{cm} = 0.2 MeV to 3.3 MeV. However, there were large ambiguities present in the $S(E)$ that needed to be clarified.

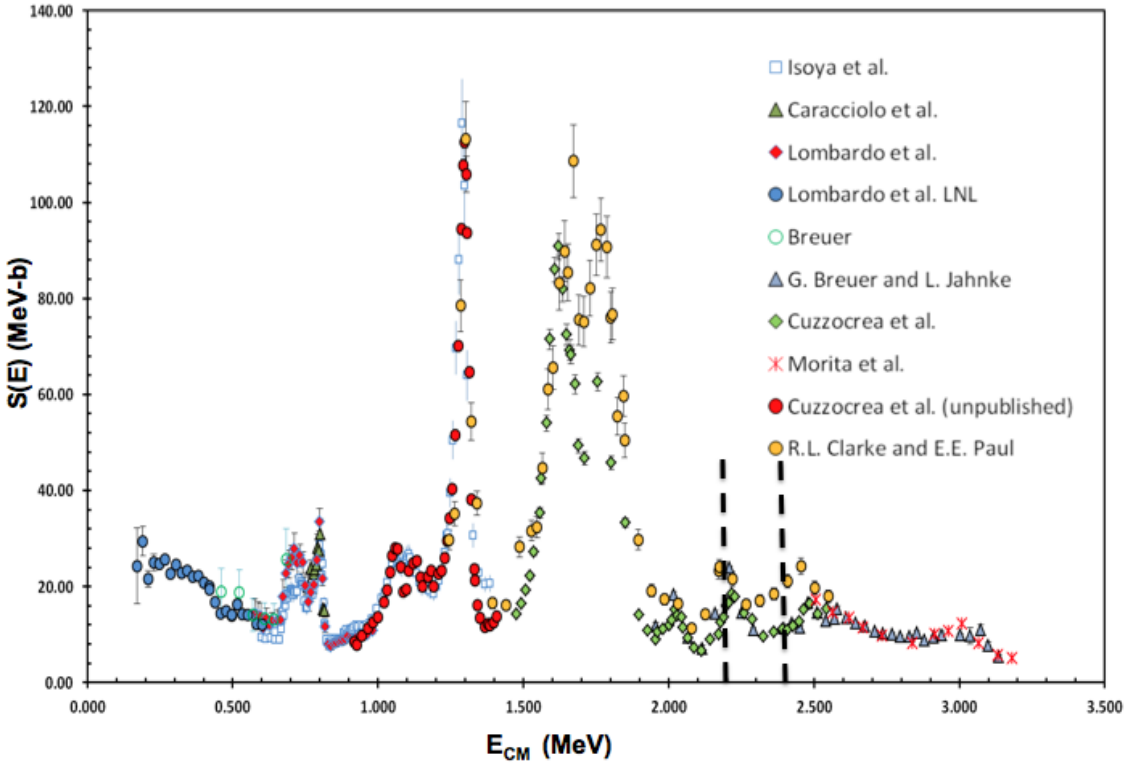

Figure 1.6: ^{19}F(p,α)^{16}O S-factor direct experimental data sets in the 0.2 MeV - 3.3 MeV energy range. (Figure adapted from D. Dell'Aquila and I. Lombardo, 2016)

Figure 1.6 is a pictorial representation of the variation in $S(E)$ with energy from all the data sets reported so far (A. Isoya et al., 1959, R. Caracciolo et al., 1974, I. Lombardo et al., 2014, 2015, G. Breuer et al., 1959, 1964, P. Cuzzocrea et al., 1980, S. Morita et al., 1986, R. L. Clarke and E. E. Paul, 1957).

In the lower end of the energy range measured so far i.e. proton beam energy from 0.630 MeV to 1.460 MeV, the data was reported by Isoya et al., 1959 as shown in blue squares. This data has been normalized by NACRE at the E_p = 1.3 MeV resonance and readily agrees with the data from R. Caracciolo et al., 1974 at a particular energy of E_{cm} = 0.842 MeV as shown in green triangles. However, it disagrees at lower energies with the data reported by G. Breuer et al., 1959, shown as light blue open circles. This disagreement led to large uncertainties in the S-factor extrapolation down to the Gamow Peak, roughly of the order of 50 percent.

Overlapping with our energy of interest i.e. at E_{cm} = 2.35 MeV, the data reported in the energy range E_{cm} = 1.5 - 2.5 MeV have a presence of considerable differences. In this energy range, the relative data by R. L. Clarke and E. B. Paul, 1957 and the absolute data by P. Cuzzocrea et al., 1980 are reported. These data points are shown as yellow points and green diamonds in the figure respectively. These two data sets found the value of $S(E)$ as to be 18.95 MeV-mb and and 9.95 MeV-mb, respectively. As discussed before, this huge discrepancy called for a reassessment of the ^{19}F(p,α)^{16}O reaction rate. In the present work, these efforts are continued as an attempt to reducing the uncertainties on deduced astrophysical S-factor.

1.2 The Rates of Reaction Relevant to Fluorine Synthesis

In this section, a summary of the nuclear reactions and rates relevant to the nucleosynthesis of fluorine production will be discussed. An account of the basic equations of stellar structure will be established by assuming the star to be spherically symmetric. Based on observational data, it has been established that various quantities pertaining to stars have some relations amongst each other. For example, if a star is more massive, then it has a higher luminosity and a higher surface temperature, true for dwarf stars on the main-sequence. As soon as a star evolves off the main-sequence, it becomes more luminous than more massive main-sequence stars and the correlation among mass and luminosity is lost for evolved and post main sequence (evolved) stars. To explain such observed relations theoretically, it is important to understand the fundamental equations which hold inside a star.

The first stellar structure equation represents the mass distribution in a spherically symmetric stellar model. It is a relationship between mass, radius and density. For a spherically symmetric star, consider a shell of mass dM_r and thickness dr, located at a distance r from the center. The volume of the shell can approximately be given by $dV = 4\pi r^2 \mathrm{dr}$. If the local density of the gas is ρ, the shell's mass is given by

$$dM_r = 4\pi r^2 \rho dr \tag{1.2.1}$$

Rewriting, we arrive at the mass conservation equation,

$$\frac{dM_r}{dr} = 4\pi r^2 \rho \tag{1.2.2}$$

which states how the interior mass of a star must change with distance from the center

If a small portion of the shell between r and $r+dr$ is considered, with dA as the transverse area of this small element, the forces exerted by pressure acting on its inward and outward surfaces are PdA and $-(P+dP)dA$. The net force arising out of pressure is $-dPdA$, which should be balanced by gravity under equilibrium conditions. The gravitational field at r is caused by the mass M_r inside r and is equal to $-GM_r/r^2$.

Since the mass of the element under consideration is $\rho\ dr\ dA$, the force balance condition for it is given as

$$-dPdA - \frac{GM_r}{r^2}\rho dr dA = 0 \tag{1.2.3}$$

which can be rewritten as

$$\frac{dP}{dr} = -\frac{GM_r}{r^2}\rho \tag{1.2.4}$$

where G is the gravitational constant, and P and $P+dP$ is the pressure being exerted at r and $r+dr$ respectively. This is the second fundamental equation in stellar structure that describes the hydrostatic equilibrium in terms of the internal pressure and the gravitational force, both acting in opposite directions This equation clearly indicates that in order for a star to be static, a pressure gradient must exist to counteract gravity. It is not the pressure that supports a star, but the change in pressure with radius. It also tells that the pressure must decrease with increasing radius; with the pressure being larger in the interior than it is near the surface.

The energy generated by nuclear reactions in the central region of a star is transported outward. If L_r is the total power passing through the spherical shell between r and $r+dr$ at radial distance r, and ϵ is the rate of energy generation per unit mass per unit time, we get

$$dL_r = 4\pi r^2 dr \times \rho\epsilon \tag{1.2.5}$$

from which, dLr can be given by

$$\frac{dL_r}{dr} = 4\pi r^2 \rho\epsilon \tag{1.2.6}$$

ϵ is an important quantity defining the energy coming from nuclear reactions and establishes the link where nuclear reaction rates directly affect stellar structure and evolu-

tion.

This is the third of the important stellar structure equations illustrating conservation of energy.

The energy flux is driven by the temperature gradient inside the star. As already discussed in the one of the previous subsections, there are two dominant modes of heat transfer in stars - convection and radiation. The total power L_r given out across the spherical surface f radius r can be given as

$$L_r = 4\pi r^2 F = -4\pi r^2 \frac{c}{\chi\rho}\frac{d}{dr}(\frac{a_B}{3}T^4) \tag{1.2.7}$$

from which

$$\frac{dT}{dr} = -\frac{3}{4a_B c}\frac{\chi\rho}{T^3}\frac{L_r}{4\pi r^2} \tag{1.2.8}$$

where, χ is the opacity of the stellar matter.

This is the fourth equation of stellar structure i.e. the equation of energy transport, if the heat flux is carried outward by radiative transfer (A. R. Choudhuri, 2010).

1.2.1 Reaction rates and cross sections

In this section, I will discuss the basic equations needed to determine stellar reaction rates, with special focus on the parameters important in experimental determination of these rates.

In stellar environments, nuclear material is synthesized when two nuclei react to produce new nuclear species. A particle a can react with target particle X to form the product pair b and Y, where Y is the synthesized nucleus, and b can either be a product particle, a γ ray photon, or both. In stellar nucleosynthesis models, reaction rates are required because they define the flow of nuclear material being synthesized. To define the rate of reaction, an expression for cross-section of the reaction at a given energy is needed. In a stellar plasma, the kinetic energy available to nuclei is that of their thermal motion and that is why the reactions initiated by this motion are called thermonuclear reactions. The typical particle energies found in stellar environments are too low to overcome the Coulomb repulsion between light particles (of the order of a few hundred keV to a few MeV). However, the particles may penetrate the Coulomb barrier through the quantum tunneling phenomenon. At low energies, the penetration through the barrier can be approximated as

$$P = exp(-2\pi\eta) \tag{1.2.9}$$

η is the Sommerfeld parameter given by

$$\eta = \frac{Z_1 Z_2 e^2}{hv} \tag{1.2.10}$$

In this form, P is called Gamow Factor, with Z_1 and Z_2 being the charges of the two particles and v is their relative velocity.

The interiors of stellar systems, comprising of hot nuclear plasma containing different abundance of isotopes, are in dynamic thermal equilibrium meaning that the velocity distribution of particles follows the Maxwell-Boltzmann relation. In terms of energy, Maxwell-Boltzmann Distribution can be given as $P(E)dE = Eexp(-E/kT)dE$, which gives the probability of finding the particle in an energy between E and $E + dE$. The value $E = kT$ represents the energy at which any given particle has the highest probability of being found in.

From equation 1.2.9 and 1.2.10, it can be seen that the probability of reaction to occur has to depend on the probability of tunneling through the barrier. This probability is quantified by the reaction rate per particle pair. For a particle induced reaction, the reaction rate per particle pair, in units of $\mathrm{cm}^3\ \mathrm{s}^{-1}\ \mathrm{mol}^{-1}$, is given as a convolution of the velocity dependent cross section and Maxwell Boltzmann velocity distribution

$$N_A < \sigma v >= N_A (\frac{8}{\pi\mu})^{\frac{1}{2}} \frac{1}{(kT)^{\frac{3}{2}}} \int_0^\infty E\sigma(E) e^{\frac{-E}{kT}} dE \tag{1.2.11}$$

where $\sigma(E)$ is the energy-dependent cross section and factor $e^{\frac{-E}{kT}}$ comes from the

Maxwell-Boltzmann Distribution, k is the Boltzmann constant, and μ is the reduced mass of the two participating nuclei. Once the cross section $\sigma(E)$ has been measured or estimated theoretically, the above integral can be solved numerically to find out the reaction rate. It is important to emphasize here that cross section, σ, has a dependence on energy E. There are two scenarios based on how the cross section varies with energy. The first case refers to cross sections that vary smoothly with energy called non-resonant cross sections. The second case applies to cross sections which vary strongly in the vicinity of a particular energy called resonant cross sections (C. Rolfs et al., 1988).

Nonresonant Reaction Rate Since the variation of the non-resonant cross section with energy is smooth, the reaction rates in this case may be obtained either by numerical integration or by using analytical expressions. At this point, astrophysical S-factor $S(E)$ is introduced by rewriting the expression for cross-section as

$$\sigma(E) = \frac{1}{E} e^{-2\pi\eta} S(E) \tag{1.2.12}$$

where, $S(E)$ is the astrophysical S-factor, $\frac{1}{E}$ is a factor accounting for de-Brogile wavelength of the particle. The astrophysical S-factor $S(E)$ has been introduced to account for all the specifically nuclear effects and properties which determine the reaction probability. The experiments at typical stellar energies are extremely difficult to measure directly due to the low cross-sections involved and the small signal-to-noise ratio. The significance of

defining astrophysical S-factor lies in the fact that experimental cross sections measured at higher energies can be extrapolated down to astrophysical regime. This becomes possible due to slow, continuous variation of $S(E)$ with energy, when resonances are not present.

Resonant Reaction Rate The previously derived reaction rate expression relies on the smooth variation of the S-factor with energy for non-resonant (direct) reactions. However, very often, resonant reactions can take place where the two nuclei a and X can fuse together into an excited state of a compound nucleus, then decay into the product particles b and Y. In this case, when the incident energy is such that the wavefunctions of the incident particle and the compound state are well matched, the cross-section for reaction is greatly enhanced around this energy, causing a large increase in the astrophysical S-factor $S(E)$. The cross section for a resonance reaction is given by the Breit-Wigner form

$$\sigma_{BW}(E) = \frac{\lambda^2}{4\pi}\omega\frac{\Gamma_x\Gamma_\gamma}{(E-E_r)^2+\frac{\Gamma^2}{4}} \tag{1.2.13}$$

Using $\sigma_{BW}(E)$ in 1.2.11 , we have

$$N_A < \sigma v >= (\frac{2\pi}{\mu KT}^{\frac{3}{2}})\frac{h^2}{4\pi}\omega\gamma e^{\frac{-E_r}{kT}} \tag{1.2.14}$$

Here, E_r is the resonance energy and $\omega\gamma$ is the resonance strength defined as

$$\omega\gamma = \frac{2J_r + 1}{(2j_A + 1)(2j_x + 1)} \frac{\Gamma_x \Gamma_\gamma}{\Gamma_{tot}} \tag{1.2.15}$$

Here, J_r is the spin of resonance, j_A is the spin of the heavy particle and j_x is the spin of the lighter particle, Γ_x and Γ_γ are the partial energy widths for decay by emission of particle 'x' and 'γ', respectively and Γ_{tot} is the total width of the resonance state. Therefore, its clear from the expression above that one needs to determine the resonant energy as well as resonance strength.

1.3 Theory of Reactions in Stellar Environments

In stellar nucleosynthesis models, reaction rates are required which define the number of reactions taking place per unit volume per unit time. In order to derive an expression for the reaction rate, the cross-section for the reaction at a given energy must be known.

A central focus of nuclear astrophysics is to measure the rates (or cross-sections) for the reactions occurring in the stars. In order to study these, techniques of nuclear physics are indispensable. It is of vital importance to examine what the appropriate energy regime is for the reaction of interest in astrophysical scenarios. Considering that the two particles involved in the reaction undergo fusion, from a classical point of view, the two would have to overcome the Coulomb barrier. As discussed in the introduction part of the thesis, by following Maxwell-Boltzmann distribution, the energy distribution characterized by the temperature T peaks at $E = kT$. When this distribution is convoluted with tunneling

probability, it shifts this statistical energy distribution of particles to an energy higher than kT, referred to as Gamow Peak E_0 as shown in Figure 1.7. The energies at which the astrophysical nuclear reactions occur are quite low and correspondingly the cross sections of interest are low at these energies.

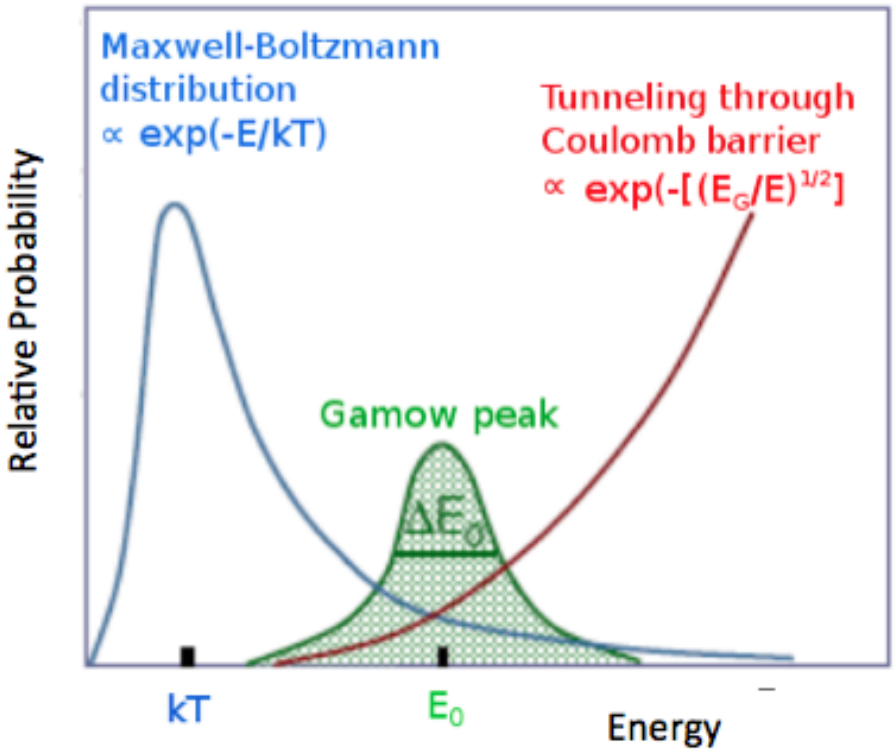

Figure 1.7: Energy dependent functions for a charged particle nuclear reaction; within the small overlap region is a peak at E_0 called Gamow Energy (Figure adapted from D. Montanari et al., 2016)

It comes across as an experimental challenge to perform measurements at these energies. To resolve this problem, making the measurement at a higher energy and then

extrapolating to lower energy of interest is a plausible solution. For a reliable extrapolation, role of astrophysical S-factor is crucial since the expression of cross section in terms of S-factor gets rid of all the non-nuclear effects.

The reaction of interest ^{19}F(p,α)^{16}O$_{gs}$ is a three-nucleon transfer process. This reaction dominates the total rate at temperatures relevant for AGB stars (K. Spyrou et al., 2000). The technique employed is to determine spectroscopic amplitude by the analysis of the experimental angular distributions for the reaction. In the work to follow in next chapters, we analyze ^{19}F(p,α)^{16}O$_{gs}$ in the framework of the Finite-Range Distorted Wave Born Approximation (FR-DWBA), understanding this reaction in the direct reaction mechanism in thermonuclear energy regions.

A nuclear reaction is initiated when a nucleon or nucleus collides with another nucleon or nucleus. A complete description of a nuclear reaction involves other observable quantities beside the incoming nuclei and the outgoing reaction products. Among these are the relative energy of the incoming and outgoing nuclei and the scattering angle of the outgoing products. Although there are many possible outcomes when two particles collide, the main focus of this work is on two particles in the exit channel. The standard notation for such a nuclear reaction is $A(a,b)B$, where A is the target, a is the projectile, B is the recoil, and b is the ejectile. The reactions can be classified in many ways. If the incident and outgoing particles are the same, it is called a scattering process. If B and b are in their ground states, it is elastic scattering, and if B and/or b is in an excited state, it is called an inelastic scattering. On the other hand, if one or two nucleons are transferred between

projectile and target, it is called a transfer reaction. The advantage of transfer reactions is in extracting information on the valence orbitals of a nucleus, mostly for the surface-dominated reactions. Useful information on nuclear structure such as angular momentum transfers and spectroscopic strengths are determined through these reactions, assuming the reaction is studied over a range of angles including the more forward angles in the center of mass. Transfer reactions belong to a broader category of direct reactions, only very few nucleons take part in the reaction, with the remaining nucleons of the target serving as passive spectators. Such reactions insert or remove nucleons from a shell model state and might therefore serve as a way to explore the shell structure of nuclei.

1.3.1 Experimental Determination of Stellar Reaction Rates

In the hot and explosive burning phases of stars, nuclear burning times are in seconds. If the lifetime of a radioactive nucleus is longer than or of the same order as the burning time, that nucleus will be involved in the nuclear burning processes. Currently, much research is being done into the reaction rates of various nuclear processes in low energy stellar environments, such as burning in main sequence stars and red giants. Nuclear cross-sections are measured at the lowest possible experimental energy, and then extrapolations are made to stellar energies, which tend to be lower still. From the knowledge of nuclear cross sections, reaction rates can be evaluated. A number of experimental techniques are used in direct measurements of astrophysically important reactions that require special equipment and procedures, mainly radioactive ion beams. Reactions in a stellar plasma at elevated

temperatures do not only involve stable nuclides but also unstable nuclides which participate in the nucleosynthesis. But the instability of one of the interacting nuclei comes across as a challenge for an experimentalist. If the half life exceeds a few days, then it may be possible to fabricate a radioactive target and to measure directly the reaction of interest by bombarding the target with appropriate particles. However, if the half life of a species amounts to a few minutes or less, then the fabrication of a radioactive target is not possible. In this case, the only direct method is to produce the radioactive nuclides in an accelerator, separate them, accelerate them in a second accelerator, and finally allow the radioactive ion beam (RIB) to interact with a H_2 or He target. The challenge here is that all of this must be achieved in a time shorter than the decay lifetime of the radioactive nuclides. Such measurements are referred to as inverse kinematics studies, in which energetic beams of radioactive nuclei induce nuclear reactions. The overall understanding of nuclear phenomena has been greatly enhanced since the advent of radioactive ion beams. The production of such beams requires an experimental facility equipped with a primary production beam. The direct approach is the online production of radioactive nuclei, their ionization and extraction from an ion source, and their subsequent acceleration. A beam of stable nuclei from a production accelerator bombards a thick target and produces radioactive nuclei. These diffuse out of the target, through a transfer tube, and into an an ion source where they are ionized and continuously extracted. The radioactive ions are then mass separated from other, undesired, isotopes. At this stage they represent a beam of unaccelerated, low-energy radioactive ions. Subsequently, they are accelerated by a post accelerator which allows a tuning of the beam energy to the desired value. This accelerated radioactive ion beam is

finally incident on a hydrogen or helium target. The radiation emitted in the reaction of interest is then observed using suitable detectors. ISOL (Isotope Separator On-Line) facilities operational today are at TRIUMF in Canada (G. C. Ball et al., 2011) and CERN in Switzerland. The experimental part of this thesis has been performed at TRIUMF.

In another technique, the emergent exotic ions can be rapidly separated by in-flight techniques before they decay (J. M. D'Auria, 1995). This technique is called in-flight separation method. Another striking feature of this technique is the use of thin production target to produce radioactive beams. The resultant radioactive beam, therefore, retains a large fraction of its initial kinetic energy. Hence, an advantage of this method is that beams can be produced and delivered at high energy without the need for reacceleration. The fragments pass through a multi-stage fragment spectrometer and then subsequently used for further reactions. This process is not sensitive to chemical properties of the isotopes of interest but it is quite challenging to achieve beam with good ion optical qualities. The fact that with such techniques radioactive beam experiments can be performed in inverse kinematics has an interesting consequence. In inverse kinematics, the solid angle in the center-of-mass system is significantly compressed up smaller as compared to the solid angle in the laboratory reference frame. This indeed helps in increasing the efficiency and sensitivity of the detection system as a small angular coverage is sufficient to measure and analyse a complete angular distribution. The first nuclear astrophysics experiment with an accelerated radioactive ion beam was the measurement of the $^{13}\mathrm{N}(\mathrm{p},\gamma)^{14}O$ reaction at Louvain-la-Neuve in 1993. Since this pioneering study, several astrophysically important

reactions have been measured directly or indirectly at a number of different radioactive ion beam facilities worldwide. Radioactive ion beam facilities have opened a window of previously unavailable capabilities in nuclear astrophysics. The major experimental procedures used in the field of nuclear astrophysics can be divided into two groups - direct and indirect measurements. If a measurement is performed to measure the cross-section or resonance strength of a particular reaction, it is referred to as a direct measurement. If, on the other hand, a measurement is performed to improve the thermonuclear rate of this particular reaction, by means of elastic scattering, particle transfer, charge exchange, it is referred to be an indirect measurement (C. Iliadis, 2010).

1.3.2 Nuclear Astrophysics goals of this thesis

For this thesis, focused on a new attempt in measurement of ^{19}F(p,α)^{16}O, inverse kinematics technique was employed. In this measurement, a solid hydrogen target was used with incoming projectile as a stable beam of ^{19}F at an energy of E_{cm} = 2.35 MeV. This center of mass energy at the interaction point in the target corresponds to an incident beam energy of 2.46 MeV/u in the laboratory frame (E_{cm}= E_{lab} $\times$m$_{target}$/($m_{target} + m_{beam}$)). Despite of the significance of this reaction, the astrophysical factor $S(E)$ of this reaction is poorly known from previous studies. Therefore, the primary motivation to study this reaction is to extract a more reliable value for the astrophysical-factor $S(E)$ of ^{19}F(p,α)^{16}O.

To constrain some of the nuclear physics information discussed in the sections above, this reaction was measured using the IRIS facility at the ISAC rare isotope beam

facility at TRIUMF, Canada. The latter part of this thesis will focus on the experimental details involved in the study of this reaction.

1.4 Looking Ahead

The remainder of this thesis will focus on a detailed description of the experimental and theoretical details of this measurement, highlighting some nuclear parameters of astrophysical significance. The structure of the following work is as follows:

Chapter 2 explains the experimental set up designed for studying ^{19}F(p,α)^{16}O reaction. The details include the scientific motivation behind the detectors. It includes the discussion of various detectors, followed by a detailed process of calibration of detectors. This chapter also includes a detailed description of electronics and data acquisition components used in this measurement.

Chapter 3 discusses the data analysis of the information obtained from calibrated detectors. The technique used such as missing mass technique is discussed. Towards the end of the chapter the theoretical framework used in the analysis of this work is detailed.

Chapter 4 includes a discussion on the statistical techniques used in the data analysis, followed by uncertainties calculations. The final results are evaluated with implications of this work for nuclear astrophysics.

Chapter 2

Experimental Set Up and Techniques

Single and multi-nucleon transfer reactions are useful tools in nuclear spectroscopy. Nuclear transfer reactions have long been used to study the structure of nuclei. As discussed in the previous chapter, such studies are an important method for constraining astrophysically important reaction rates. This chapter gives an overview of the techniques and detectors used for the measurement of the ^{19}F(p,α)^{16}O reaction cross section at an incident beam energy of 4 MeV/u. The ^{19}F beam was produced at TRIUMF, Vancouver, Canada. TRIUMF is Canada's particle accelerator centre. The laboratory is located around the world's largest cyclotron, providing H^- ions upto 520 MeV. The facility used for producing radioactive and stable nuclear beams is named Isotope Separator and Accelerator (ISAC). In the following

sections, the setup of the IRIS facility used for this experiment will be detailed.

2.1 IRIS

The IRIS facility is a charged particle spectroscopy station in the ISAC II experimental area at TRIUMF, designed to study elastic, inelastic scattering and transfer reactions with radioactive ion beams and isotopes of hydrogen p and d as targets. The reaction is studied in inverse kinematics where the beam is heavier than the target. The reaction products are detected in the silicon detectors placed downstream of target. Each unit of the set up is placed in a separate vacuum chamber to avoid the energy losses in air.

Shown in Fig. 2.1 is a schematic layout of the facility with the detector arrangement.

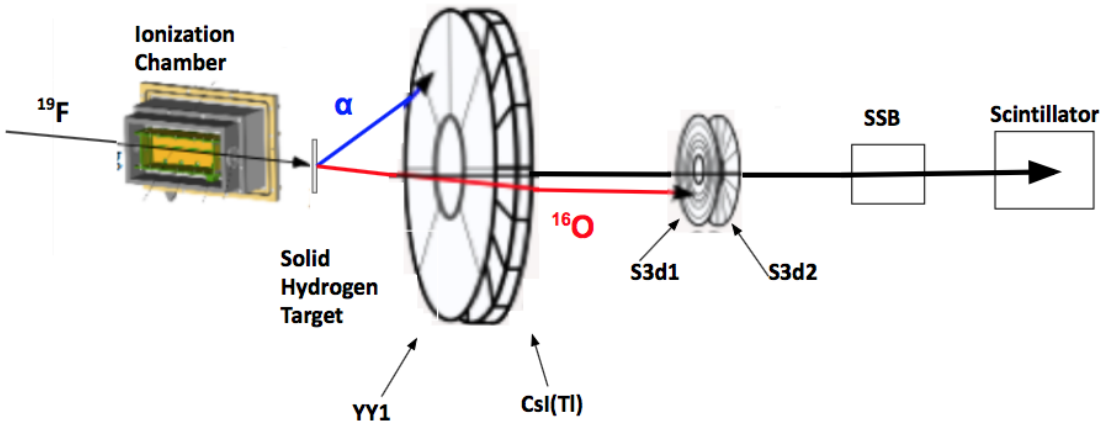

Figure 2.1: IRIS set up

The four major components of the IRIS facility are the ionization chamber, solid H_2/D_2 target, the charged particle detectors for detecting the reaction products and two detectors at the end, SSB (silicon surface barrier) detector and scintillator detector, for detecting the unreacted beam. In the following sections, each of these components are described in detail.

2.1.1 Ionization Chamber

This is the first detector in the beam line. It is placed upstream of the target in order to measure the beam condition before it reaches target. It is a gas-filled detector and it serves two purposes. First, to count the number of incident beam particles. Second, to detect the constituents of the beam i.e. isobaric contaminants by identifying their atomic number Z through energy loss in the gas chamber. This identification of the beam components is important, in particular, for medium mass and heavy mass nuclei that are difficult to post accelerate as pure beams. For ^{19}F, the beam was relatively pure as it is a stable isotope. As we are dealing with fairly low energy particles at IRIS, it is important to minimize the energy losses by the particles traversing the Ionization Chamber (IC) so that the physics at the reaction target is not greatly affected. The fill gas in the IC must be maintained at a low pressure while still allowing for a signal to noise ratio high enough to make necessary measurements. The fill-gas used is isobutane, maintained at 19.5 Torr, along with thin entrance and exit windows of the IC. The windows of the chamber are made from silicon nitride Si_3N_4, 50 nm in thickness and dimensions of 10 mm $\times$ 10 mm (R. Kanungo, 2013).

The purpose of the windows is to separate the gas volume from the vacuum. IC is equipped to have a multi-sampling anode system of 16 independent anodes used for charge collection. The anodes can be coupled together in sections to have a single anode read out as well, to optimize for desired energy loss depending on each case. For the present experiment with ^{19}F beam, the anodes were coupled to be one single read-out. The electrical signal produced in the anode is read out using a charge-sensitive preamplifier located outside the vacuum chamber (P. R. Fortier, 2013).

2.1.2 Solid Hydrogen Target

The use of a solid hydrogen target (SHT) is a unique and novel feature of IRIS for low-energy reactions with radioactive ion beams. The distinguishing feature of this set up which sets it apart from other systems is it being solid, thin and windowless at the exit channel. The advantage of this set up lies in higher density of the target atoms because more target atoms imply more reaction centers, and therefore more reaction yield. In addition to achieving a higher yield with low-intensity beams of exotic nuclei, the SHT also has an advantage in terms of background. Other target systems such as liquid or gas targets have windows or supporting materials which add extra layers contributing heavily to background. Since SHT has a thin silver foil backing only on upstream of the target, the scattered particles do not encounter any other material before reaching the detectors. This suppresses the energy straggling and multiple scattering. It is of advantage as the energy loss in the target is a critical determinant of the final energy resolution of the measurement.

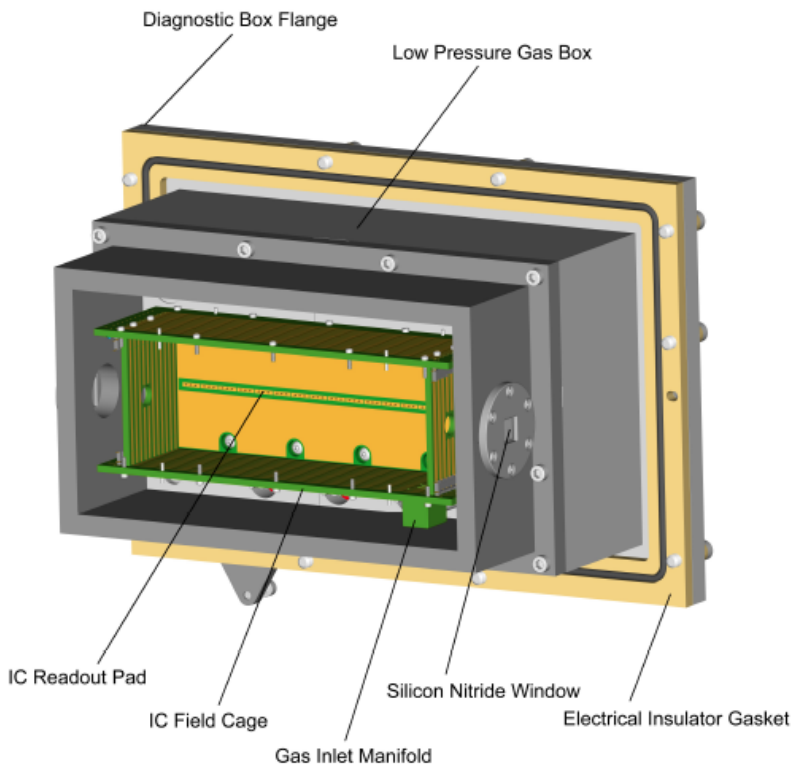

Figure 2.2: A computer rendering of the IRIS IC attached to its vacuum chamber flange showing the main components of the IC (G. Sheffler 2013)

Figure 2.3 provides a view of the salient features of the target assembly, silver backing foil on copper cell in (a), solid hydrogen target cell in (b), and the cylindrical heat shield in (c). The target assembly comprises of a copper cell placed inside a cylindrical heat shield. On the copper cell, a 5 mm hole is bored in the center. A thin silver foil of thickness $\sim 4.5\,\mu\text{m}$ lines one face of the target cell onto which the desired target solid H_2 is formed. A cryocooler with a helium compressor is used to cool the target cell to a temperature of $\sim$ 4 K.

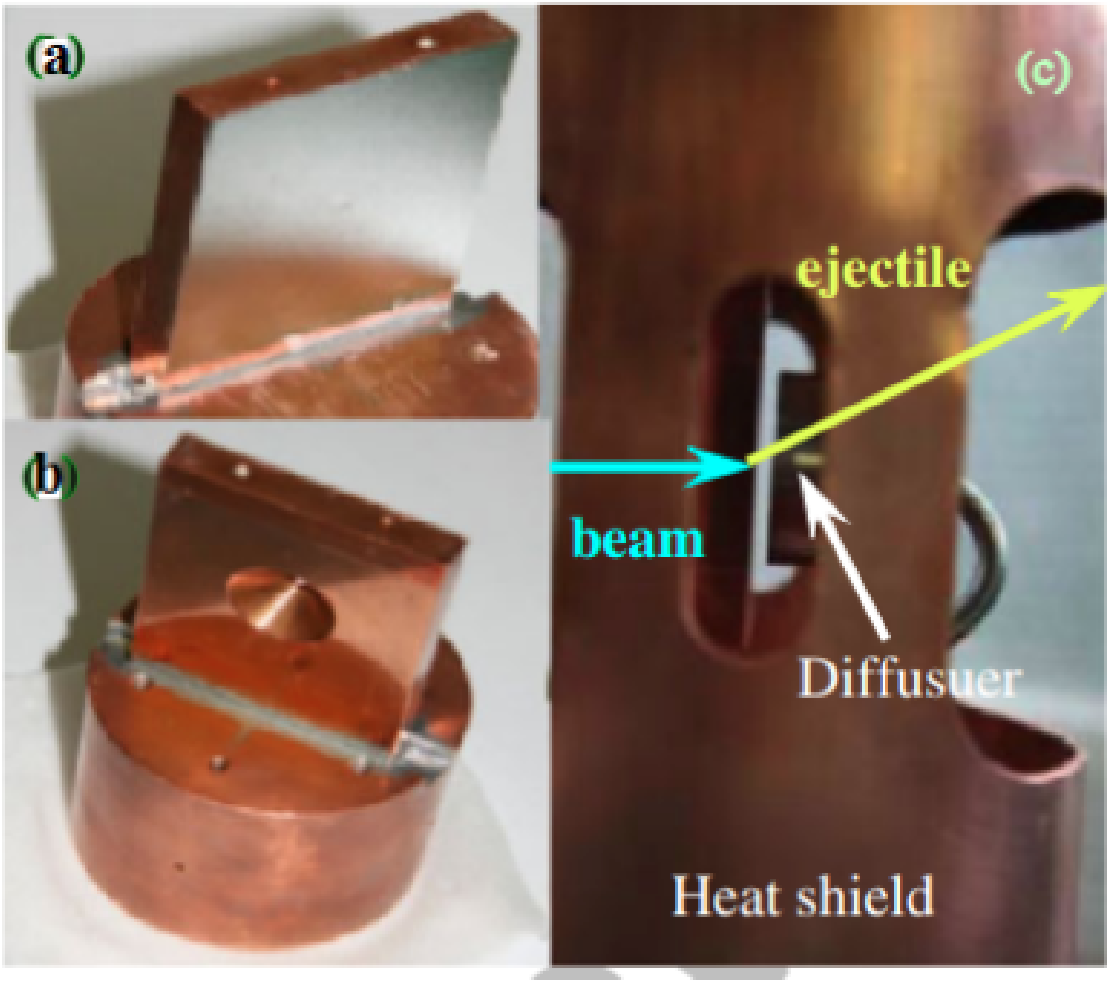

Figure 2.3: Solid H_2 target assembly (R. Kanungo, 2013)

A diffuser in the beam line, which can move up and down when needed, is used to spray the H_2 gas on the surface of the silver foil to form a solid H_2 target. By controlling the gas volume the desired target thickness can be achieved. This set up is shown in Fig. 2.4 showing the diffuser in action.

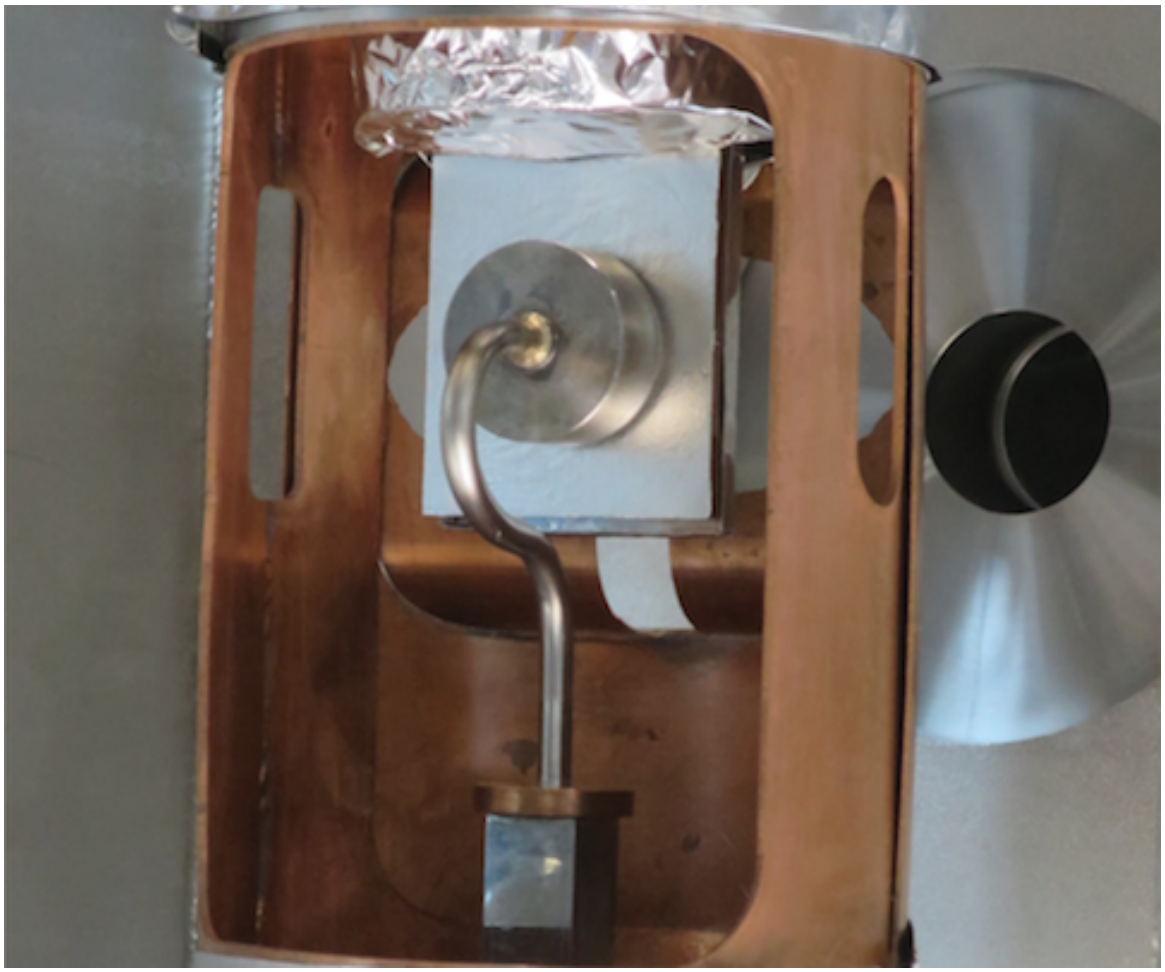

Figure 2.4: IRIS target assembly showing the diffuser in upper position in front of the silver foil, placed within the copper heat shield

The main purpose of the copper shield is to minimize the heating of the target from the ambient temperatures. The reaction products from the target are emitted through

the opening in the heat shield.

In the present work on $^{19}F(p,\alpha)^{16}O$, the incoming ^{19}F beam passes through the silver foil backing and then hits the solid hydrogen target. The beam interacts randomly within the target and the reaction products then pass through the remaining thickness of the target. In addition to the desired reaction products, fusion evaporation reactions from the silver foil are also present as background events. To separate such unwanted products, the contribution from the background reactions can be separately measured with beam hitting the silver foil only (i.e. no hydrogen target on the silver foil).

2.1.3 Charged Particle Detectors

The main focus of the IRIS facility is to detect the charged particle reaction products from the reactions with isotopes of hydrogen as target. Therefore, the detection system is designed to detect both the light target-like reaction ejectiles and well as the heavy beam-like reaction residues. The detectors employed to detect the light fragments and heavy residues after the reaction are termed as charged particle detectors. These are segmented silicon-arrays positioned downstream of the target. IRIS uses two sets of thin and thick detectors to measure energy loss and energy deposited for both lighter target-like fragments and heavier beam-like residues. To measure the energy loss and scattering angle of the lighter particles, IRIS uses detector telescope with a 100 µm thick segmented silicon detector YY1 type followed by a 12 mm thick annular CsI(Tl) array, which is in exactly the same azimuthal configuration as the YY1 array. As the underlying principle of particle identification is ΔE-

E correlation, this pair of detectors is vital in identifying the lighter particles from all the reactions.

Figure 2.5 and Figure 2.6 show photographs of the light particle detectors, YY1 and CsI(Tl), respectively. The annular silicon detector YY1 is segmented into 8 azimuthal sectors. Each sector is further divided into 16 rings which provide the scattering angle information, giving a total of $8 \times 16 = 128$ detectors. The CsI(Tl) detector is an array of 16 individual crystals, each of which is readout using photodiodes as marked in the figure. For this measurement, the angle coverage for the lighter particles was between 18.4°to 40.7°

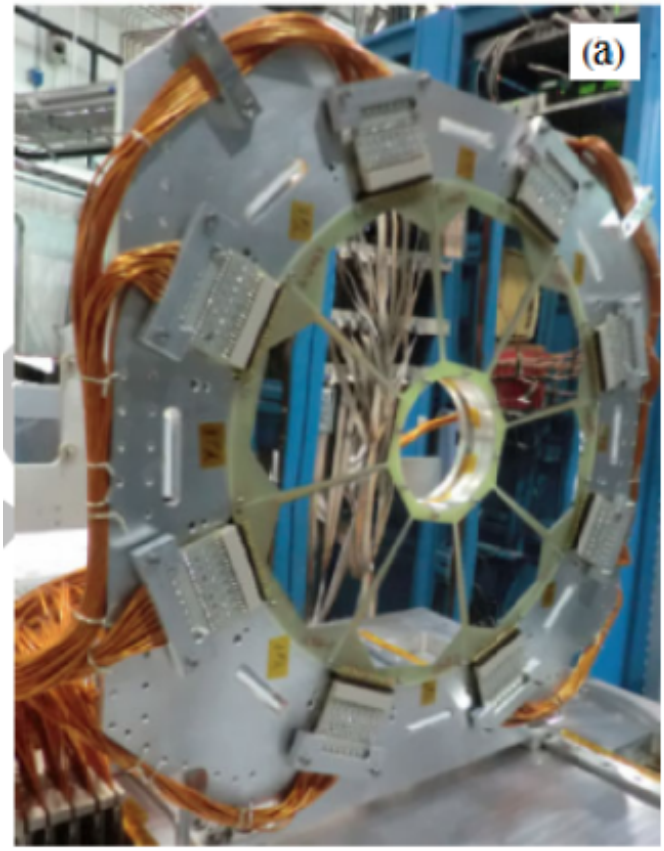

Figure 2.5: Snapshot of the YY1 Silicon Detector Array (R. Kanungo, 2013)

For detecting heavier beam-like particles, a detector telescope is placed downstream of the target. It is a pair of thin and thick detectors made up of S3-type silicon with 60 µm and 500 µm thickness for the active layer silicon respectively. This arrangement allows a ΔE-E identification of the heavy reaction residue. Both the detectors are segmented in 24 rings on one side and 32 sectors on other side. The image of an S3 detector is shown in Fig. 2.7. These detectors were placed in the experiment set up with an angle coverage of 1.2°to 3.81°.

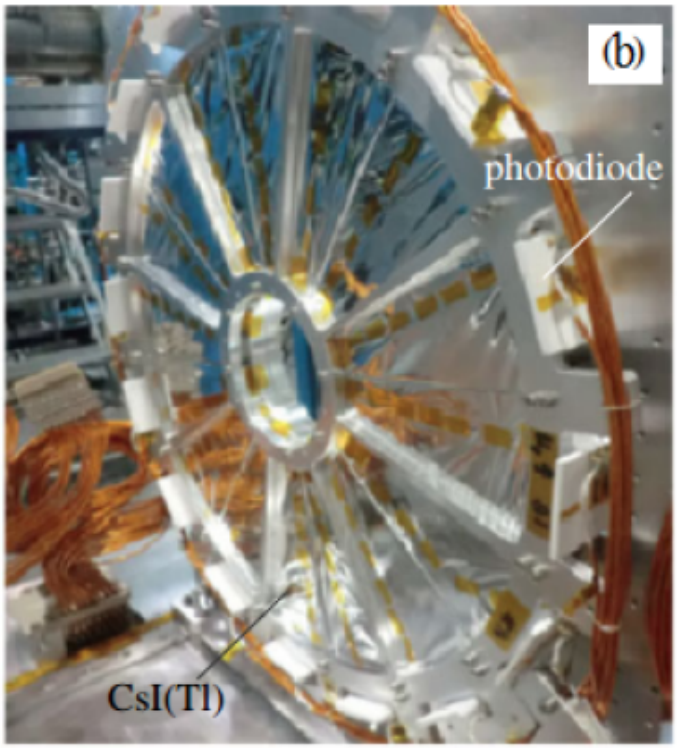

Figure 2.6: Snapshot of the CsI(Tl) Detector Array (R. Kanungo, 2013)

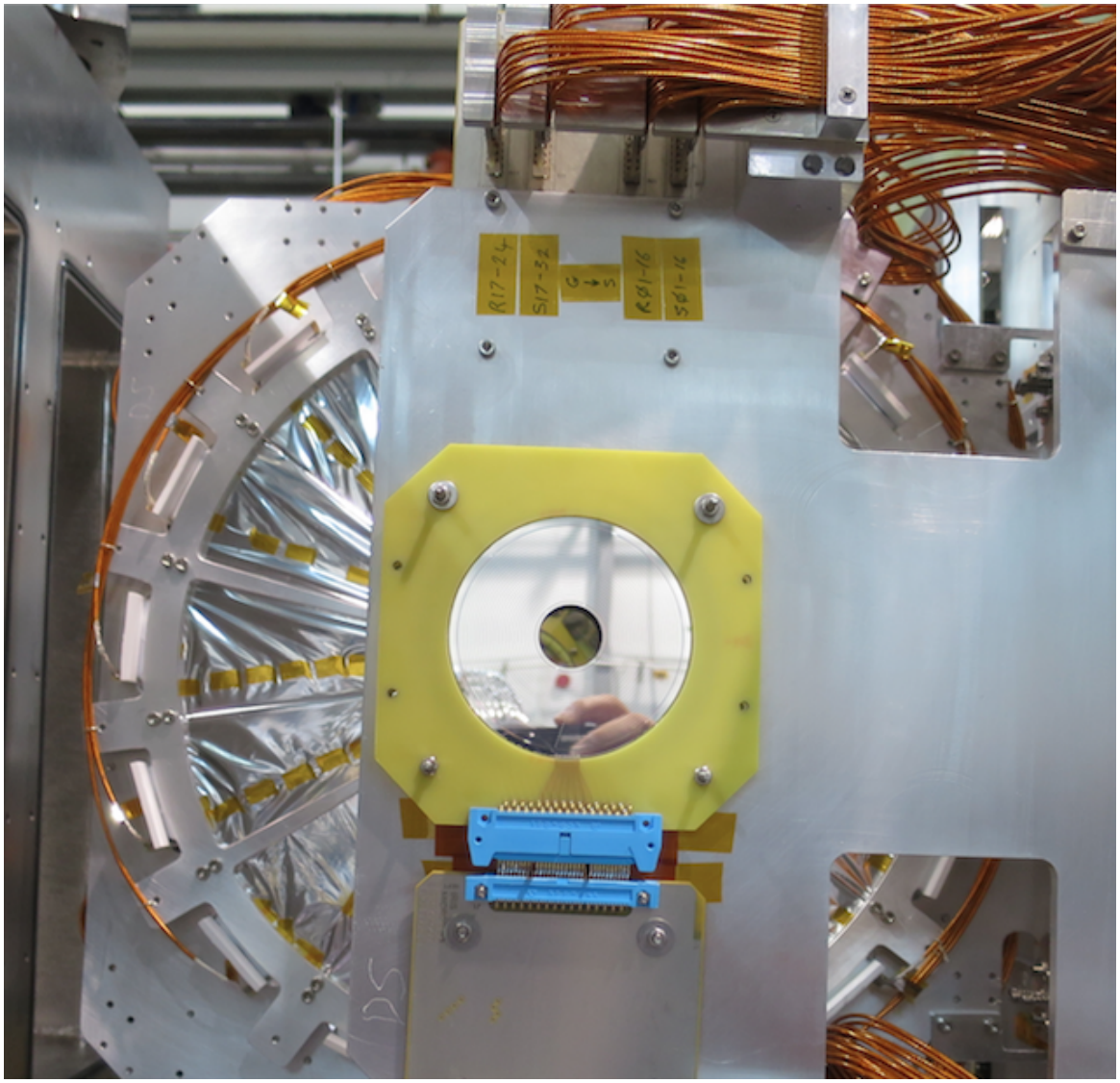

Figure 2.7: S3 Detector viewed from the end of beam line

2.1.4 Scintillator and SSB detectors

These detectors are placed at zero degrees at the end of IRIS beam line to detect the unreacted beam particles. Since detectors for the reaction products described in the previous sections are annular in shape, the unreacted beam particles pass through the hole in these detectors and are eventually stopped and counted using a radiation hard YAP:Ce inorganic scintillator, read out by a photomultiplier tube. The scintillator detector is placed behind another second zero degree detector called SSB detector. This detector is used to measure the remaining energy of the unscattered beam after it passes through the target. This set of detectors is placed in the last vacuum chamber in the IRIS experimental set up. The ratio of the particle counts in the scintillator to that in the ionization chamber provides beam transmission through the experiment set up and is monitored during the entire experiment. Figure 2.8 shows picture of SSB detector taken when taken out of beamline.

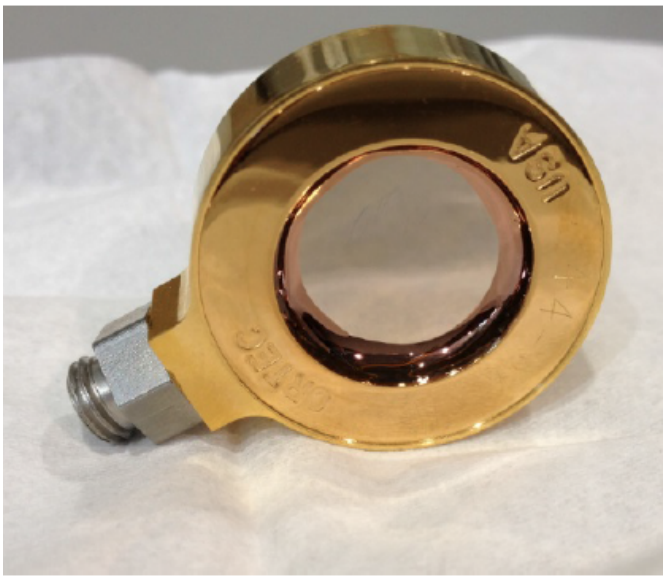

Figure 2.8: SSB Detector

2.2 Data Collection and Electronics

In order to obtain information on the reaction products, these particles are detected using the above mentioned detectors. When these particles pass through the detectors they generate electrical signals. These signals contain the information about the particles - type, energy, and trajectory. This information is digitized and stored in the data acquisition system (DAQ) and is decoded subsequently for extracting the physics information. The set of all detector signals which describe a single nuclear interaction is called an "event". The DAQ needs to know when an interaction event has occurred in the detector. In general, signals from different detectors in an experimental set-up are combined to make a decision on when an event of the physics interest to be recorded has occurred. This generates a trigger which tells DAQ when to read the data. Now, during an experiment, there can be any number of events occurring per second. These events can occur randomly but only a few events are of interest for a particular reaction measurement. In this case, triggering the DAQ means choosing to record the events that we want or are specifically interested in. The detector data must be digitized to be stored on a computer.

A charged particle interacts with the detector material and produces charge carriers through this encounter. If it is an ionization chamber, ion pairs are formed because of ionization. Each ion pair is made up of an electron and the positive ion of an absorber atom in the active volume of the detector. These electric charges carry the information about the energy deposited in the detector by the particle. By applying detector bias, an electric field is created in the detector volume, which causes the positive and negative

charges created by the incident radiation to migrate to the electrodes to be collected. During the charge collection a small current flows, and the voltage across the bias is pulse voltage. The amplitude of the signal pulse is directly proportional to the corresponding charge, Q, generated within the detector divided by the capacitance C of the circuit (G. F. Knoll). It can be expressed as

$$V_{max} = \frac{Q}{C} \tag{2.1}$$

The collected charge therefore produces a voltage pulse which is processed by subsequent electronic circuits comprising of pre-amplifier, shaping amplifier and digitizer. Figure 2.9 shows a schematic of a signal processing circuit.

2.2.1 Signal Processing at IRIS

In this section, the signal processing and trigger logic of the electronics used in the data acquisition for the measurement of ^{19}F(p,α)^{16}O at IRIS will be discussed.

The first element in the signal-processing chain at IRIS is a preamplifier. It provides an interface between the detector and the pulse-processing electronics that follows. The preamplifier used in this experiment were of charge-sensitive type for both silicon and CsI(Tl) detectors. These types of pre-amplifiers deliver an output voltage being proportional to the total integrated charge in the pulse. The rise time of the output pulse is related to the

collection time of the charge, while the decay time of the output is the RC time constant, a characteristic of the preamplifier itself. As shown in Fig. 2.9, the preamplifier is located as close as possible to the detector to reduce capacitance from connecting cables, which can contribute to the noise. Another important function of the preamplifier is to terminate the capacitance quickly and therefore to maximize the signal to noise ratio. Overall, the preamplifier provides no pulse shaping. Once the collected charge passes through the preamplifier, the output pulse is sent into a composite shaping amplifier and discriminator unit. IRIS employs MSCF-16 model (Mesytec Nuclear Physics tools, MSCF-16F) which is a 16-channel shaping/timing amplifier with leading edge discriminator (LED).

The shaping amplifier unit serves to shape the pulse as well as further amplify it keeping the information in the pulse preserved.

Once the signal is shaped and amplified, the discriminator in MSCF-16 responds only to the input signals with a pulse height greater than a specified threshold value. This threshold is set to reject the low amplitude electronic noise.

The MSCF-16 has a CR-RC network that differentiates the pulse to remove the slowly varying decay time and then integrates to reduce the noise. As a result, a near-Gaussian pulse shape is produced, giving an optimal signal-to-noise ratio.

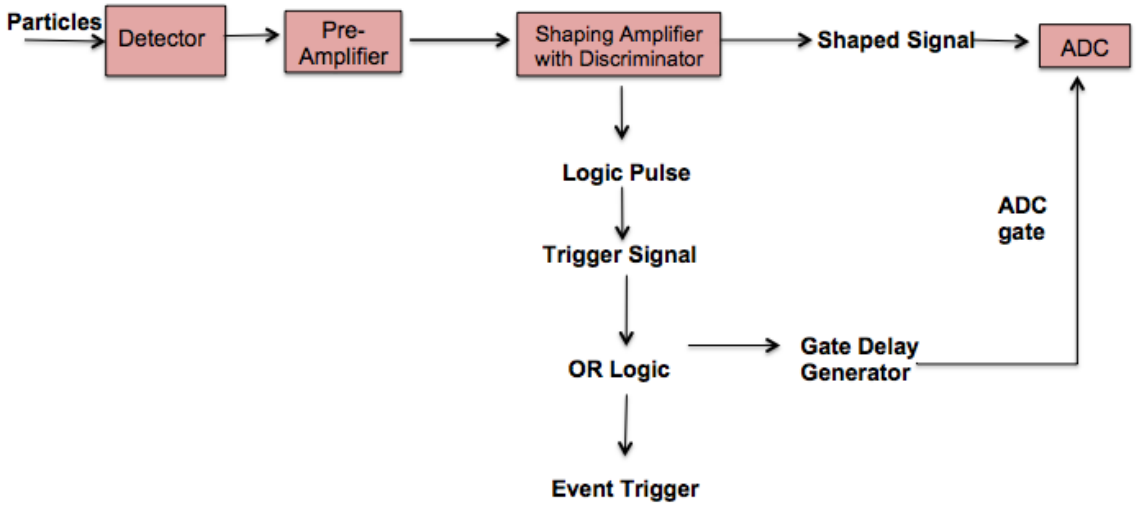

Figure 2.9: Schematic of the electronics for pulse processing showing output from a preamplifier unit and a shaping amplifier for a general detector

This module also has an active baseline restorer which helps to ensure that the baseline between pulses is at the ground potential.

The amplified and shaped energy signal is then fed into analog-to-digital converter (ADC) which converts the amplitude of an analog voltage signal into a proportional digital number. IRIS uses the MADC-32 model from Mesytec which has 32 ADC units. The ADCs used are of peak sensing type and have a resolution of 12 bits, thereby covering a range of channels from 1 to 4096. Since the scattered particles of interest are being detected by the YY1 and S3 detectors, a logic-OR operation on the trigger signals obtained from their respective MSCF-16 units is performed. The resultant signal is called the free trigger. This free trigger is then fed into a gate generator unit which generates the desired gate pulse. This

gate is a user defined window which when fed into an ADC puts it in peak detection and hold mode. This feature, along with ADCs' processing time, enables the ADCs to know when to start taking data and for how long before the next signal can be processed. Figure 2.10 and 2.11 show the schematic of the circuits for pulse processing at IRIS. Figure 2.10 shows how the signal from each detector is sent out into the following circuit i.e. pre-amplifier, shaping amplifier, leading to the formation of free trigger as discussed above.

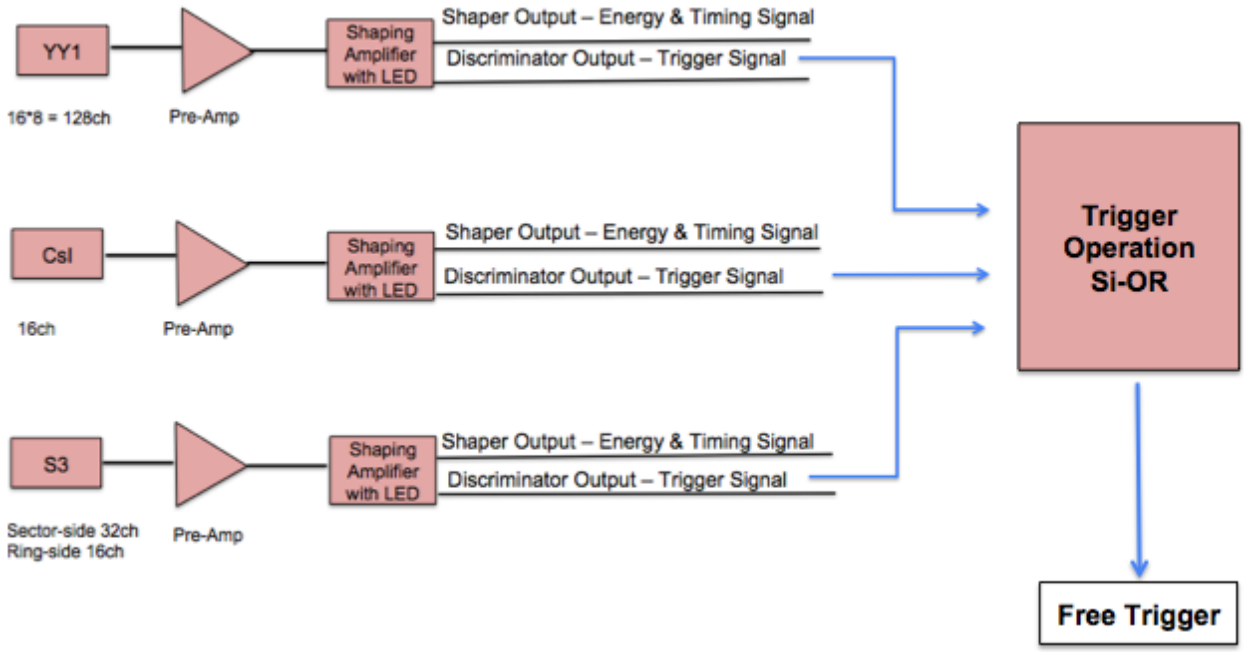

Figure 2.10: Schematic of the electronics for pulse processing showing output from the detectors employed at IRIS leading to formation of trigger logic

Figure 2.11 shows further processing of the free trigger as obtained from each detector.

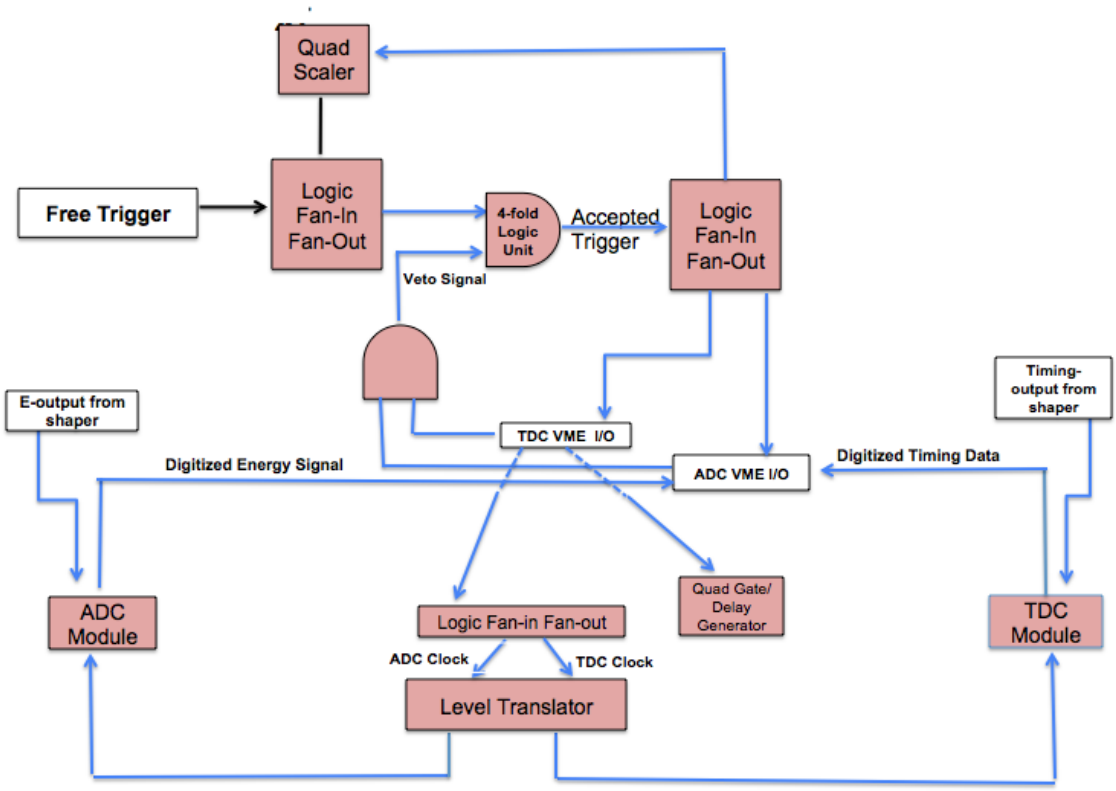

Figure 2.11: Schematic of the electronics showing formation of accepted trigger and analog to digital conversion

2.3 Calibration of Detectors

There are different types of detectors employed in the experiment. To interpret the information recorded in a detector, conversion into a more readable form is important. In this section, the basic process of extracting, sorting and calibrating the experimental data from all the detectors employed at IRIS will be discussed.

The operation of any radiation detector depends on the manner in which the radia-

tion to be detected interacts with the material of the detector itself. An understanding of the response of a specific type of detector is completely based on the fundamental mechanisms by which radiations interact and lose their energy in matter. As discussed in the previous sections, based on the type of detector, ion pairs formed through ionization are used as basis of detector response. The output signal of the detectors is in the form of a voltage pulse. The relation between the radiation energy and the total charge or pulse height of the output signal is understood as the response of the detector. This analog signal is to be analyzed for the exact value of its amplitude. At IRIS, we use peak sensing ADCs in which the maximum of a voltage signal is digitized. Using these ADCs such a conversion is performed in the form of a range of digital numbers named channel numbers of ADC. Converting the channels of ADCs into a physical quantity, energy, is referred to as calibration.

Since the ADC is an instrument that digitizes the analog signal information into digital data, the underlying concept of relating the ADC channel numbers to energy is based on the following linear equation

$$E = g \times (c - p) \tag{2.1}$$

where, E is the energy deposited by the charged particle in the detector, c is the ADC channel number corresponding to the peak position of the signal, p is the pedestal i.e. the zero-energy point in the ADC spectrum, g is called gain i.e. a channel to energy conversion factor for a particular ADC. The calibration, therefore, involves finding gain 'g'

and pedestal 'p' in order to obtain the energy deposit of the ionizing radiation.

We start with the identification of beam particles that pass through the Ionization Chamber (IC). The ^{19}F beam with a total energy of 76 MeV, loses a part of its energy in the IC. This energy loss is used to identify the beam constituents based on the stopping power ($\frac{dE}{dx}$) expression

$$\frac{-dE}{dx} \propto \frac{Z^2}{v^2} \tag{2.2}$$

where, v and Z are the velocity and atomic number of the charged particle, respectively.

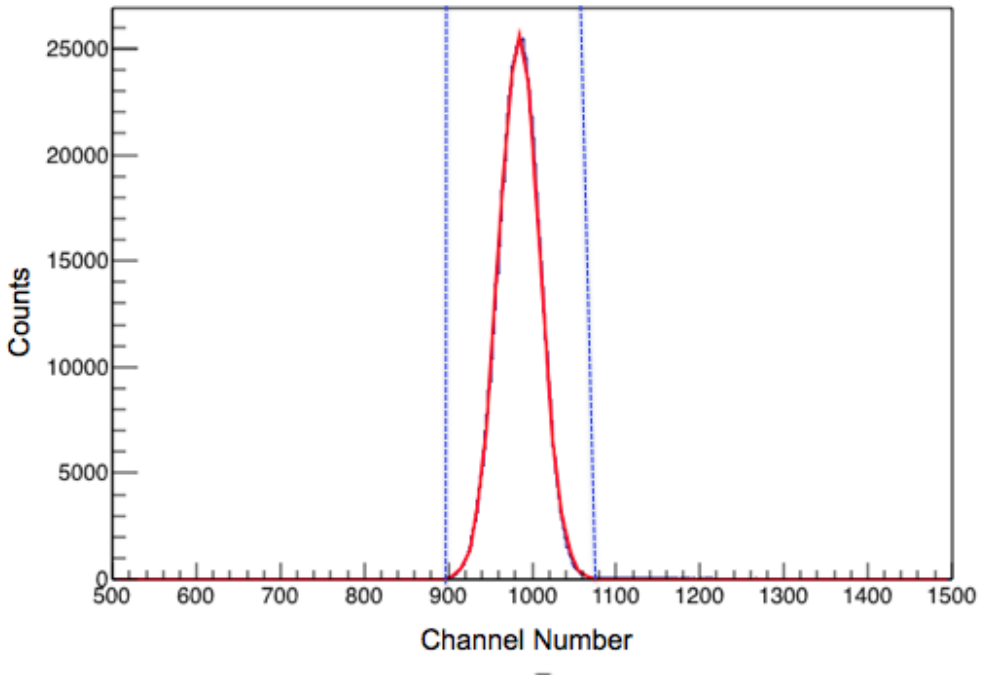

Figure 2.12: IC Spectrum with ^{19}F beam fitted with a Gaussian function in red, blue dashed vertical lines showing the 3σ region for the selection of ^{19}F particles

If there are more than one constituents in the beam, they all have the same energy. Out of those, the particle with higher Z will have more energy loss, based on equation 2.2, and will appear at a relatively higher channel number. The ADC spectrum in Fig. 2.12 of the IC shows only one peak which corresponds to ^{19}F beam particles. Hence, the incoming beam was relatively pure and clean. The blue dashed vertical lines show the selection gate on ^{19}F particles used in further analysis.

2.3.1 Calibration of S3d1 and S3d2 detectors

To calibrate these detectors, the data from elastic scattering of ^{19}F with Ag foil in the absence of solid hydrogen target is used. The scattered ^{19}F, after passing through the intervening material layers and dead layers deposits all of its energy in the first detector S3d1. In the S3d1 detector, 24 rings and 32 sectors segmented on either side act as independent detectors.

The ADC spectrum in Fig. 2.13 shows the peak for scattered ^{19}F from Ag foil for the first ring of the S3d1 detector. This ADC spectrum contains the information about the energy deposited by scattered ^{19}F in the active layer of S3d1. Once this spectrum is fitted with a Gaussian, the peak position in terms of channel number is obtained from the fit. To estimate the energy deposited by ^{19}F in the S3d1 active layer, kinematics calculations are performed for elastic scattering ^{19}F(Ag,Ag)^{19}F with the average position at the middle of the silver foil. The kinematic energy of the scattered ^{19}F then undergoes further energy loss in exiting the target and through the dead layers of the S3 detectors. After these losses are calculated, we obtain the calculated energy that the ^{19}F particles deposit in the active

silicon. This energy is used for calibrating the detector.

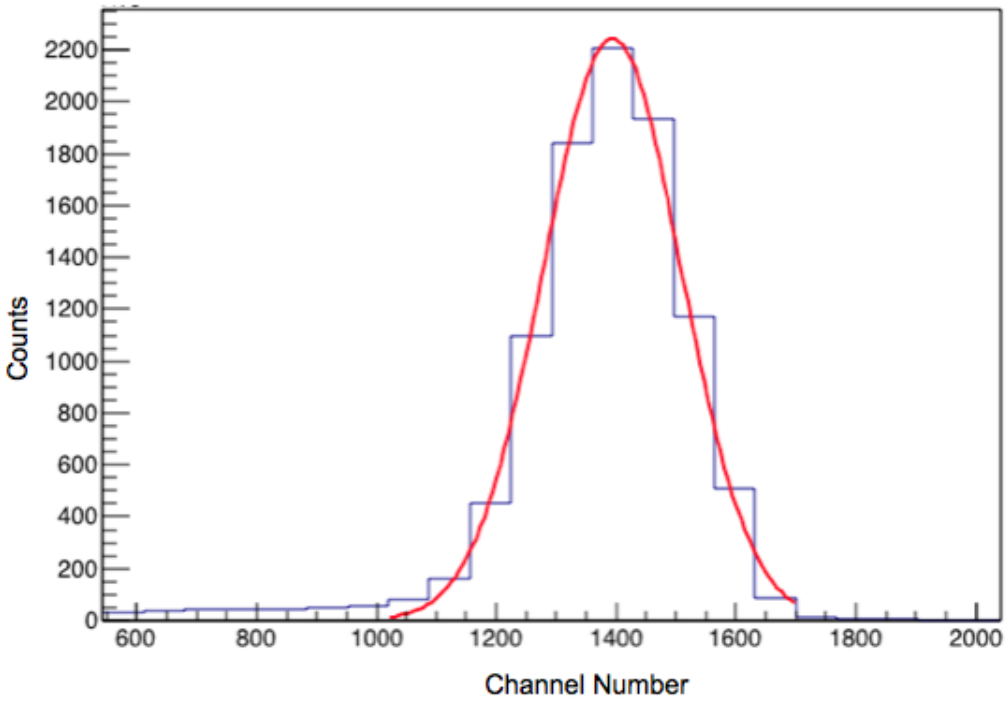

Figure 2.13: ADC spectrum for the first ring of the S3d1 detector fitted with a Gaussian Function

Figure 2.14 shows the trajectory of a scattered particle through various dead layers of S3 detector. Then, the gain is obtained by using equation 2.1. The calibrated energy versus scattering angle plot overlaid with the calculated kinematic locus after the energy losses is shown in Fig. 2.15. The good agreement of calculation with the data affirms proper calibration.

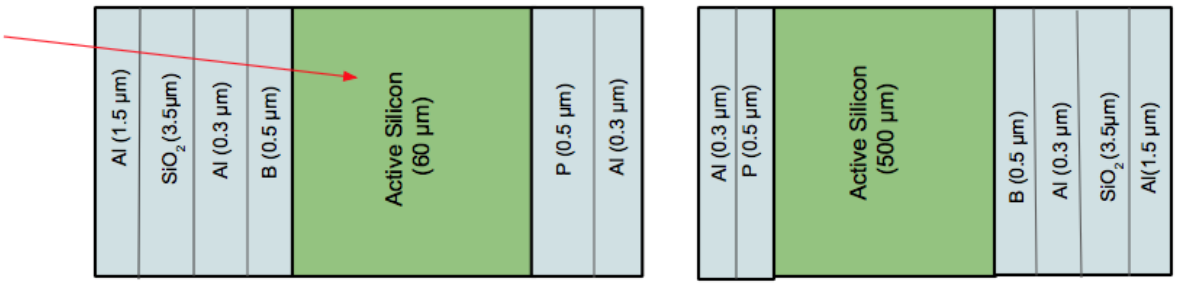

Figure 2.14: Illustration of S3 dead layers where energy losses are taken into account

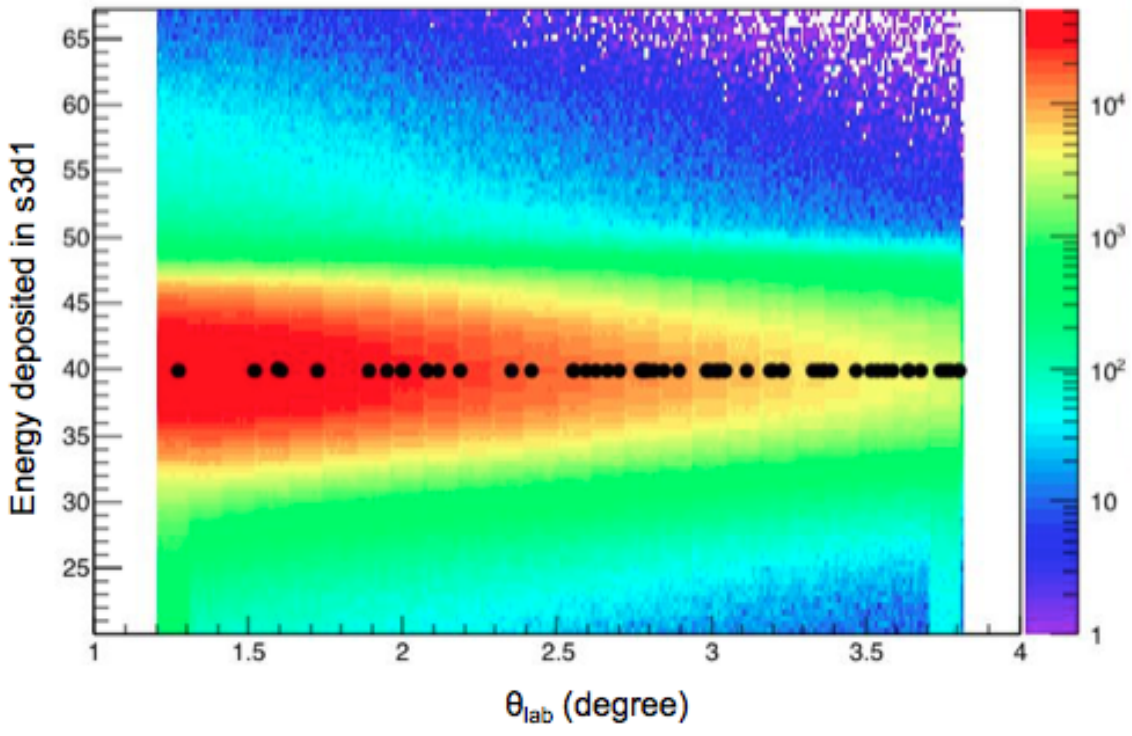

Figure 2.15: S3d1 rings side energy vs angle overlaid with the calculated curve in black

The process of calibrating the S3d2 detector is exactly the same except for the fact that the orientation of S3d2 is opposite to the S3d1 detector in the experiment set up. Its sector side is facing upstream and ring side is downstream with respect to the direction of incoming beam. Since the S3d2 is a thicker detector, the scattered beam-like particles after passing through S3d1, deposit their remaining energy in the S3d2 detector. In this measurement, the scattered ^{19}F particles deposited all of its energy in S3d1 and hence none of the ^{19}F particles reached S3d2. After the calibration of heavier detectors is complete, we have the appropriate energy information required to determine target thickness.

2.3.2 Determining the Target Thickness

It is of vital importance to monitor and determine the target thickness throughout the course of the measurement. The solid hydrogen target may undergo evaporation with time due to radiative heating from ambient room temperature. Of note here is, that the change in beam energy during the course of experiment also affects the calculated variation in target thickness. If the beam energy decreases from the original or desired value, beam loses more energy in the IC. Due to this, the beam comes with lesser energy at the reaction point and deposits lesser energy at S3d1. This effect is reflected as higher calculated target thickness. To evaluate the target thickness, we determine the energy deposited in active layer of S3d1, with and without solid hydrogen target. The difference in the energy deposited in the S3d1 detector corresponds to the energy loss in the target. This energy loss can be used to calculate the thickness of the target using the stopping power as shown in the following

equation

$$\int_{E_i}^{E_f} \frac{1}{S(E)} dE \tag{2.3}$$

where, t is the target thickness, $S(E)$ is the stopping power (equation 2.2) of beam particle passing through solid hydrogen target, E_i and E_f are the energy of ^{19}F obtained by reconstructing before it enters the S3 detector, from the data without and with the solid hydrogen target. The reconstructed energies for ^{19}F from the S3 detector are shown in Fig. 2.16. By fitting the peaks with a Gaussian function, the energy with and without target is obtained.

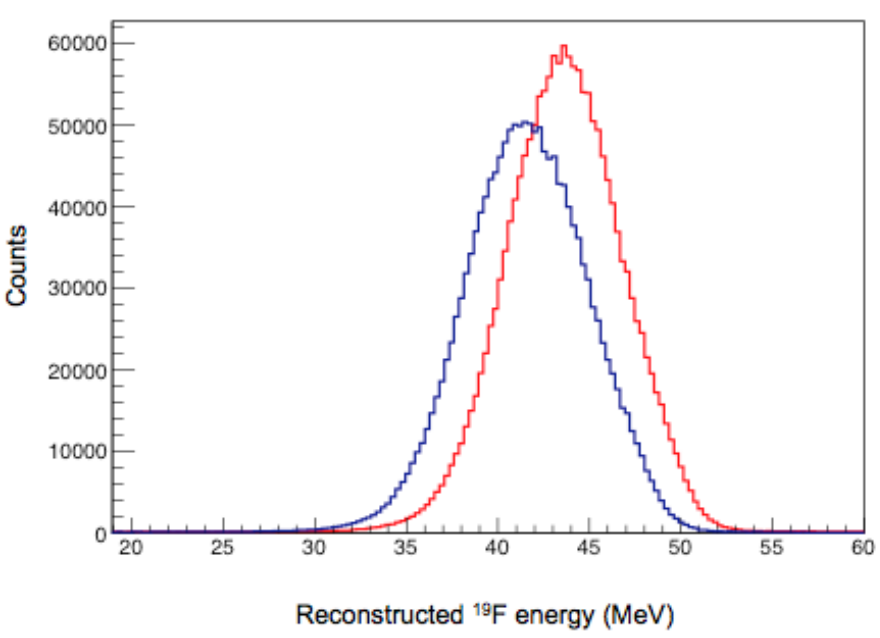

Figure 2.16: Reconstructed ^{19}F energy with (blue) and without (red) solid H_2 target

Figure 2.17 shows the variation in the IC centroid as a function of the data taking period and a sinusoidal pattern is observed. This is analogous to looking at the variation in energy loss of ^{19}F in the IC. This variation comes from the change in density of the isobutane gas. This change in density comes from change in temperature during the day and night cycle over the course of the data collection period. Due to the periodic variation in the density of the isobutane gas, there is a corresponding variation in energy loss of the beam particles in the IC. The periodic variation of temperature recorded in the IC is shown in Fig. 2.18.

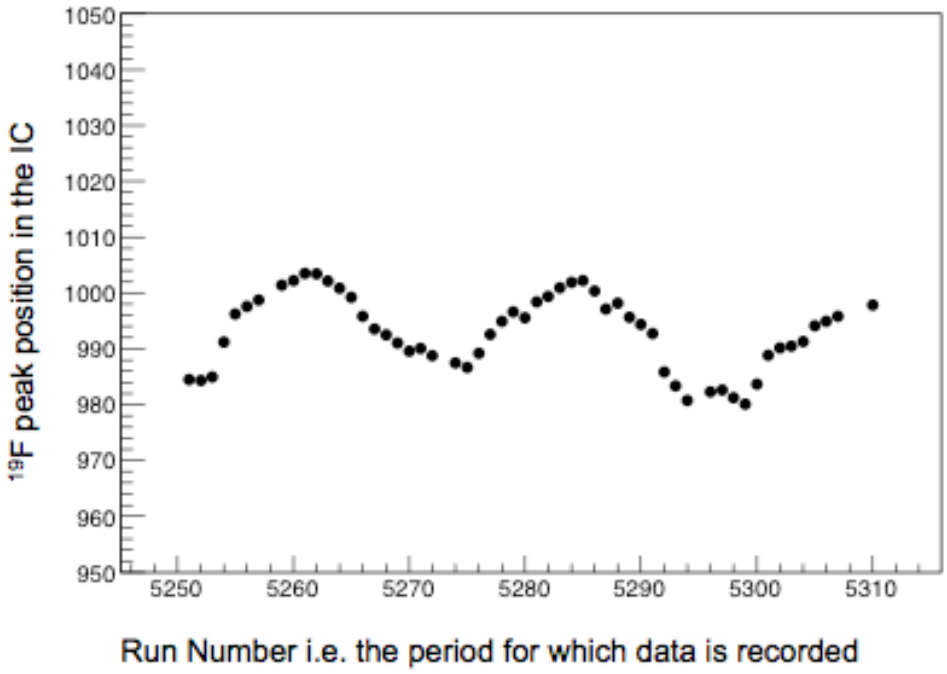

Figure 2.17: Variation of the ^{19}F peak position in the IC during the data collection period

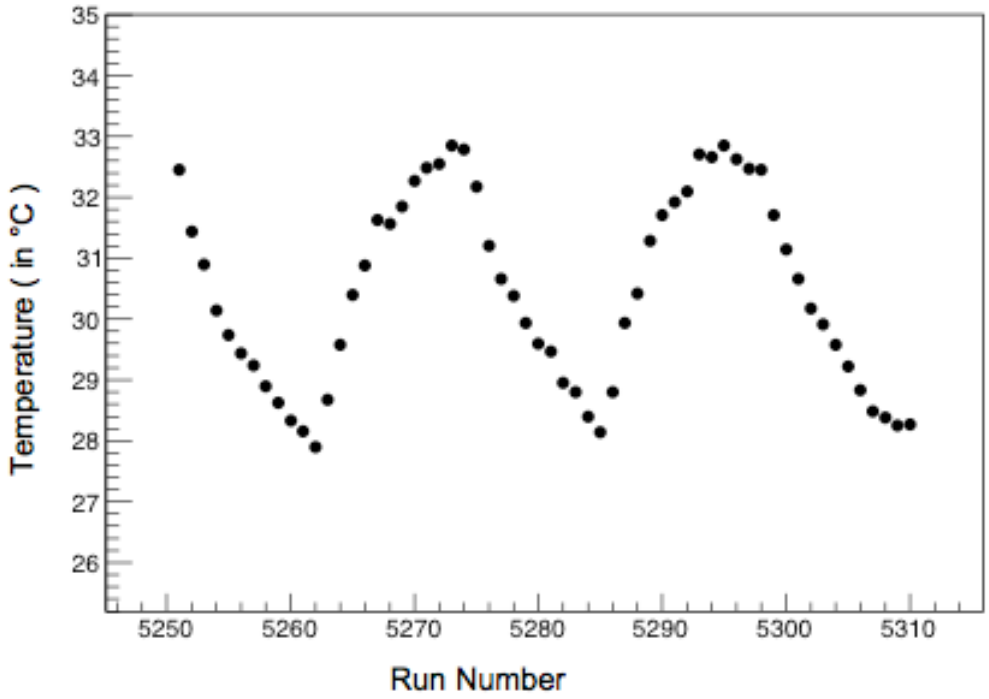

Figure 2.18: Variation in the temperature recorded at IC during the data collection period

Using this information of temperature variation in the IC and combining it with energy loss tables from LISE++, the corresponding energy lost by the beam in the IC is determined. The variation in energy loss during the data taking period shown in Fig. 2.19 follows the pattern of temperature variation.

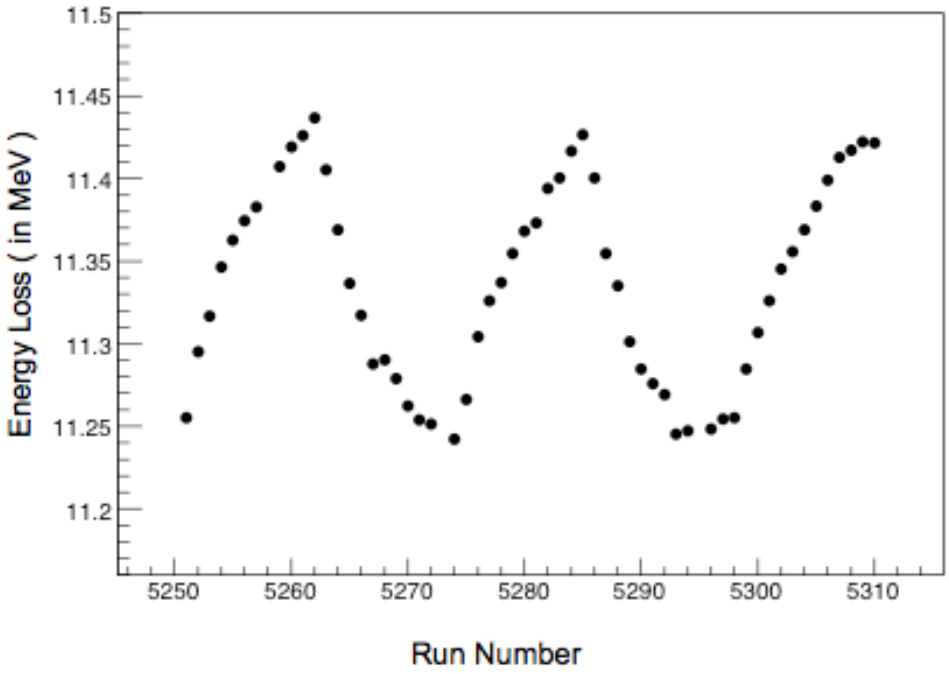

Figure 2.19: Energy loss variation in IC during the data collection period

Since the underlying concept of calculating the target thickness is based on energy loss, a higher energy loss in the IC reflects as higher calculated target thickness. Figure 2.20 shows the target thickness variation in time due to multiple effects. It is important to determine the variation in target thickness because reaction yield depends on it.

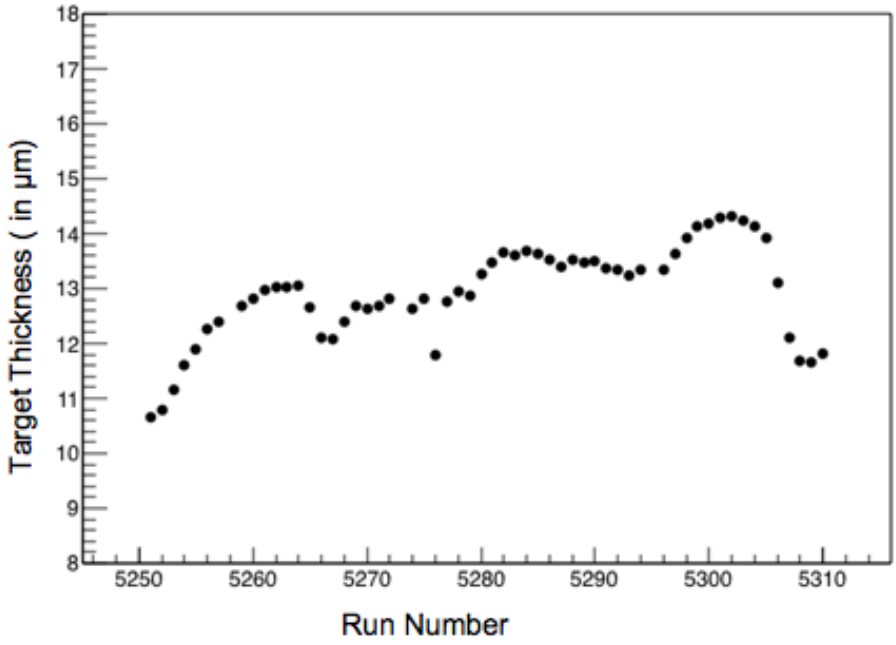

Figure 2.20: The solid H_2 target thickness determined during the data collection period

2.3.3 Calibration of the YY1 Detector

For the calibration of this detector, a triple alpha calibration source was used. It is called triple alpha source because it contains three radioactive isotopes of ^{239}Pu, ^{241}Am, and ^{244}Cm. These isotopes emit alpha particles with energies of 5.155 MeV, 5.486 MeV, and 5.805 MeV respectively. This source is placed in front of the YY1 detector with the help of a source holder. The alpha particles after passing through the dead layers of YY1, lose a very small portion $\sim$ 9 to 11 KeV of energy, and deposit the remaining energy in silicon layer of the YY1. A layout of the materials through which the energy losses of the lighter particles

have been taken into account is shown in Fig. 2.21. The spectrum of the triple alpha source for one of the YY1 detector channels is shown in Fig. 2.22. Each peak is fitted by a Gaussian function and the peak position gives us the channel number. The calculated energy corresponding to each of the peak is known already as mentioned above, the gain is found by using the calibration equation 2.1.

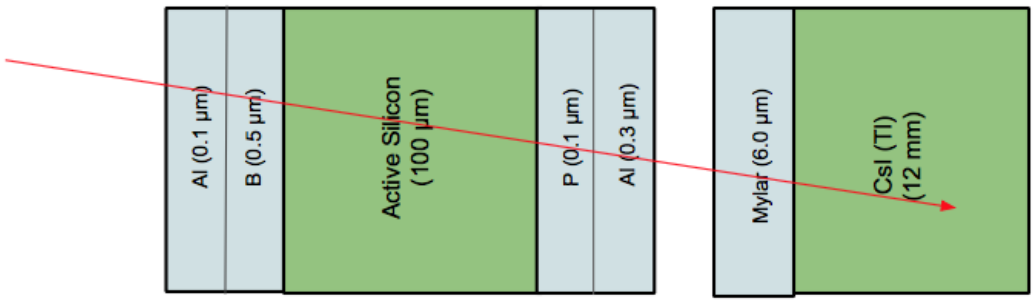

Figure 2.21: Illustration of material layers to account for for calibration of CsI(Tl) detector

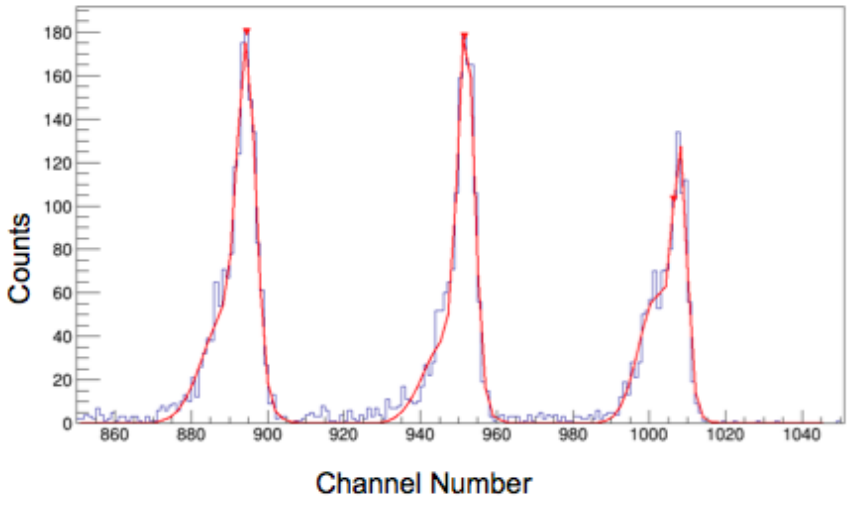

Figure 2.22: ADC spectrum of one ring of YY1 detector and Gaussian Fitting to the peaks

2.3.4 Calibration of the CsI(Tl) Detector

A CsI(Tl) detector is a scintillator detector for which the light collection was done using photodiodes. The calibration of this detector was done by the $^{19}F(p,p)^{19}F$ inelastic scattering reaction by detecting the protons scattered from the hydrogen target. The protons scattered from the random interaction points in the target lose energy in the remaining target thickness, in the YY1 detector dead layer and silicon, in CsI(Tl) covering material and finally deposit the remaining energy in CsI(Tl). By constructing a plot of ADC channel number versus the laboratory angle for all protons measured in the data, the kinematics curves for the ground and excited states of ^{19}F are observed. The measured kinematic curves correspond to the energy deposited by the scattered protons in CsI(Tl). The calculated kinematic curve can be constructed by starting with a total initial energy of the beam, and subtracting the calculated energy losses in the intervening layers. This gives the calculated energy deposited by the protons in CsI(Tl). Figure 2.23 shows the measured kinematics curves for $^{19}F(p,p)^{19}F$ scattering protons in ground state, first excited state (109.9 KeV) and second excited state (197.14 KeV) of ^{19}F combined for all the 16 sectors of CsI(Tl) detector. For calibration purposes, protons scattered in the first excited state of ^{19}F were used.

For each sector of CsI(Tl) detector, once the measured and calculated kinematics curve is obtained, the two can be matched by varying the gain (equation 2.1) as a parameter to get the best fit to the data as shown in Fig. 2.24. The value of the parameter for which the chi-square value is minimized is considered to be the gain of the corresponding sector. This completes the calibration of one sector of CsI(Tl). This process was repeated for each of the

remaining 15 sectors of CsI(Tl) giving an individual gain parameter for each of the sectors. Figure 2.25 shows the calibrated measured spectrum of kinematics of protons overlaid with calculated curve in black.

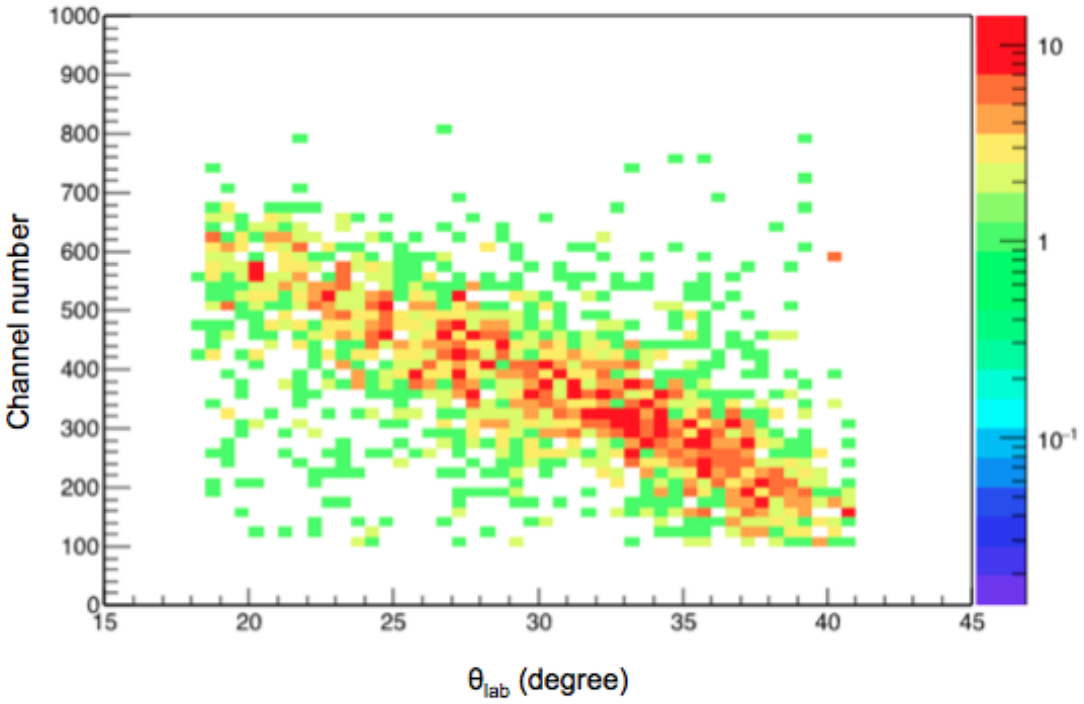

Figure 2.23: CsI(Tl) detector ADC channel number vs Laboratory angle for all 16 sectors of CsI(Tl) detector

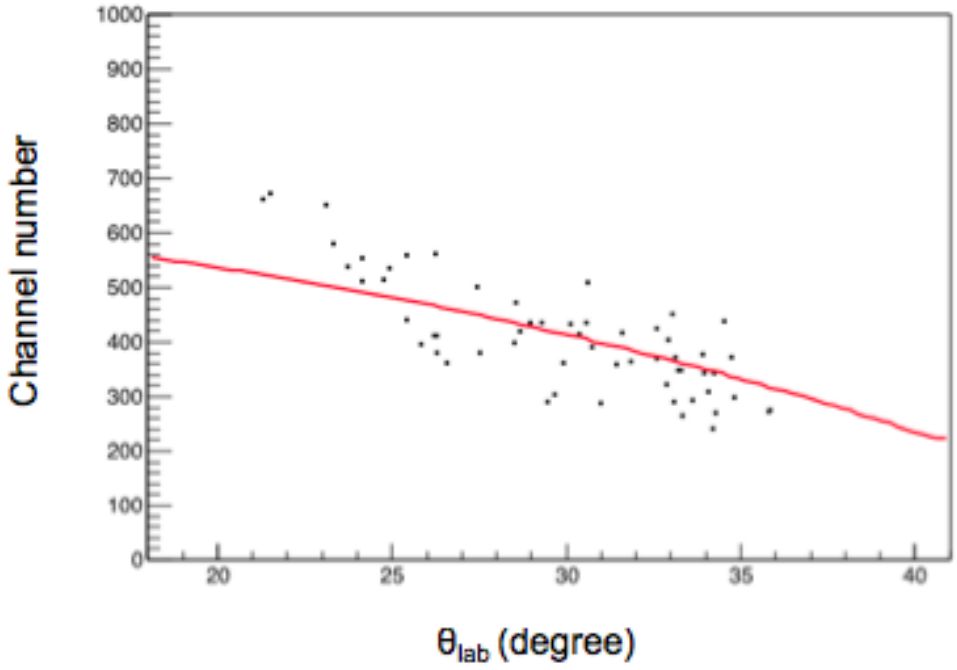

Figure 2.24: CsI(Tl) detector ADC channel number vs Laboratory angle for one of the sectors with calculated curve in red. This calibration is done individually for each of the 16 CsI(Tl) sectors

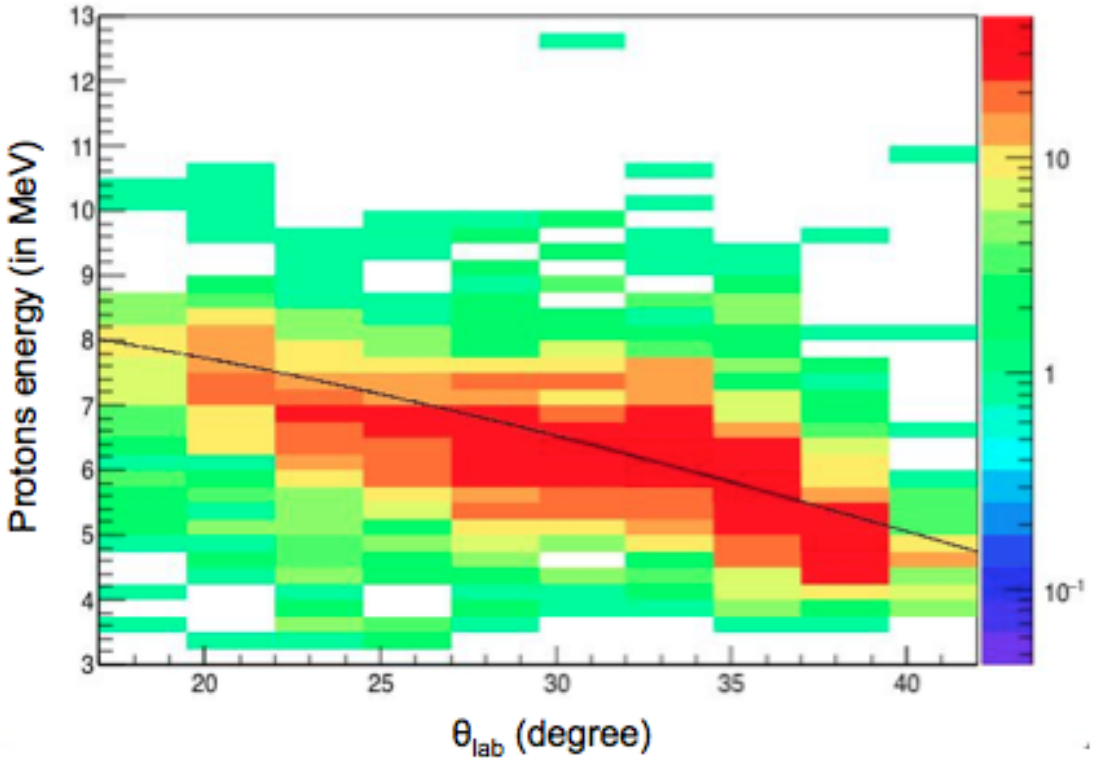

Figure 2.25: The measured energy in CsI(Tl) vs the Laboratory angle of the scattered protons from ^{19}F(p,p)^{19}F scattering. The black curve shows the corresponding calculated curve.

Chapter 3

Data Analysis

In this chapter, analysis of the calibrated data will be discussed. Once both the light and heavy particle detectors are calibrated, next step involves identifying particles emitted from the channel of interest since more than one reaction channels are possible at a given energy. The possible reaction channels in the present measurement are ^{19}F(p,p)^{19}F, ^{19}F(p,p)$^{19}F^*$, ^{19}F(p,α)^{16}O, ^{19}F(p,α)$^{16}O^*$, ^{19}F(p,α)$^{16}O^{**}$ giving protons and alpha particles as the lighter fragments. These particles can be identified by constructing a particle identification spectrum as discussed in the section below.

3.1 Particle Identification Spectrum

We know that the energy loss, ΔE, of a particle in a detector depends on the atomic number of the particle (equation 2.2) and the remaining energy E deposited in a detector depends on

the mass number of the incoming particle (E$\propto\frac{mv^2}{2}$). Therefore, the energy information from the YY1 silicon and CsI(Tl) detector, serving as a ΔE-E telescope, can be used to identify the lighter fragments in the exit channel. The particle identification spectrum as obtained from the data is shown in Figure 3.1. We can clearly see the bands for protons and alpha particles separated in the spectrum. The higher Z particles i.e. alpha particles, are in the upper lying band marked with a polygon cut whereas the particles in the lower tiny band are protons, as identified in this work.

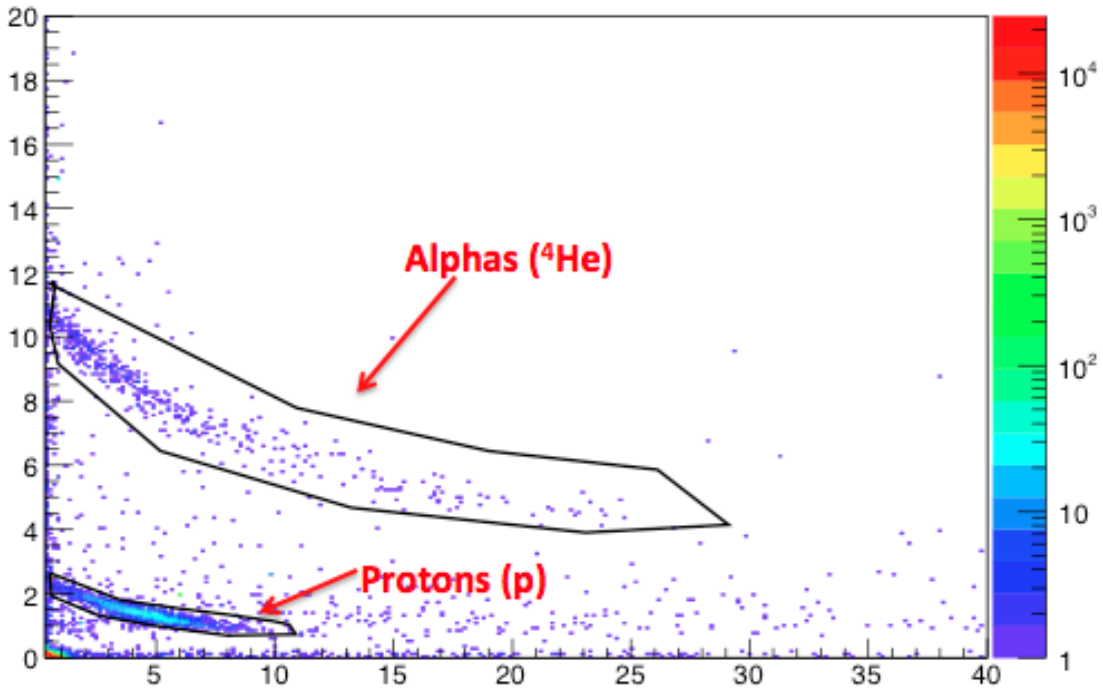

Figure 3.1: Particle Identification Spectrum (PID) for light particles showing a clear identification of protons and alphas inside the polygon cuts

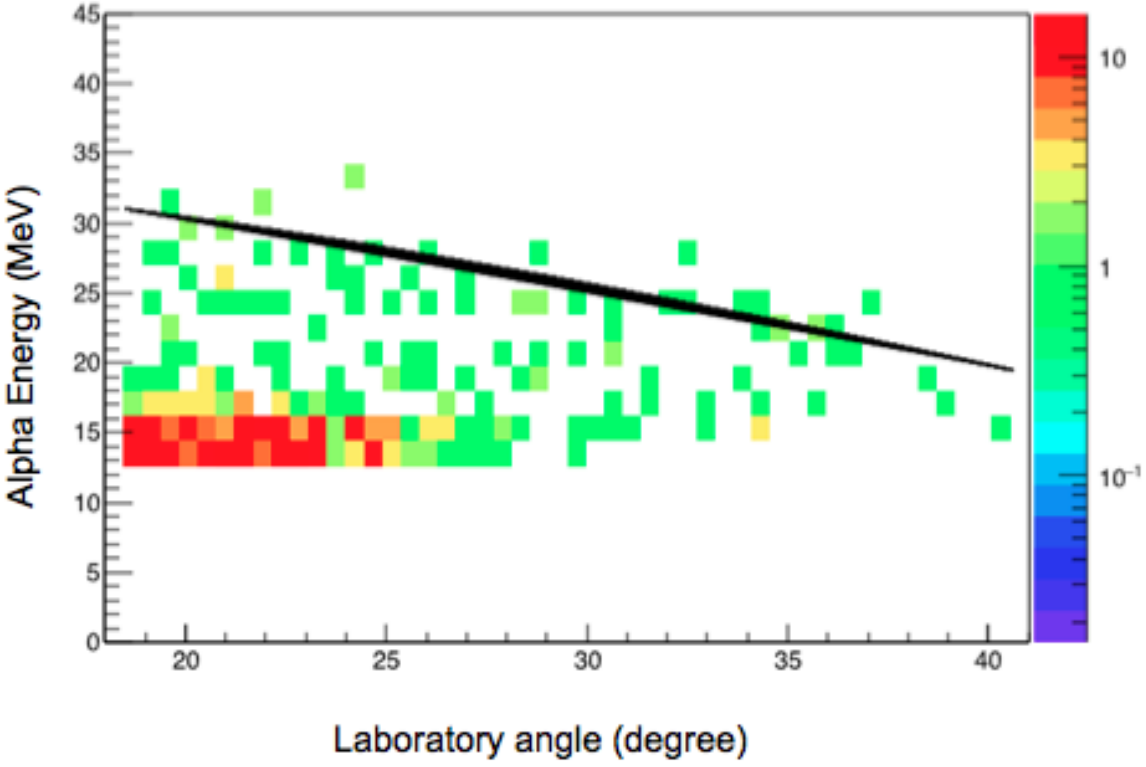

Figure 3.2: Measured kinematics of alpha particles for $^{19}F + p \rightarrow \alpha + ^{16}O$. The black curve shows the corresponding calculated curve only for $^{19}F + p \rightarrow \alpha + ^{16}O_{gs}$

As the detectors are calibrated now, the kinematics of alpha particles can be obtained by plotting the measured energies versus laboratory scattering angles as shown in Figure 3.2.

3.2 Q-value spectrum of ^{19}F(p,α)^{16}O

Q value of a reaction is defined as the difference in the masses of the reactants and products in a reaction. For a reaction a+b→c+d, the Q value can be expressed as

$$Q = m_a + m_b - m_c - m_d \tag{3.2.1}$$

where, m_a, m_b, m_c and m_d are the masses of the species a, b, c and d respectively.

By using the energy and momentum conservation, the RHS of equation 3.2.1 can be written in terms of quantities that can be measured in the experiment. Expressing the equation for Q value in terms of kinetic energy and scattering angle of the fragments measured through YY1 and CsI(Tl) detector, unknown Q-value can be obtained.

$$Q = m_a + m_b - m_c -$$

$$\sqrt{m_a^2 + m_c^2 - m_b^2 + 2m_b(KE_a + m_a) - 2(KE_a + m_a + m_b)(KE_c + mc) + 2P_aP_c cos(\theta)_c} \tag{3.2.2}$$

where, KE_a and KE_c are the kinetic energy of the species a and c, respectively. P_a and P_c are the relativistic momenta of the species a and c, respectively and θ_c is the laboratory scattering angle of species c. This technique to measure the Q value of a reaction is called missing mass technique. The significance of this technique lies in the fact that if any of the particles in the exit channel is in an excited state, then the mass of the excited

particle will be different from its rest mass, based on mass-energy equivalence. In other words, the missing mass of the excited nuclei will be reflected as excitation energy in the Q value spectrum, hence the name. This technique is significant in identifying unknown excited states in nuclei.

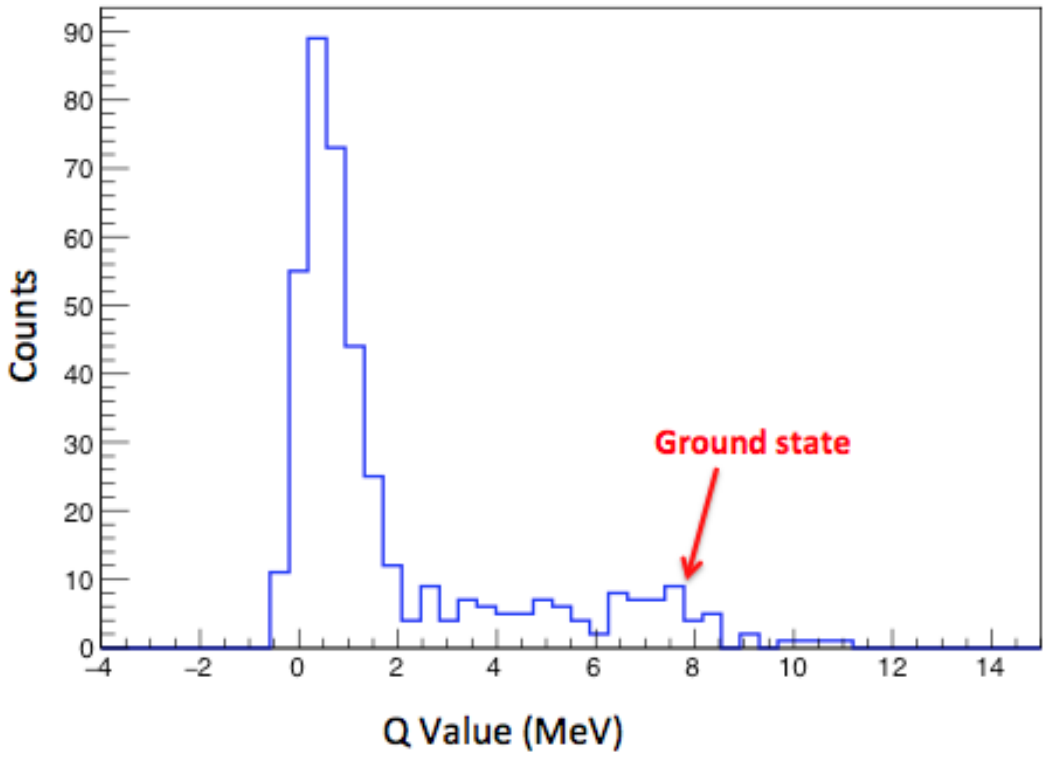

Figure 3.3: Measured Q value spectrum for ^{19}F(p,α)^{16}O

Figure 3.3 shows the measured Q value spectrum of ^{19}F(p,α)^{16}O following the missing mass technique. The ground state Q value for ^{19}F(p,α)$^{16}O_{gs}$ is 8.1 MeV. The structure obtained near 8 MeV potentially corresponds to the ground state of ^{16}O. Since

the channel of interest in this work is ^{19}F(p,α)^{16}O$_{gs}$, better identification of the ground state peak is required. A close look at Fig. 3.2 reveals that the states are relatively better separated at higher laboratory angles, greater than 30 degrees. In other words, the alpha particles corresponding to ^{16}O$_{gs}$ are better separated from the excited state bands, at angles higher than 30°. Using this angle selection, the Q value spectrum is constructed again with a clearer ground state peak showing up around the expected Q value for ground state.

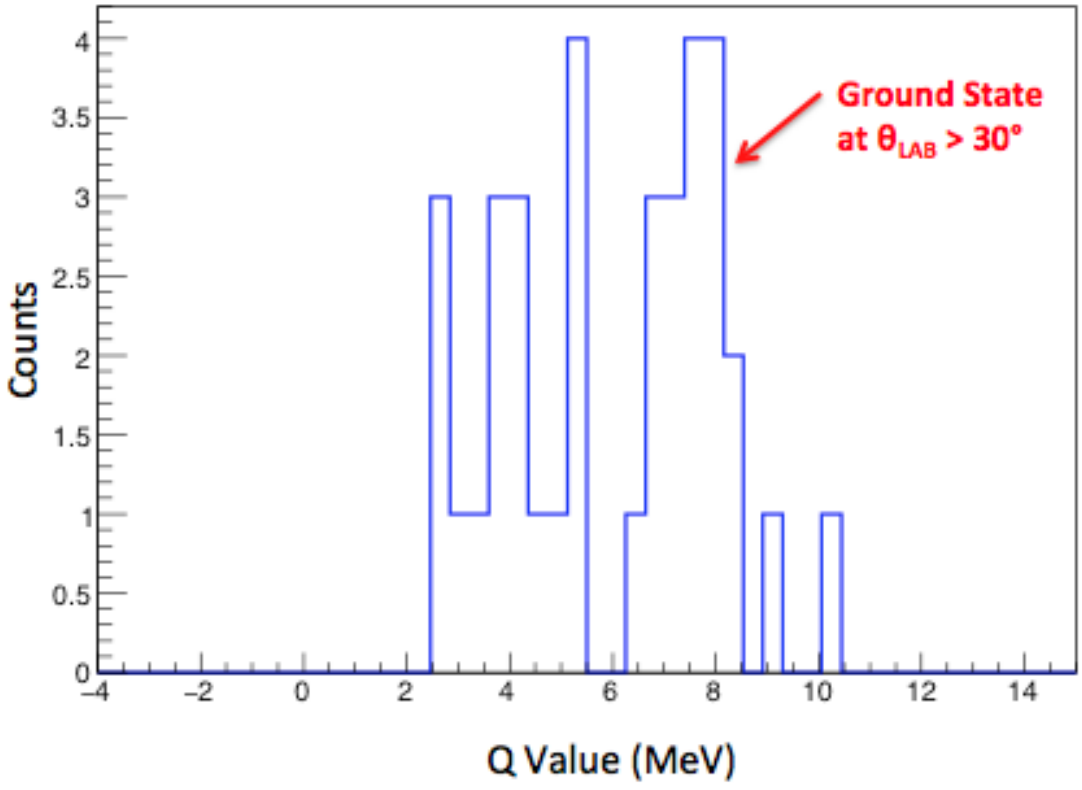

Figure 3.4: Measured Q value spectrum of ^{19}F(p,α)^{16}O with $\theta > 30°$

3.3 Background Subtraction

Since the solid hydrogen target has a backing of silver foil, the fusion-evaporation reactions on the Ag foil could lead to different lighter particles as reaction products. The background alpha particles from ^{19}F+Ag that could contribute to the desired reaction products were measured with ^{19}F beam passing through Ag foil i.e. without any H_2 (without target) data was recorded.

Due to the low statistics of the measured background data, no significant contribution of background alpha particles to the angular coverage of interest was seen. To make a fair assessment of the background contribution in such a situation, the fusion-evaporation code PACE (O. B. Tarasov, 2008) in $LISE++$ was used to simulate the background reaction. As seen in Fig. 3.2, for θ >30°, the energy of measured alpha particles corresponding to $^{16}O_{gs}$ lies in the range around 20 MeV to 35 MeV. When compared to the simulated background spectrum, shown in Fig. 3.5, there are no counts simulated in the respective angular and energy range mentioned above. Therefore, the results from the simulated background spectrum also indicated towards a negligible contribution to the alpha particles coming from ^{19}F(p,α)$^{16}O_{gs}$ in the energy and angular coverage of interest.

In conclusion, the background alpha particles from ^{19}F+Ag were located away from the energy and angular region of interest.

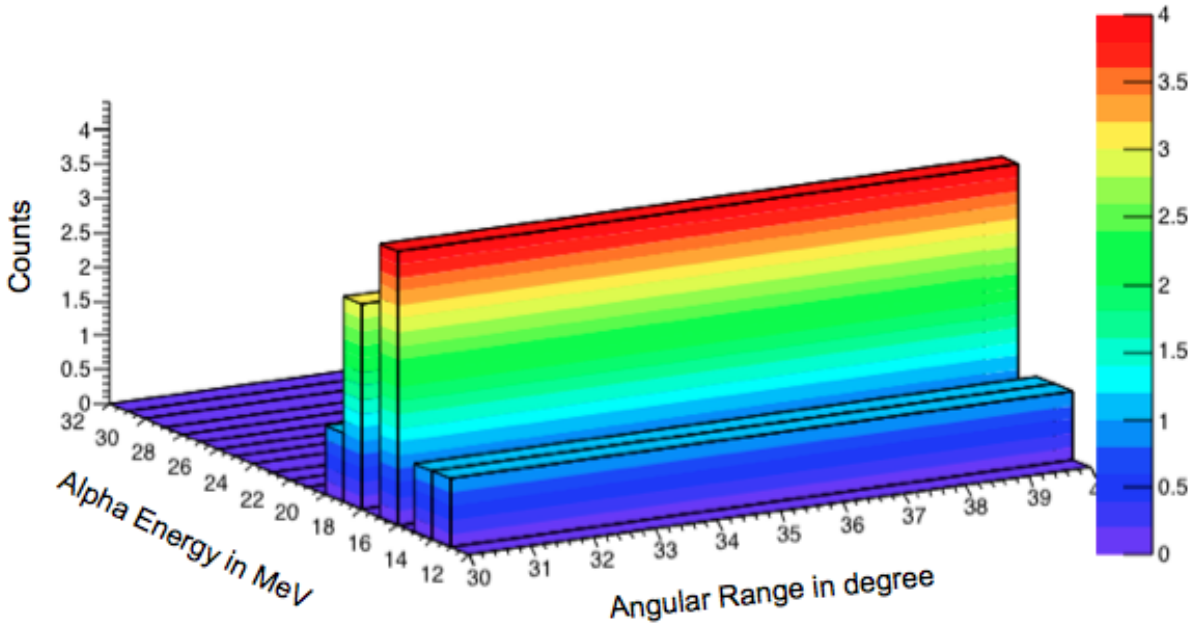

Figure 3.5: Simulated background spectrum from PACE4 (LISE++), showing energy of the alpha particles versus the scattering angle. The color axis here shows the number of simulated counts corresponding to the respective energy and scattering angle as shown in the plot

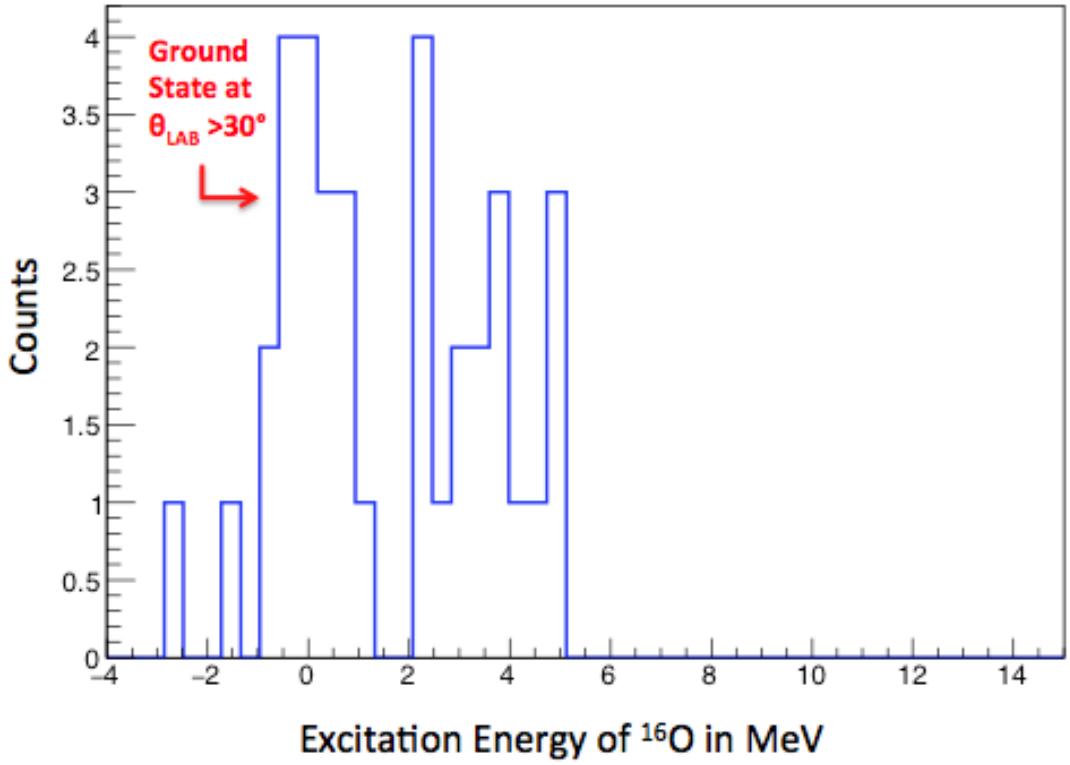

Figure 3.6: Excitation Spectrum of ^{16}O with $\theta > 30°$

In addition, since Q = $Q_{gs} - E_{exc}$, where Q_{gs} corresponds to the Q value of the ground state channel and E_{exc} is the energy of an excited state in the final nucleus, the excitation energy spectrum for ^{16}O can be constructed as shown in Figure 3.6. This spectrum also has the angle selection as θ >30°.

3.3.1 Information from excitation spectrum of ^{16}O

The excitation spectrum for ^{16}O, as shown in Fig. 3.6, highlights the states observed in ^{16}O in this measurement. Since the ground state is better resolved in this spectrum due to the angle selection, the corresponding ground state peak is fitted using a Gaussian function. Once the ground state is identified, the distribution of the total counts in ground state peak over the measured angular range needs to be determined. This is called angular distribution and is vital to find the differential cross-section for the ground state corresponding to (p,α) channel.

3.4 Differential Cross-Section

The interaction of two particles is described in terms of the cross section which gives a measure of the probability for a reaction to occur. The number of particles dN_{sc} scattered per unit time into a solid angle $d\Omega$, given as $d\sigma/d\Omega$, is called differential cross section. It is given by

$$\frac{d\sigma}{d\Omega} = \frac{N_{sc}}{N_{in}} \times \frac{M_t}{N_A} \times \frac{1}{\rho T} \times \frac{1}{d\Omega} \tag{3.4.1}$$

where N_{in} and N_{sc} are the number of incident and scattered particles, respectively.

$d\Omega$ is the differential solid angle, M_t and ρ are the molar mass and density of the solid H_2 target, respectively. N_A is the Avogadro's number and T is the thickness of the

solid H_2 target.

The next step from here onwards is to find the scattering flux or in other words, number of scattered alpha particles corresponding to ^{16}O gs, for each angular bin in the measured Q-value spectrum. For θ >30°, there are 8 angular bins, YY1 detector ring number 9 to 16 i.e. from angle 31.70 to 40.53°. Therefore, Q value spectrum for each angular bin was constructed, giving the ground state peak for each angle. The counts in each angular bin corresponding to the ground state peak were determined. By fitting the ground state peak in each spectrum for each bin, the 3σ region around the mean is determined. This region around the mean in the Gaussian function covers 99.7 % of the area under the peak and it is the number of particles within this range, that are counted for each angular bin.

To find the total number of incident ^{19}F, scaler information recorded during the experiment is required. The IC scaler counter records the number of incoming particles which includes the beam particles of interest along with other constituents in the beam. The other constituents could be isobaric contaminants along with the beam. To get the number of incoming ^{19}F particles out of the total, a selection gate in terms of ADC channel numbers on ^{19}F peak in the IC spectrum is used to scale the total counts recorded in IC. This ratio, however, needs to be corrected by data acquisition (DAQ) live time. It is important to include this correction because data acquisition system requires a finite amount of time to process and store an event before it can accept the next one. This means that it cannot process all the events incident on the detectors. Therefore, this correction is crucial to avoid overestimating the number of incoming ^{19}F particles.

The DAQ live-time is given by

$$\tau = \frac{Total\,Accepted\,Trigger}{Total\,Free\,Trigger}$$

Therefore, for each run i, incident ^{19}F particles are given as

N_i^{19F} = (IC Scaler counts in the ith run)$\times\tau_i\times N_i^{ADC(19F)}$ /$\mathrm{N}_i^{ADC(Total)}$

Once N_i^{19F} is obtained for each run, it is summed over all the runs to get total N_{in} incident during the entire data collection time, expressed as

$\mathrm{N}_{in} = \sum_i \mathrm{N}_i^{19F}$

Since the target thickness may change (decrease) over time, this variation is included and the expression above gets modified as

$\mathrm{N}_{in}\times\mathrm{T}_i = \mathrm{N}_1^{19F}*\mathrm{T}_1+\mathrm{N}_2^{19F}*\mathrm{T}_2+$ .....

where T_i is the solid H_2 target thickness for i^{th} data run

The solid angle in a range dθ at an angle θ is given by

$\mathrm{d}\Omega = 2\times\pi\times\sin\theta_{lab}\times\mathrm{d}\theta$lab where,

$$d\theta_{lab} = \theta_{max} - \theta_{min} \tag{3.4.2}$$

and

$$\theta_{lab} = (\theta_{max} + \theta_{min})/2 \tag{3.4.3}$$

θ_{max} is the maximum and θ_{min} is the minimum angle subtended by the upper edge and lower edge respectively, of each ring of the YY1 silicon detector. θ_{lab} as shown in equation 3.4.3 is the mean angle at the center of the ring.

3.4.1 Uncertainty in the measurement of differential cross section

From the expression for differential cross section as in equation 3.4.1, it is concluded that the uncertainty in the measurement of differential cross section should be propagated from the uncertainty in the variables used in that expression. This implies uncertainty in the number of scattered particles N_{sc} and solid H_2 target thickness T. The uncertainty in N_{sc} is a statistical uncertainty based on the number of counts in an angular bin. On the other hand, the uncertainty in determining target thickness depends on the uncertainty in determining the energy of scattered particles. As this energy value is used to calculate target thickness, therefore, uncertainty in this quantity arises from the variation in energy loss tables. This uncertainty is systematic, approximated to be 5% reflecting the uncertainty from stopping power tables. Note that the uncertainty in total number of incident particles, N_{in} is negligible and therefore not accounted for. Hence, the final expression for finding the uncertainty in the measurement of the differential cross section can be written as

$$\Delta(\frac{d\sigma}{d\Omega}) = \frac{d\sigma}{d\Omega} \times \sqrt{\frac{\sigma^2_{Nsc}}{N^2_{sc}} + \frac{\sum_i \sigma^2_{Ti} \times (N_i^{19F})^2}{(\sum_i N_i^{19F} \times T_i)^2}} \tag{3.4.4}$$

where,

$$\sigma^2_{Nsc} = N_{sc}$$

$$\sigma^2_{Ti} = \frac{25}{10000} \times T_i^2$$

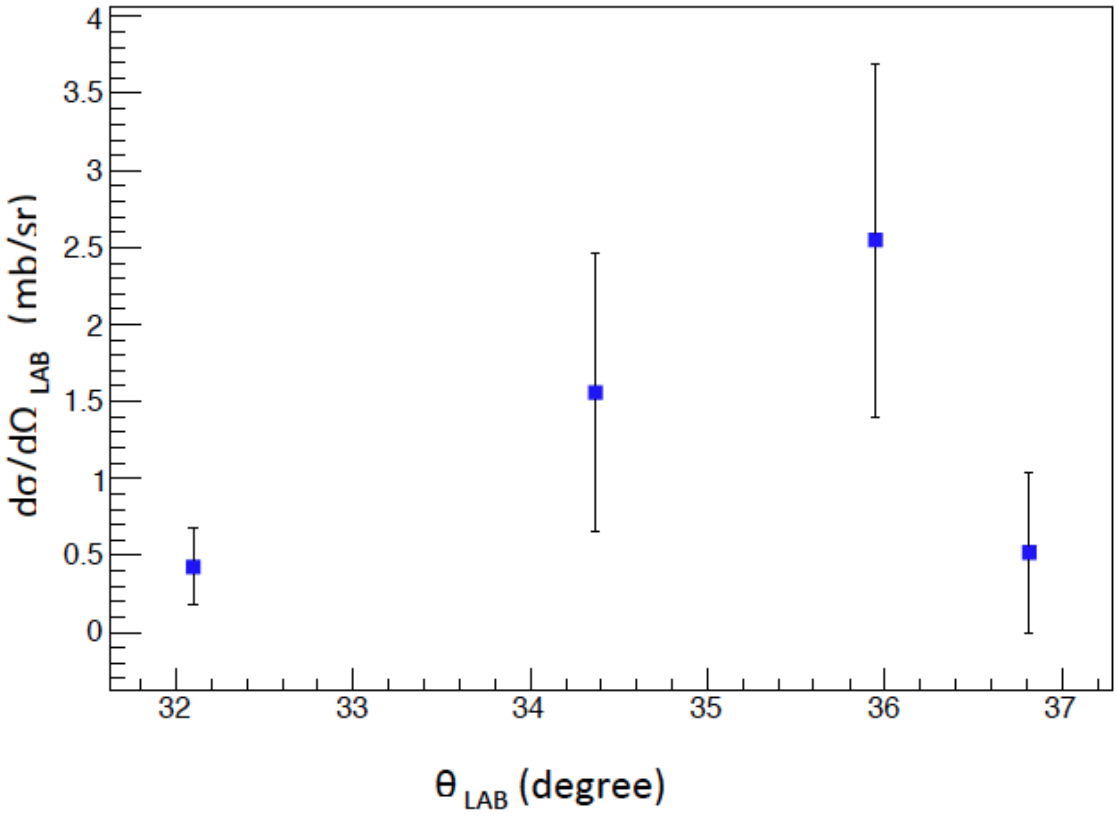

Figure 3.7: Measured angular distribution for ^{19}F(p,α)^{16}O$_{gs}$ in laboratory frame

These two uncertainties are mutually independent and were added together quadratically to obtain the total uncertainty as shown in equation 3.4.4. The systematic uncertainty did not add a significant amount to the total uncertainty. The low counting statistics accounted for majority of the uncertainty at every data point.

It is important to transform results for the measurement of differential cross sections from the laboratory frame into the center of mass frame, for comparison with the results of theory calculations, as the theory is calculated in the center of mass frame. When going from the laboratory frame to the center of mass frame, it is not only a transformation of measured angles but the corresponding solid angle is transformed. Consequently, the differential cross sections in the laboratory system are not identical to those in the center of mass system. The conversion of the cross sections obtained in the laboratory system to those in the center of mass frame are based on the ratio of the solid angles obtained in these two frames. The ratio of differential factors that describes this transformation is known as the Jacobian. The Jacobian is defined as

$$J_{lab->cm} = \frac{d\Omega_{lab}}{d\Omega_{cm}} = \frac{sin\theta_{lab} \times d\theta_{lab}}{sin\theta_{cm} \times d\theta_{cm}} \tag{3.4.5}$$

This expression relates laboratory angles to center of mass angles which can be obtained from kinematics calculations. Figure 3.8 shows the relation between laboratory and center of mass angles for ^{19}F(p,α)^{16}O$_{gs}$ with the Jacobian shown in Fig. 3.9 as evaluated by equation 3.4.5.

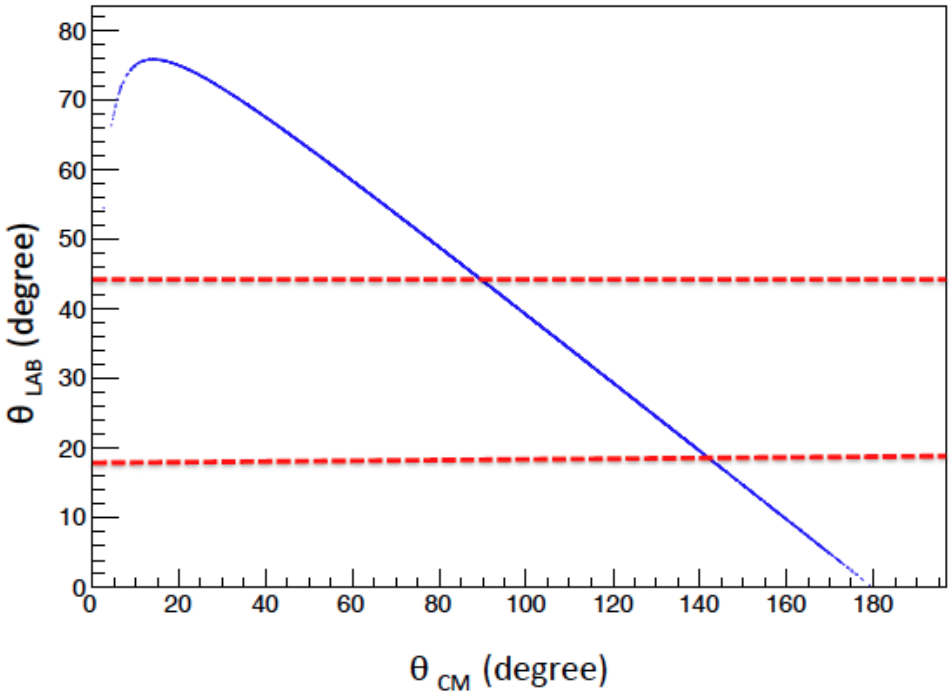

Figure 3.8: Laboratory angle vs center of mass scattering angle with the detector coverage marked in red dashed lines

Using the Jacobian of transformation, the differential cross section in the center of mass frame is obtained as

$$\frac{d\sigma}{d\Omega_{cm}} = \frac{d\sigma}{d\Omega_{lab}} \times \frac{d\Omega_{lab}}{d\Omega_{cm}} \tag{3.4.6}$$

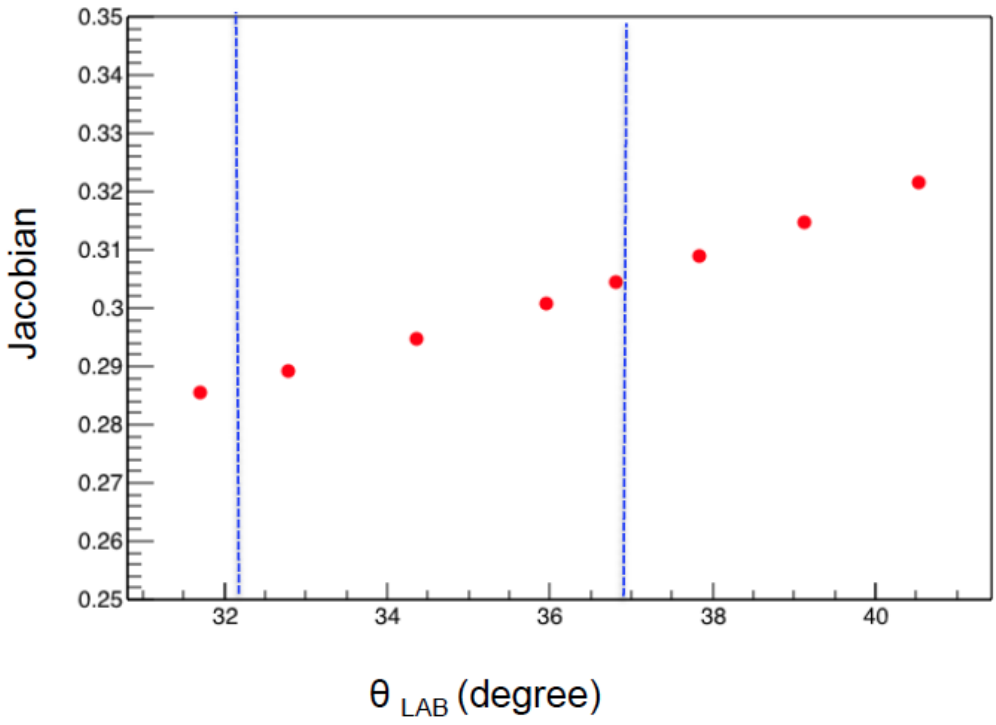

Figure 3.9: The Jacobian of transformation from the laboratory frame to the center-of-mass frame vs laboratory angle

The differential cross section in the center of mass frame obtained using equation 3.4.6 versus the center of mass scattering angle is shown in Fig. 3.10.

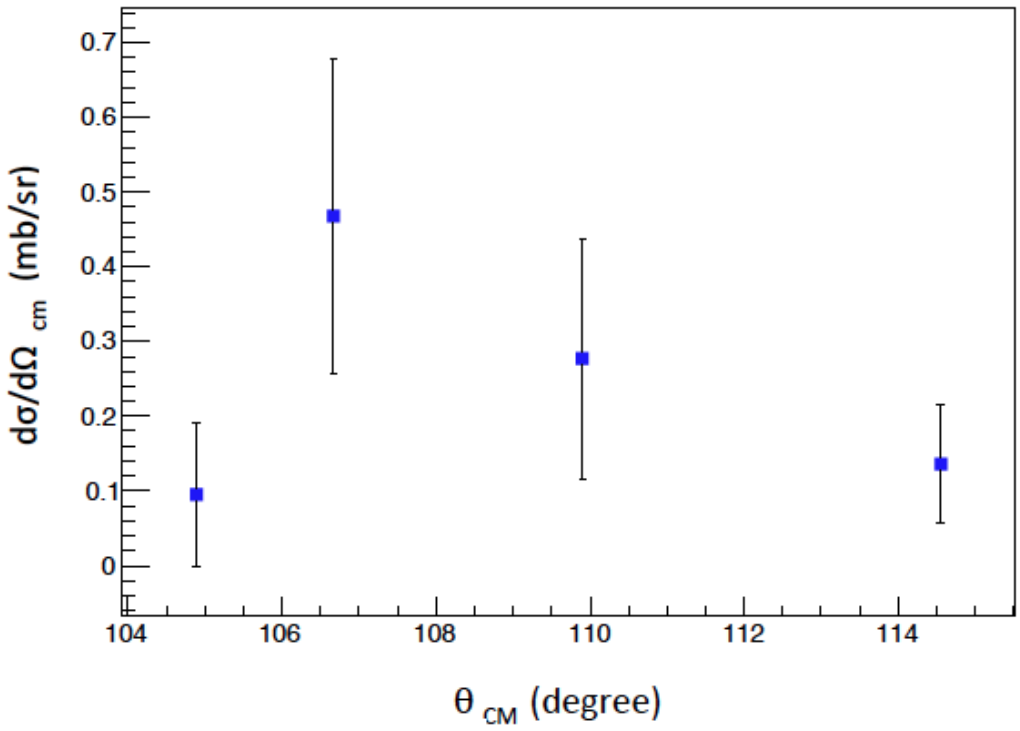

Figure 3.10: Differential cross section in center of mass frame for $^{19}F(p,\alpha)^{16}O_{gs}$

The total uncertainty associated with the cross section in center of mass system were then evaluated by multiplying the relative uncertainties in the cross section in the laboratory system by the cross section in the center of mass system.

3.5 Discussion

To obtain nuclear physics information such as total cross section from the experimental differential cross sections, the measured angular distribution is interpreted in the framework of a theoretical formalism. Nuclear reaction theories, in general, describe the interactions

between nucleons in terms of two fundamental forces, the electromagnetic and strong nuclear force. The electromagnetic force or Coulomb interaction between charged particles, is well understood, whereas the strong nuclear force involved is not precisely known and is complex. The nucleon-nucleon interaction exhibits both attractive and repulsive behaviour varying with distance between incident particle and a nucleus. To calculate every interaction between nucleons, approximations using optical potentials are used. These potentials are based on a smooth, functional form for the energy dependence of the potential depths, and on physically constrained geometry parameters. These parameters are customized to a specific energy of a reaction and are not generalized to all the nuclear interactions (A. J. Koning and J. P. Delaroche, 2003).

This section provides an overview of the components in the nuclear reaction formalism needed to interpret the experimental results. The theoretical model that is used to describe transfer reactions is the Distorted Wave Born Approximation (DWBA) theory. The assumptions for the reaction mechanism are presented with an introduction to direct reactions theory followed by a discussion of basic concept of optical model.

3.5.1 Direct Reaction Theory

Direct reaction theory attempts to describe a given process when two nuclei collide with the entrance and exit channels described as waves scattered by a nuclear potential. These two nuclei are the projectile and target nuclei and those subsequent pairs of nuclei that may be obtained by transferring one or more nucleons between them. The potential between the

participating nuclei is the distorting potential used to generate the distorted waves through the Schrodinger equation. This is called Distorted Wave Born Approximation (DWBA). The simplest scattering theory is in terms of a plane wave Born approximation. An improved model replaces the plane waves by the wave solutions that are distorted by the presence of the scattering potential, giving the DWBA. The main idea of the DWBA model is that the main parts of the reactions are elastic scattering and that all other channels are weak perturbations governed by an imaginary potential which removes particles from the elastic channel. The interaction potential used in DWBA is an optical potential which consists of a real and imaginary part (G. R. Satchler, 1983). To determine the scattering cross-section, an appropriate potential must be chosen. Shown below is a general form of the potential consisting of a Coulomb and nuclear part. The nuclear part of the potential includes both a real and an imaginary component as

$$U(r) = Vc(r) + V(r) + iW(r)$$

where, $Vc(r)$ is the Coulomb Potential. $V(r)$ and $W(r)$ are nuclear potential functions that give the potential the correct radial dependence. Here, $V(r)$ is the real component and $W(r)$ is the imaginary component. Typical forms of $V(r)$ and $W(r)$ are the Woods-Saxon potentials (C. M. Perey, 1976).

3.5.2 Optical Model

The scattering theory is treated in an optical model approach, where scattering potential is complex and has attractive and absorptive components. As in optical light being scattered from a cloudy crystal sphere, the calculation resembles that of light incident on a somewhat opaque glass sphere. The loss of flux, by any process is represented by the imaginary part of the potential (K. S. Krane, 1988). Scattering potentials with both an imaginary and real component are called optical potentials due to the resemblance with the description of the optical refractive index of light because a similar description works for nuclear scattering with particles. The interaction potential is a many-body problem but in the optical model, the potential is described by a smoothed average of the actual interaction. The potential consists of four types of interactions - an attractive nuclear interaction term V_r, an imaginary surface absorption term W_D, a spin-orbit term V_{SO}, and a Coulomb potential V_C.

$$U(r) = V_c\text{-}Vf(x_o)+(h/m_\pi c)^2 V_{so}(\sigma.l)\tfrac{1}{r}\tfrac{d}{dr}f(x_{so})$$

$$-i[(Wf(x_W) - 4W_D\frac{d}{dx_D}f(x_D)]$$

where, $V_c = Z_1Z_2e^2/r$ for $r \geqslant = (Z_1Z_2e^2/2R_c)(3\text{-}r^2/R_c^2$ for $r \leqslant R_c$

$R_c = r_cA^{\frac{1}{3}}$

$f(x_i) = (1+e^{x_i)^{-1}}$ where $x_i = (r\text{-}r_iA^{\frac{1}{3}})/a_i$

This model washes out the many-order degrees of freedom in a nucleus and replaces the nucleus with a mean field plus any valence nucleons relevant to the reaction. The final state populated in a reaction is represented as a core (being the original target nucleus) with the transferred nucleon in an eigen state of the potential that arises due to the core. DWBA transfer cross sections are very sensitive to the optical potential parameters. The angular distributions from different optical potentials can vary significantly. (G. R. Satchler, 1983). The outcome of a direct reaction depends strongly on the way it is initiated. The cross section of the exit channel b+B is strongly dependent on the entrance channel i.e. on the overlap of the initial and final wave functions.

To analyze the ^{19}F(p,α)^{16}O$_{gs}$ transfer reaction, DWBA is used. The measured angular distribution was interpreted using the code FRESCO (I. J. Thompson, 1988). The parameters used in the calculation are determined from elastic scattering data for the entrance and exit channels. The best fitted calculated elastic scattering angular distribution provides the optical potential parameters. These parameters are then used to calculate the transfer reaction angular distribution for the entire center of mass scattering angular range of 0°to 180°. Once theoretical angular distribution is calculated, it is compared to the measured angular distribution to extract nuclear spectroscopic information.

Large sets of elastic scattering data that have been compiled for particular mass and energy ranges, are used to deduce global optical model parameterizations. The primary optical model parameterization used in this analysis is that of Koning-Delaroche (A. J. Koning and J. P. Delaroche, 2003).

These phenomenological optical model potentials are for neutrons and protons with incident energies from 1 keV upto 200 MeV, for (near-)spherical nuclides in the mass range $24 < A < 209$. These are based on a smooth, unique functional form for the energy dependence of the potential depths, and on physically constrained geometry parameters.

Figure 3.11 shows the calculated angular distribution for $^{19}F(p,\alpha)^{16}O_{gs}$ using the parameters from Koning & Delaroche.

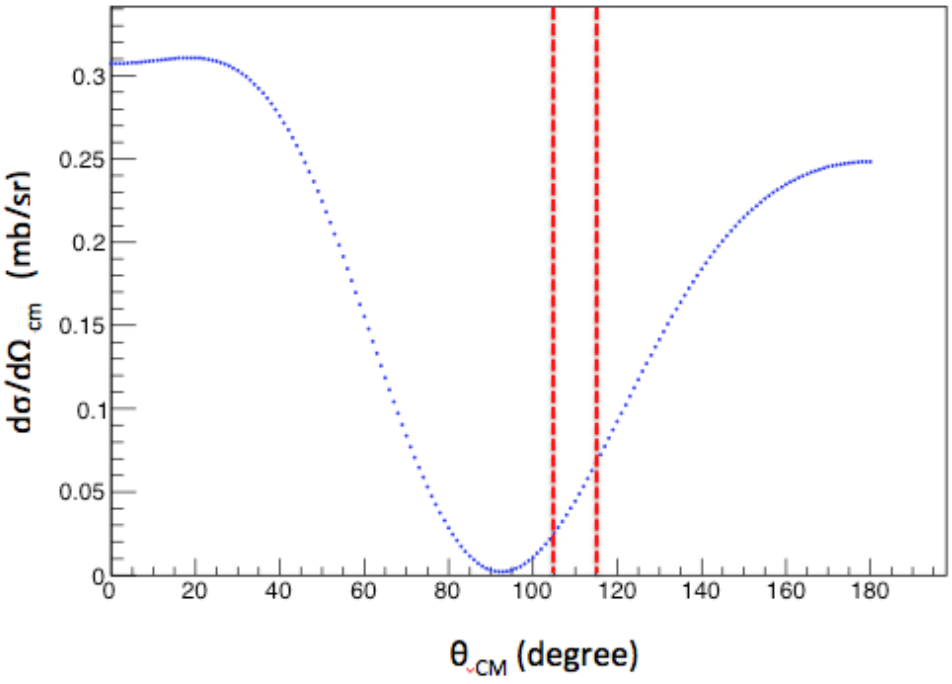

Figure 3.11: Calculated angular distribution for $^{19}F(p,\alpha)^{16}O_{gs}$ using Koning-Delaroche global optical model in DWBA framework using FRESCO, with dashed lines in red showing the angular range, in center of mass, measured in this work

To obtain the spectroscopic factor, S, the calculated angular distribution is nor-

malized to the experimentally measured data for angular distribution of ^{19}F(p,α)^{16}O$_{gs}$. The calculations consider pure shell model configurations but the actual nuclear states that are populated can have a mixed configuration. In other words, it means that the DWBA calculations employed in this work assume a unit normalization as the definition of the spectroscopic factor. Therefore, S_{exp} here is a normalization factor other than one, giving a scaling factor between the theoretical calculation and the data, which gives experimental value for the spectroscopic factor.

The spectroscopic factor is then obtained using the expression as shown below

$$\frac{d\sigma}{d\Omega}_{(exp)} = S_{exp}\frac{d\sigma}{d\Omega}_{(theory)} \tag{3.5.1}$$

i.e. by comparing the calculated DWBA cross sections with measured values of angular distribution. For this kind of comparison, the $\chi 2$ based statistics are used. The normalization is done by minimizing the chi-square, evaluated up to one standard deviation (1 σ) that each data point lies from the model (X. D. Liu et al, 2004).

Two statistical methods for extracting normalization factor by chi-square minimisation are used in this work, Least squares chi-square minimization and Maximum likelihood ratio chi-square minimization. Both these methods are different in terms of their basic principle but, when data points follow the normal distribution, these two methods are equivalent.

Least squares minimisation is more applicable when the data distribution is as-

sumed to be Gaussian. For least squares parameters estimation, the line that minimizes the total squared distance between the data points and theory is found. Since the Gaussian distribution is symmetric, this is equivalent to minimising the distance between the data points and the mean value. On the other hand, if the data distribution is assumed to be following Poisson Distribution, maximum likelihood method is considered more appropriate. In maximum likelihood estimation, the total probability of the data is maximised. A parameter called maximum likelihood estimator for the theoretical distribution is found, that maximises the probability of data coming from it.

To summarize, the χ^2 method estimates the variance of a given data point from the theoretical value. In contrast, the likelihood function does not employ the variance, but rather the probability distribution itself. A brief description of each method will be discussed in the next sections.

3.6 Least Squares Chi-Square χ2 Histogram Fitting

The chi-square test, as used in this work, is based on the difference between the observed and the expected values of differential cross section in center of mass frame for each center of mass angle.

The chi-square statistic is defined as

$$\chi^2_{LS} = \sum_i^n \frac{(Measured_i - Calculated_i)^2}{(\sigma_{measured})^2} \tag{3.6.1}$$

where, Measured$_i$ is the measured differential cross section and Calculated$_i$ is the calculated differential cross section, at each center of mass angle. $\sigma_{measured}$ is the measured uncertainty at each i i.e. at each data point.

A redefined statistic from chi-square, defined as reduced chi-square is used.

$$\chi^2_\nu = \frac{\chi^2}{\nu} \tag{3.6.2}$$

with an expectation value of $\chi^2_\nu = 1$. Here, ν refers to the number of degrees of freedom and is equal to the total number of data points minus the number of constraints. In this work, $\nu = n - 1$ has been used in the evaluation of reduced chi-square.

3.7 Likelihood Ratio χ2 Histogram Fitting

Maximum likelihood estimation is a method that determines values for the parameters of a model. The parameter values are found such that they maximize the likelihood that the process described by the model produced the data that were actually observed. The values that are found in this process are called maximum likelihood estimate (MLE). The method of Maximum likelihood is used assuming that the data have been binned into histograms.

The histogram has k bins labelled by the index i running from 1 to k with n_i as the number of events in the i^{th} bin. The task is to fit to the theoretical curve which yields y_i as the number of events predicted by the model to be in the i^{th} bin and α as the parameter that is varied. The central assumption of this method comes from the constraint imposed by the limitation on counting statistics. For the analysis of low-statistics data, the likelihood ratio analysis is more appropriate. For independently Poisson-distributed data, the likelihood function is given by

$$L(y;n) = \prod_{i=1}^{k} \frac{y_i(\alpha)^{n_i} exp(-y_i(\alpha))}{n_i!}$$

for some choice of model y. If m is taken to be the true value of n, then the likelihood ratio Λ is defined as

$$\Lambda = \frac{L(y;n)}{L(m;n)}$$

The likelihood ratio test theorem says that the likelihood chi-square is defined by

χ^2_Λ = -2 lnΛ = -2 ln L(y;n)+2 ln L(m;n)

and it asymptotically obeys a chi-square distribution.

where, n_i represents the observed data and $y_i(\alpha)$ representing the model data in bin i. The objective of the process reduces to minimizing the chi-square which means

maximizing the likelihood function (S. Baker and R. D. Cousins,1983).

Once the MLE n value is evaluated for each bin, then the above expression becomes

χ^2_Λ = -2 lnΛ = -2 ln L(y;n)+2 ln L(n;n)

$$= 2\sum_{i=1}^{k} y_i(\alpha) - n_i + n_i ln\frac{n_i}{y_i(\alpha)}$$

n_i represents the observed data and $y_i(\alpha)$ represents the model data in bin i.

3.8 Results for Normalization Factor

In this section, the theoretical angular distribution using global optical proton potential is used, to obtain a normalization factor, by comparing to the measured differential cross section in the center of mass.

In section 3.8.1, both the above discussed methods are used to obtain a normalization factor between the measured and calculated theoretical angular distribution using Koning-Delaroche global optical model. A careful comparison of the results obtained through both minimization methods establishes the better applicability of maximum likelihood method, as discussed in in section 3.8.2.

In section 3.8.3 - 3.8.5, only maximum likelihood method is used for comparison between the measured and calculated theoretical angular distribution using Menet et al. (J.

J. Menet et al., 1971), Becchetti-Greenlees (F. D. Becchetti et al., 1969), Perey (F. G. Perey, 1963) global optical models.

3.8.1 Koning-Delaroche, 2003

To obtain the value of normalization factor, calculated angular distribution using Koning-Delaroche global model was used. Both the above discussed chi-square minimization methods were employed. Figure 3.12 and Fig. 3.13 show the χ^2_{LS} and χ^2_{Λ} plotted against the normalization factor for ^{19}F(p,α)$^{16}O_{gs}$ differential cross section. These figures reveal the value of normalization factor obtained against the chi-square, clearly showing the minimum in chi-square distribution.

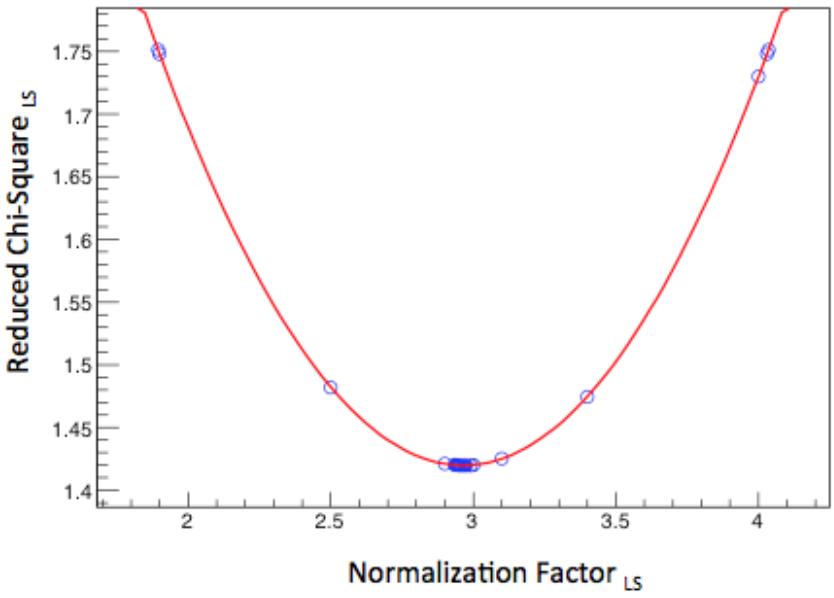

Figure 3.12: Least squares chi-square minimization: Reduced chi-square values versus the normalization factor for each chi-square, obtained from the comparison of measured and calcuated angular distribution for Koning-Delaroche global proton optical potential. The red curve shows fitted polynomial of degree 2.

Normalization Factor	Chi-Square	Reduced Chi-Square
1.90	5.25	1.75
2.96	4.25	1.42
4.03	5.25	1.75

Table 3.1: Least squares minimization chi-square values corresponding to each normalization factor obtained through least squares chi-square minimization

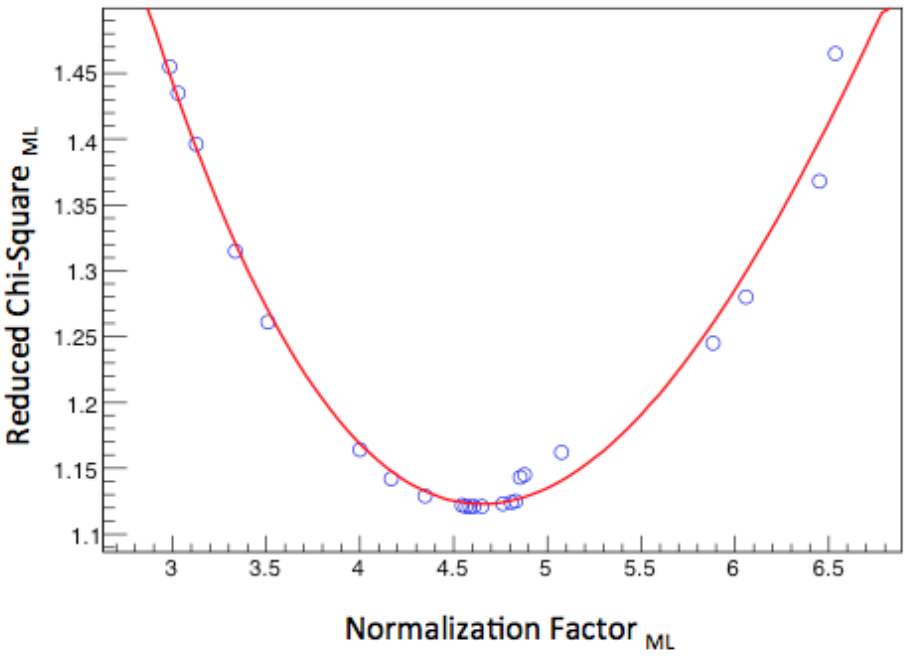

Figure 3.13: Maximum likelihood chi-squares minimization: Reduced chi-square values versus the normalization factor for each chi-square, obtained from the comparison of measured and calcuated angular distribution for Koning-Delaroche global proton optical potential. The red curve shows fitted polynomial of degree 3.

Normalization Factor	Chi-Square	Reduced Chi-Square
6.54	4.39	1.46
4.65	3.36	1.12
2.98	4.36	1.45

Table 3.2: Maximum likelihood chi-square values corresponding to each normalization factor obtained through maximum likelihood chi-square minimization

3.8.2 Uncertainty in Normalization Factor

In this section, various factors that contribute to the evaluation of an accurate normalization factor are discussed. In addition, a discussion on both minimization methods is made.

In an attempt to find the uncertainty for the normalization factor obtained by both the methods discussed above, $\chi 2_{min}+1$ i.e. within the 1σ limit is evaluated. Table 3.1 and 3.2 show the normalization factor corresponding to the minimum chi-square and reduced chi-square in first, second and third column, respectively, for both least squares chi-square minimization and maximum likelihood chi-square minimization method. In addition to this, one standard deviation for the minimum chi-square and corresponding normalization factor are also shown for each method. This gives rise to the statistical contribution in uncertainty of normalization factor, coming from the method of normalization.

To fit experimental data of low statistics is quite challenging. While fitting the data with χ^2 methods, systematic errors are incurred. When applied to low-statistics data, results that differ systematically from the true values are obtained. Stated briefly, χ^2 obtained by first method i.e. least-squares fitting yields a parameter with a deviation of -1 (Y. Jading and K. Riisager, 1996). This bias can be overcome by employing maximum-likelihood methods, and the Poisson likelihood chi-square analysis (S. Baker and R. D. Cousins, 1983). Therefore, from here on, the results from Maximum likelihood method is used for further analysis.

Based on the discussion above, the final normalization factor for the global proton optical model of Koning-Delaroche is concluded to be $4.65\ ^{+1.89}_{-1.67}$. Once the normalization

factor is obtained, the calculated cross section is scaled by the normalization factor. This gives an angular distribution of the differential cross section over complete angular range of 0°to 180°. This distribution is integrated to evaluate the total cross section as shown in section 3.9.

However, the uncertainty that might arise from calculating the theoretical angular distribution cannot be ignored as it will propagate in the uncertainty in normalization factor. In the interest of determining the uncertainty of the theoretical angular distribution, three more global proton potential parameter sets are used. These phenomenological optical model parameters were determined by fitting elastic-scattering angular distributions for various incident particles over an energy range that is consistent with the measurement energy used in this work (C. M. Perey, 1976). This compilation consists of a systematic analysis for proton potentials over large energy ranges and mass numbers. Significant contributions and variations in optical potentials have been provided by Menet et al. (J. J. Menet et al., 1971), Becchetti & Greenlees (F. D. Becchetti et al., 1969), and Perey (F. G. Perey, 1963) at different energy intervals and mass number ranges. Each global optical potential set is employed to calculate the complete theoretical differential cross section for $^{19}\mathrm{F}(\mathrm{p},\alpha)^{16}\mathrm{O}_{gs}$ transfer reaction over an angular range of 0°to 180°. FRESCO was used to calculate the theoretical distribution for each parameter set.

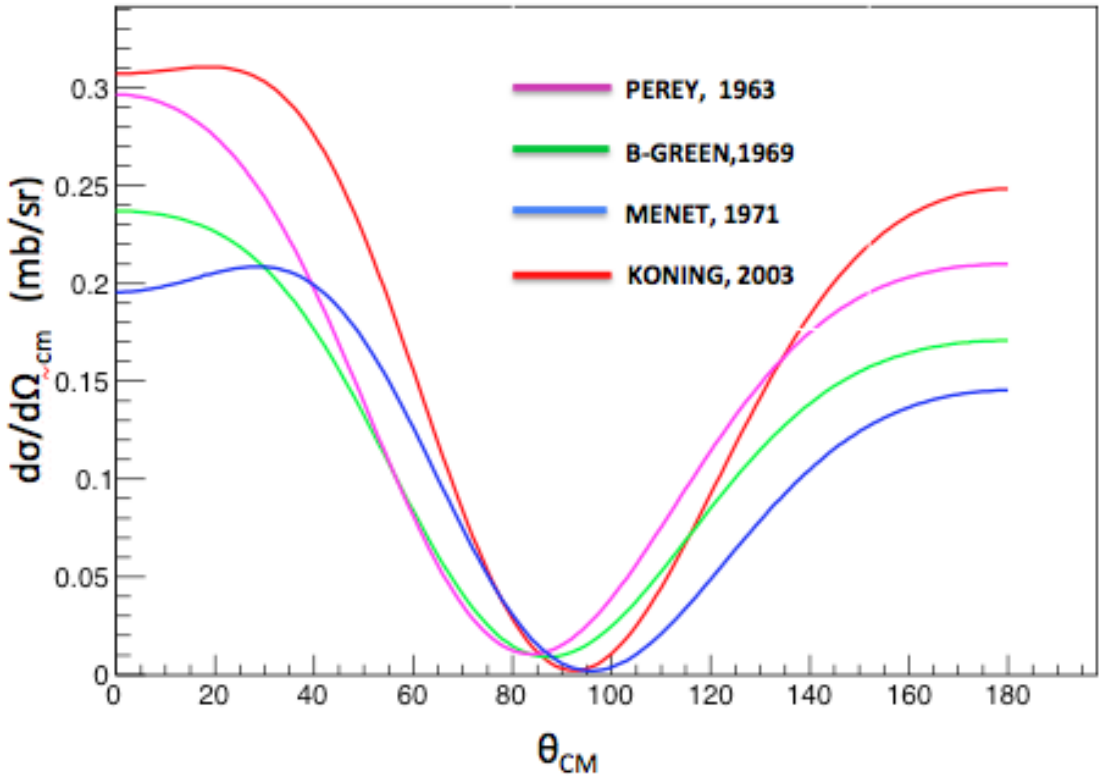

Figure 3.14: Calculated angular distribution for ^{19}F(p,α)^{16}O$_{gs}$, using parameters based on various theoretical formulations for global proton potentials

Figure 3.14 shows the calculated angular distribution for each of the global optical model set. In this work, none of the model has been considered superior than the other. Therefore, this variation in the calculation of angular distribution for the same reaction is an important contribution to evaluate uncertainty in the normalization factor.

In the next sections, Maximum likelihood chi-square minimization is used to scale

the calculated angular distribution from each global potential to the measured angular distribution that yields a normalization factor with an uncertainty for each global model.

3.8.3 Menet et al., 1971

The global proton potential parameters formulated by the work of Menet et al. was based on extensive analysis in energy region from 30 MeV to 60 MeV. They used extensive cross section data to help determine imaginary potential. Their parameter set was used to calculate the angular distribution using FRESCO. This calculated angular distribution is compared to the measured angular distribution using Maximum likelihood method. The results obtained are shown below in Fig. 3.15 and Table 3.3.

The final normalization factor as obtained through Maximum likelihood method is concluded to be $9.61\ ^{+4.47}_{-3.36}$.

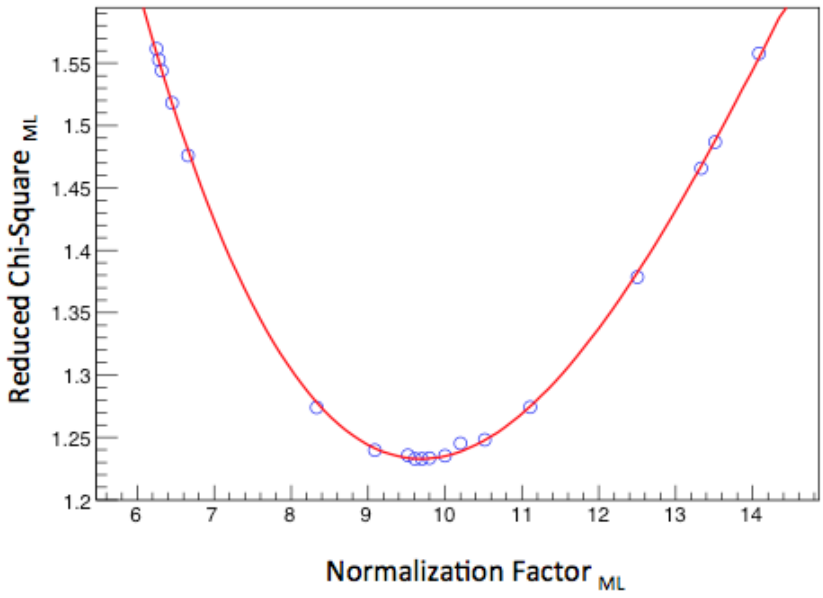

Figure 3.15: Using Maximum likelihood Method: Reduced chi-square values versus the normalization factor for each chi-square,obtained from the comparison of measured and calcuated angular distribution for Menet et al. (1971) global proton optical potential. The red curve shows fitted polynomial of degree 3.

Normalization Factor	Chi-Square	Reduced Chi-Square
14.08	4.67	1.55
9.61	3.69	1.23
6.25	4.68	1.56

Table 3.3: Maximum likelihood Chi-Square values for comparison of measured angular distribution to calculated angular distribution using Menet et al. (1971) global optical model

3.8.4 Becchetti-Greenless, 1969

The systematic analysis of Becchetti & Greenless fitted well a large number of elastic differential cross section for E < 50 MeV. The geometry parameters used in this formulation are very well adapted to give good fits at energy around and less than 20 MeV. Their parameter set was used to calculate the angular distribution using FRESCO. The calculated angular distribution is compared to the measured angular distribution using Maximum Likelihood method. The results obtained are shown in Fig. 3.16 and Table 3.4 below

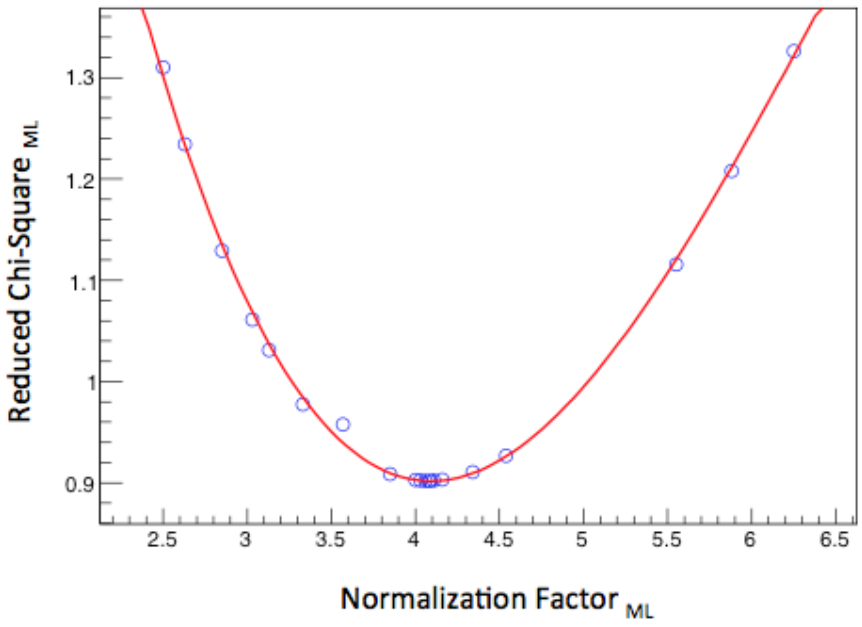

Figure 3.16: Using Maximum likelihood Method: Reduced chi-square values versus the normalization factor for each chi-square, obtained from the comparison of measured and calcuated angular distribution for Becchetti-Greenlees (1968) global proton optical potential. The red curve shows fitted polynomial of degree 3.

Normalization Factor	Chi-Square	Reduced Chi-Square
5.88	3.62	1.20
4.08	2.70	0.90
2.63	3.70	1.23

Table 3.4: Maximum likelihood chi-square values for comparison of measured angular distribution to calculated angular distribution using Becchetti-Greenlees (1968) global optical model

The final normalization factor as obtained through Maximum likelihood method is concluded to be $4.08\ ^{+1.80}_{-1.45}$.

3.8.5 Perey, 1963

The analysis of Perey is applicable below 25 MeV. Also, this potential does not have spin-orbit potential because of lack of data. Their parameter set was used to calculate the angular distribution using FRESCO. This calculated angular distribution is compared to the measured angular distribution using Maximum likelihood method. The results obtained are shown below in Fig. 3.17 and Table 3.5.

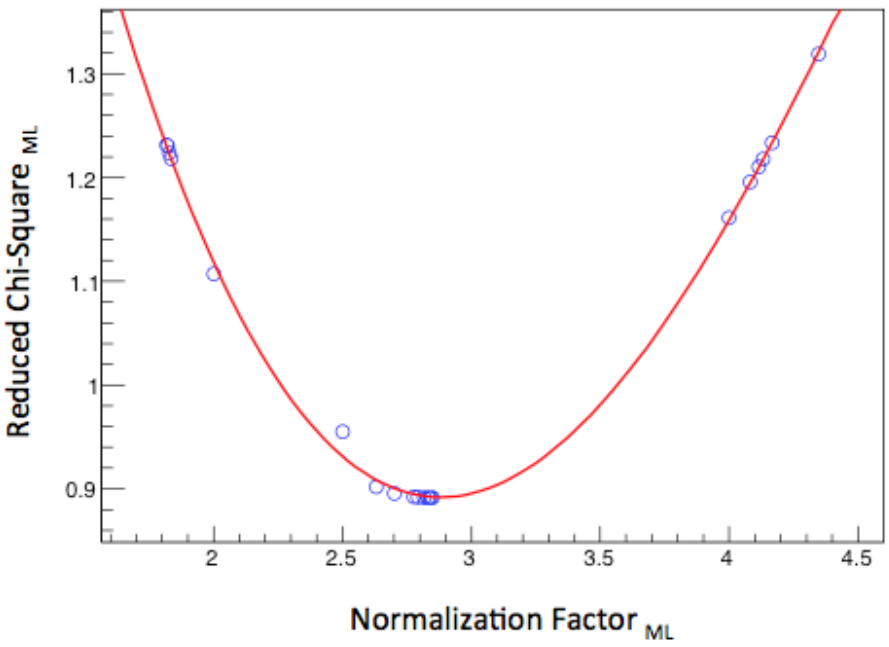

Figure 3.17: Using Maximum likelihood Method: Reduced chi-square values versus the normalization factor for each chi-square, obtained from the comparison of measured and calcuated angular distribution for Perey (1963) global proton optical potential. The red curve shows fitted polynomial of degree 3.

Normalization Factor	Chi-Square	Reduced Chi-Square
4.13	3.65	1.22
2.83	2.67	0.89
1.83	3.67	1.22

Table 3.5: Maximum likelihood chi-square values for comparison of measured angular distribution to calculated angular distribution using Perey (1963) global optical model

The final normalization factor as obtained through maximum likelihood method is concluded to be $2.83\ ^{+1.30}_{-1.00}$.

In summary, the final normalization factor with the uncertainty, as obtained by minimization of Maximum likelihood chi-square, for each global proton optical potential model is tabulated as shown below in Table 3.6.

Global Optical Model	Normalization Factor	Chi-Square	Reduced Chi-Square
Koning-Delaroche, 2003	$4.65\ ^{+1.89}_{-1.67}$	3.36	1.12
Menet et al., 1971	$9.61\ ^{+4.47}_{-3.36}$	3.69	1.23
Becchetti-Greenlees, 1969	$4.08\ ^{+1.80}_{-1.45}$	2.70	0.90
Perey, 1963	$2.83\ ^{+1.30}_{-1.00}$	2.67	0.89

Table 3.6: Summary of the results obtained by scaling the calculated angular distribution to the measured angular distribution corresponding to each global proton optical potential model (in column 1), Normalization Factor for each model (in column 2). Column 3 and column 4 show the respective chi-square and reduced chi-square for each value of the normalization factor

3.9 Total integrated cross section

The measured cross section covers only a small angular range in the center of mass. Outside the angular range explored in the present experiment, the angular distribution trend is taken to the best fit to experimental angular distribution. To obtain the total cross section $\sigma_{tot}(E)$ of ^{19}F(p,α)^{16}O$_{gs}$, the normalized angular distribution of each global optical model was integrated over 4π. The total cross section has been obtained by integrating the normalized angular distributions over the solid angle by using the expression

$$\sigma_{tot}(E) = \int \frac{d\sigma}{d\Omega} \times d\Omega$$

which can be rewritten as

$$\sigma_{tot}(E) = \int \frac{d\sigma}{d\Omega} \times 2\pi \times sin(\theta) \times d\theta$$

The uncertainty in total cross section is propagated from the uncertainty in the normalization factor.

Table 3.7 shows the summary of results for total cross section for ^{19}F(p,α)^{16}O$_{gs}$ as found by integrating the normalized angular distributions.

Global Optical Model	Total cross section (mb)
Koning-Delaroche, 2003	$7.65\ ^{+3.11}_{-2.75}$
Menet et al., 1971	$10.69\ ^{+4.97}_{-3.74}$
Becchetti-Greenlees, 1969	$4.76\ ^{+2.10}_{-1.70}$
Perey, 1963	$3.95\ ^{+1.80}_{-1.40}$

Table 3.7: Results for total cross section (in column 2) for each global proton optical potential model considered in the present work (column 1)

Chapter 4

Results and Discussions

4.1 Implications for astrophysics

Nuclear structure and nuclear dynamics play an important role in astrophysics. The occurrence or non-occurrence of a certain state at a given excitation energy can change the reaction rate by many orders of magnitude, and, consequently the abundance of the element involved may change. The reaction rates are calculated using the total cross sections σ_{tot}(E) of reactions, or related astrophysical S-factor $S(E)$. The total cross section is converted to astrophysical S-factor by using the following expression

$$\sigma_{tot}(E) = E^{-1} exp(-2\pi\eta) S(E) \tag{4.1.1}$$

The quantity η is called Sommerfeld parameter and is defined as

$$\eta = \frac{Z_1 Z_2 e^2}{h\nu}$$

and the quantity $exp(-2\pi\eta)$ is the Coulomb barrier penetration penetrability.

To obtain $S(E)$ from equation 4.1.1, the above equation can be rearranged as shown below

$$S(E) = \frac{\sigma(E) \times E}{exp(-2\pi\eta)} \tag{4.1.2}$$

or,

$$S(E) = E \times exp(2\pi\eta) \times \sigma_{tot}(E) \tag{4.1.3}$$

By substituting total cross section σ_{tot}(E) of ^{19}F(p,α)$^{16}O_{gs}$, as obtained in section 3.9, the astrophysical S-Factor of ^{19}F(p,α)$^{16}O_{gs}$ at an incident energy of E_{cm} = 2.35 MeV is calculated. Since each global optical model gives a different value of total cross section, the astrophysical S-factor corresponding to each total cross section is evaluated.

4.1.1 Uncertainty in Astrophysical S-Factor

The uncertainty attributed to the measured astrophysical S-factor is a combination of both statistical and systematic errors, arising from the uncertainty in E_{cm}, the uncertainty in $exp(2\pi\eta)$ due to the uncertainty in E_{cm} and the uncertainty in $\sigma_{tot}(E)$.

The energy E_{cm} = 2.35 MeV is evaluated by assuming the reaction point to be at half the target thickness. This corresponds to a definite interaction point whereas in reality the interaction occurs randomly within the target thickness. To account for that, a spread in the reaction energy within the target is evaluated. This results in a range in the E_{cm} as from 2.27 MeV to 2.43 MeV, giving a spread of 0.08 MeV. This spread is used as a contribution to the overall uncertainty in $S(E)$. This uncertainty is propagated in the evaluation of uncertainty in $exp(2\pi\eta)$. The uncertainty in total cross section is listed in Table 3.7, that was used to evaluate $S(E)$. The dominant contribution to the uncertainty is coming from the uncertainty in total cross section.

The total uncertainty is evaluated by propagating the individual uncertainties from each contribution and adding those together in quadrature as shown below

$$\Delta_{S(E)} =$$

$$\sqrt{(exp(2\pi\eta) \times \sigma_{tot}(E))^2 \times \sigma^2_{Ecm} + (E_{cm} \times \sigma_{tot}(E))^2 \times \sigma^2_{exp(2\pi\eta)} + (E_{cm} \times exp(2\pi\eta)^2) \times \sigma^2_{tot}(E)} \tag{4.1.4}$$

Table 4.1 shows the upper and lower limits of 1σ contribution of individual uncertainties added up in quadrature in equation 4.1.4. As seen in the table, the majority of the contribution to the total uncertainty comes from the individual uncertainty in total cross section, approximated to be about $\sim$ 90% to 95 %. This is followed by the individual uncertainty in $exp(2\pi\eta)$, and then a minor contribution $\sim$ 5% to 10 % from the uncertainty in the E_{cm}.

Global Optical Model	ΔE_{cm} (1σ)	$\Delta_{exp(2\pi\eta)}$ (1σ)	$\Delta_{\sigma tot}$ (1σ)
Koning-Delaroche, 2003	$^{+0.179}_{-0.179}$	$^{+0.468}_{-0.560}$	$^{+2.143}_{-1.895}$
Menet et al., 1971	$^{+0.250}_{-0.250}$	$^{+0.654}_{-0.783}$	$^{+3.424}_{-2.577}$
Becchetti-Greenlees, 1969	$^{+0.111}_{-0.111}$	$^{+0.291}_{-0.348}$	$^{+1.447}_{-1.227}$
Perey, 1963	$^{+0.093}_{-0.093}$	$^{+0.242}_{-0.289}$	$^{+1.240}_{-0.965}$

Table 4.1: Individual uncertainty contribution within 1σ interval of each factor carrying uncertainty used in the evaluation of the total uncertainty in $S(E)$

Table 4.2 shows the final astrophysical S factor $S(E)$, evaluated corresponding to each total cross section coming from different global optical models. The total uncertainty within the 1σ interval, as propagated from each individual contribution is shown.

Global Optical Model	Astrophysical S-Factor (MeV-barn)
Koning-Delaroche, 2003	$5.28\ ^{+2.20}_{-1.98}$
Menet et al., 1971	$7.37\ ^{+3.50}_{-2.70}$
Becchetti-Greenlees, 1969	$3.29\ ^{+1.48}_{-1.23}$
Perey, 1963	$2.72\ ^{+1.27}_{-1.01}$

Table 4.2: Summary of the astrophysical S-factor for measurement of ^{19}F(p,α)$^{16}O_{gs}$ at E_{cm} = 2.35 MeV performed in this work

A nuclear reaction occurs when two nuclei a and A are brought close enough together such that they are closer than the sum of their radii. When the incident particle interacts with only one or a few nucleons in the target, direct reaction mechanism is dominant leading to final products b and B as a+A -> b+B. On the other hand, a resonant reaction occurs when two nuclei a and A fuse together into an excited state of a compound nucleus C, then decay into the product particles b and B as a+A -> C -> b+B. In this case, the center of mass energy is well matched with the resonance energy, and the properties of the interacting nuclei are such that the angular momentum selection rules corresponding to the compound nuclear state are satisfied. Hence, the the cross section for reaction is greatly enhanced around this energy, causing a large increase in the astrophysical S-factor. Depending on the mechanism through which the reaction takes place, the angular distribution of the fragments

may vary significantly, showing distinguishing features in the spectrum. This becomes a little difficult if the incident energy is very low since the resonant and direct contributions may overlap.

The reaction rate, therefore, is mainly divided into two major contributions - direct capture and resonant capture. For a resonant capture, ^{19}F(p,α)^{16}O proceeds via a compound nucleus state as

$$^{19}F + p -> ^{20} Ne -> \alpha + ^{16} O$$

Here, ^{20}Ne is the compound nucleus formed, before the state decays into an alpha particle and a heavier residual nucleus ^{16}O. The emission probabilities are defined through the partial energy widths, Γ_x as the particle width. As mentioned in chapter one, equation 1.2.13, the knowledge of resonance energies is of critical importance as the reaction rate varies exponentially with the resonance energy.

The astrophysical S-factor in Fig 1.6. shows the presence of many resonance peaks over a wide range of center of mass energies. In the energy range measured in this work, E_{cm} = 2.27-2.43 MeV, the previously reported results show different behaviour in the variation of $S(E)$ with energy. There are many sharp peaks observed in the astrophysical S-factor towards the lower energy range of this measurement. This behaviour is attributed to the presence of resonant states corresponding to known states in ^{20}Ne. This shows that the compound nucleus mechanism is also contributing to the reaction mechanism along with

the direct reaction mechanism for ^{19}F(p,α)^{16}O$_{gs}$. The measured angular distribution is therefore a sum of resonant and direct capture processes. The differential cross sections for the two processes can be quite different in both magnitude and shape. To determine accurately the relative resonant and direct contributions involves a detailed study of the excitation function which is beyond the scope of this thesis work.

Therefore, in this work we have assumed the shape of angular distribution of resonant and direct capture to be similar within the measured energy range. With this assumption, we have therefore normalized only the calculated differential cross section from the direct reaction i.e. from DWBA, to the data. Since this normalization does not take into account separately the resonant capture, the normalization factor deduced is not the same as the spectroscopic factor that involves the structure of the nuclei involved. The total cross section and hence the astrophysical S factor $S(E)$ is then extracted from the angle integrated value of this normalized differential cross section from DWBA. Therefore, the extracted $S(E)$ contains the uncertainty of the missing angular distribution shape of the resonant capture. The extracted $S(E)$ represents therefore, only a lower limit where the total angular distribution is similar to that of the direct reaction.

4.2 Comparison to previous measurements in relevant energy range

As discussed in the introduction, two different trends of the variation of astrophysical S-factor in the interested range of energy is observed. As mentioned in chapter one, previous measurements by R. L. Clarke and E. B. Paul (R. L. Clarke & E. B. Paul, 1957) and

Cuzzocrea et al. (P. Cuzzocrea et al., 1980) have reported the astrophysical S-factor for the reaction of interest ^{19}F(p,α)$^{16}O_{gs}$ to be 19.70 MeV-barn and 9.53 MeV-barn respectively. However, these two measurements differ from each other significantly. A distinguishing feature from the present work is that, both the previous measurements were done in direct kinematics whereas the measurement in this work was performed in inverse kinematics.

While making a comparison to previous measurements, the first step is to look in the literature for information on the $S(E)$ relevant to the energy of our experiment. The earliest source of information comes from an experiment performed by R. L. Clarke and E. B. Paul, in 1957. Their experiment was an extension of the earlier work of Rubin (S. Rubin, 1947) extended to higher energies. The reaction of interest ^{19}F(p,α)$^{16}O_{gs}$ has been studied from an energy of 1.3 MeV to 2.7 MeV which includes the reaction energy of this present measurement. In their measurement, protons from an electrostatic accelerator hit on a CaF_2 target backed up by copper disks. Their detection system set up to measure the angular distribution consisted of a magnetic spectrometer along with a proportional counter. The alpha particles resulting from the reaction were analyzed by means of a magnetic spectrometer which separated alpha particles from the scattered protons.

The alpha particles were detected in a proportional counter. They stated that the proportional counter was employed to distinguish readily the ground state group of alpha particles from the lower energy alpha particles to make sure that only the ground state group was counted. The range of angles covered by their detection system was between 30°to 150°. They analyzed their data in terms of Legendre polynomials up to order four and the fitting

was done by the least squares method with all the points weighted equally. Figure 4.1 shows the measured angular distribution versus the cosine of the center of mass angle, observed by R. L. Clarke and E. B. Paul. The chief uncertainties present in their measurement were in the absolute calibration of the beam current integrator since they used beam current as a measure of their incident beam.

In 1980, P. Cuzzocrea et al., measured the $^{19}F(p,\alpha)^{16}O_{gs}$ reaction in an energy range of 0.7 to 2.68 MeV at the Laboratori Nazionali di Legnaro (Padova). Their reaction target consisted of CaF_2/BaF_2 evaporated onto thin carbon backing. The angular range covered by their detectors made a measurement from 30°to 160°. They fitted their angular distributions by Legendre Polynomial expansion as shown in Fig. 4.2. Their uncertainty primarily arose from the results of least squares fit.

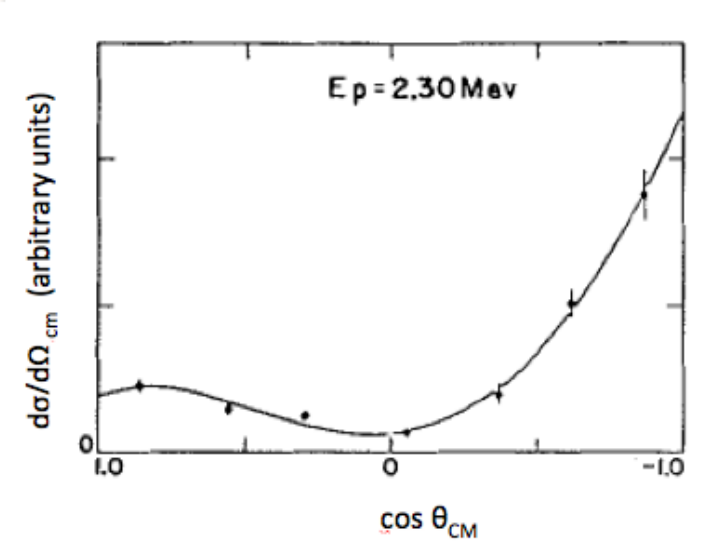

Figure 4.1: Observed angular distribution versus θ, with solid curves showing Legendre polynomial fitting to the data, R. L. Clarke and E. B. Paul. (Figure adapted from R. L. Clarke & E. B. Paul, 1957)

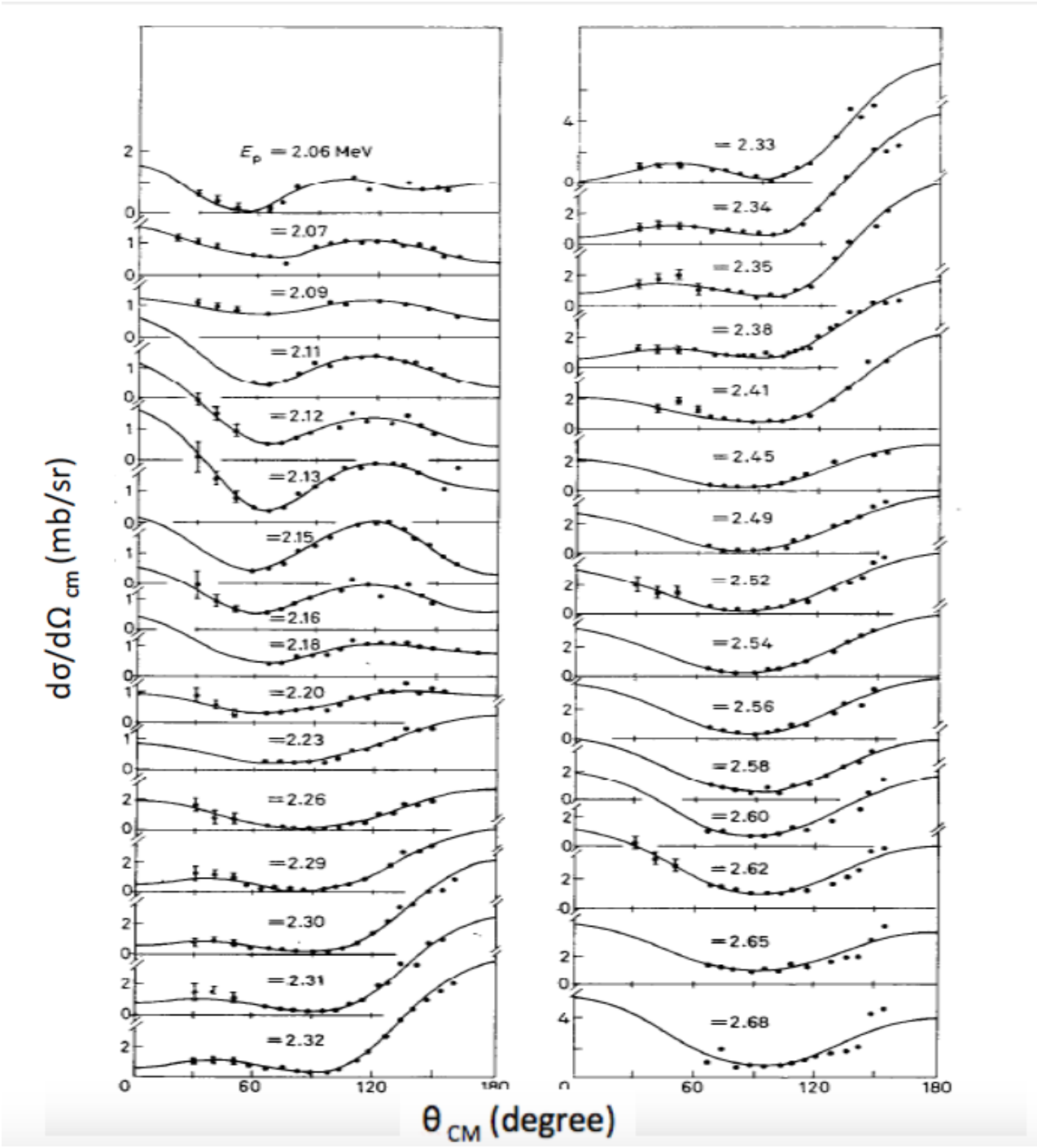

Figure 4.2: Observed angular distribution versus θ, with solid curves showing Legendre polynomial fitting to the data, P. Cuzzocrea et al. (Figure adapted from P. Cuzzocrea et al., 1980)

4.2.1 Average $S(E)_{published}$

To compare the results obtained in this work to previous published measurements, an average of the astrophysical S-factor over the energy range in E_{cm} considered in this work was evaluated. WebPlotDigitizer (Ankit Rohatgi, automeris.io), a web based tool to extract data from plots, was used to get the data points from published results of $S(E)$ vs E_{cm} of Clarke and Paul, 1957 and P. Cuzzocrea et al., 1980.

The average of $S(E)$ over the relevant E_{cm} was found by using the following expression

$$\int_{E_1}^{E_2} S(E)dE \tag{4.2.1}$$

i.e. an integral of S(E) over the energy interval from E_1 to E_2

from which the average can be found as,

$$S(E)^{avg}_{published} = \frac{1}{E_2 - E_1} \int_{E_1}^{E_2} S(E)dE \tag{4.2.2}$$

E_1 and E_2 here refer to the lower and upper energy limit respectively in the range of E_{cm} used in this work. Figure 4.3 and 4.4 show the published data in terms of $S(E)$ vs E_{cm}. The data marked in red vertical lines corresponds to the range in center of mass energy relevant for this measurement, used here to find the average of the astrophysical S factor

over the energy interval.

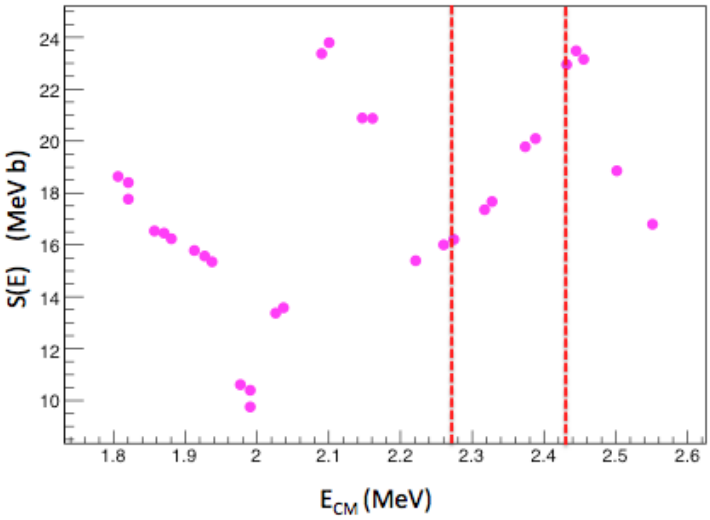

Figure 4.3: Extracted data points from R. L. Clarke & E. B. Paul 1957, using WebPlotDigitizer. The red dashed vertical lines show the range of E_{cm} considered in this work

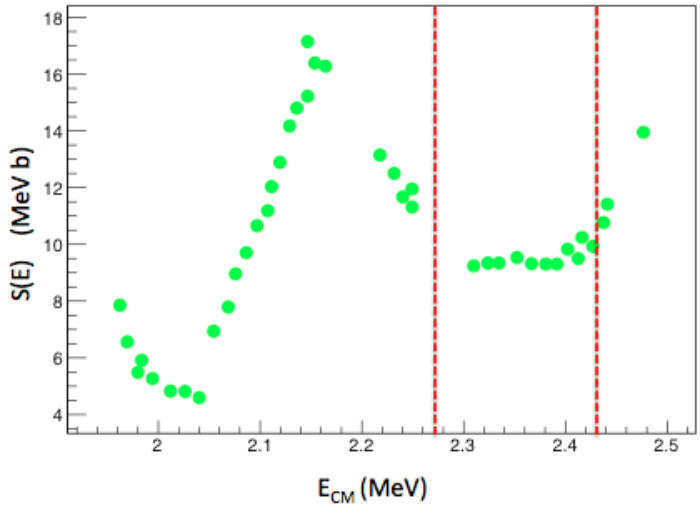

Figure 4.4: Extracted data points from P. Cuzzocrea et al., 1980, using WebPlotDigitizer. The red dashed vertical lines show the range of E_{cm} considered in this work

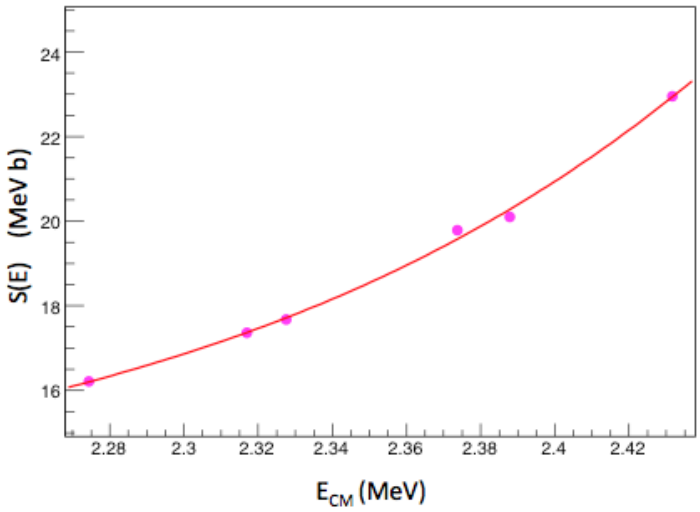

Figure 4.5: Zoomed in extracted data points from R. L. Clarke & E. B. Paul 1957, using WebPlotDigitizer, in the range of E_{cm} considered in this work. The red curve shows fitted polynomial of degree 3.

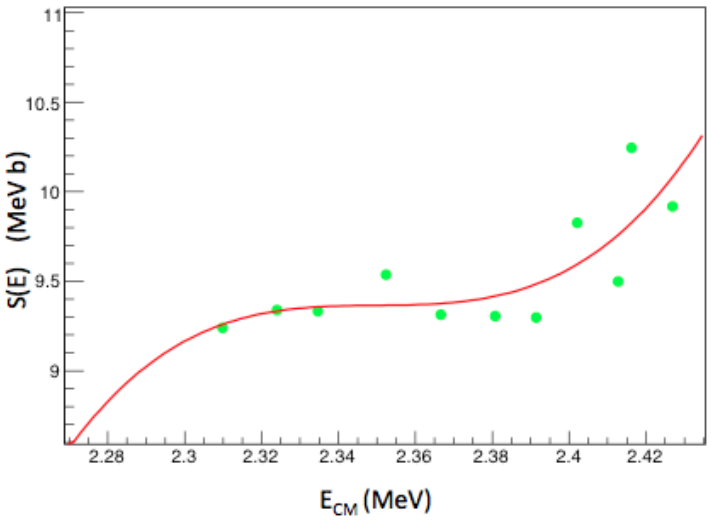

Figure 4.6: Zoomed in extracted data points from P. Cuzzocrea et al., 1980, using WebPlotDigitizer, in the range of E_{cm} considered in this work. The red curve shows fitted polynomial of degree 3.

A polynomial of degree 3 is used to fit the continuous function curve for $S(E)$ as shown in Fig. 4.5 and Fig. 4.6. By integrating the polynomial function over the range E_1 and E_2, $S(E)^{avg}_{published}$ was evaluated as tabulated below in Table 4.3.

Reference	Astrophysical S-factor S(E) (MeV-barn)
Clarke-Paul, 1957	18.95
Cuzzocrea et al., 1980	9.95

Table 4.3: Average $S(E)_{published}$

4.3 Results & Conclusions

The astrophysical S-factor results evaluated in this work, as listed in Table 4.2, were combined together to find the final result. Since there are four individual values of the astrophysical S-factor, corresponding to four different global optical models for theoretical calculations of ^{19}F(p,α)^{16}O$_{gs}$, the final value of the S-factor has been found by combining the reported measurements. There are two ways in which this can be achieved.

An average value of the set of astrophysical factors $S(E)$ was calculated by combining the individual measurements obtained from four independent analysis. Based on this technique, we report the astrophysical S-factor for ^{19}F(p,α)^{16}O$_{gs}$ to be

$$S(E) = 4.66^{+1.45}_{-0.95} MeV - barn$$

The uncertainty, as reported above, has been found using the expression derived for an average of a set of measurements, as shown below,

$$\sigma^2_{S(E)} = \sum_{i=1}^{4} \frac{\partial S(E)_i}{\partial E} \sigma^2_{S(E)_i}$$

which can be written as

$$\sigma^2_{S(E)} = \frac{1}{4}\sqrt{\sigma^2_{S(E)1} + \sigma^2_{S(E)2} + \sigma^2_{S(E)3} + \sigma^2_{S(E)4}}$$

This average has been found taking the mean value from four different analysis and uncertainty as the overlapping region from four independent analysis.

In another method, assuming that each measurement of S(E) is not independent of each other, the absolute uncertainty has been found by taking the full range of individual uncertainties allowed by the four different analysis. This uncertainty is much larger as compared to the previous uncertainty, and comes out to be

$$S(E) = 4.66^{+2.35}_{-2.35} MeV - barn$$

As compared to the $S(E)^{avg}_{published}$ deduced from previous data reported in the literature, the $S(E)$ evaluated in the present work, within the 1σ confidence interval, lies closer to the result reported by P. Cuzzocrea et al. Overall, the average value of $S(E)$ measured in this work is smaller than the $S(E)^{avg}_{published}$ results from Clarke and Paul (R. L. Clarke & E. B. Paul, 1957) and P. Cuzzocrea et al. (P. Cuzzocrea et al., 1980).

As the use of DWBA differential cross section represents only a lower limit of the $S(E)$, further analysis is required including the resonant reaction mechanism for establishing the relevance of low energy $S(E)$ for AGB stars. In addition, since this measurement is made

at an energy much higher than the Gamow Peak for AGB stars (E_{cm} = 24 keV - 112 keV), an extrapolation of the measured astrophysical S-factor at the energy down to a few tens of a keV is important to draw a firm conclusion. A standard solution of extrapolating to lower energies is to measure the $S(E)$ over a over a wide range of energies and to the lowest energies possible in experimental measurements. From there, the data is extrapolated downward to the meaningful astrophysical energy. The extracted astrophysical S-factor in this work provides a guidance on comparison between different existing data sets. In order to accurately determine the capture cross section, and hence $S(E)$ at the lowest energies, a more detailed study over a wide energy range, in particular down to the lowest center of mass energies will be needed. In conclusion, this measurement favours the lower $S(E)$ from previous measurements at E_{cm} = 2.35 MeV, with a condition that the possibility of resonant reaction mechanism has not been taken into account in this analysis.

This work hints at a lower value of $S(E)$ at the higher energies that can potentially constrain theoretical estimates of the astrophysical S-factor for a better prediction at the lowest energies where the direct measurements are challenging. A lower value of $S(E)$ suggests a lower reaction rate of ^{19}F(p,α)$^{16}O_{gs}$, leading to many important astrophysical implications. Since this reaction channel removes ^{19}F from nucleosynthesis scenario, it may have an effect on overall fluorine abundance. A lower cross section of this destruction channel implies a less efficient fluorine destruction channel. How such a reduction of the ^{19}F(p,α)$^{16}O_{gs}$ cross section would fit in the framework of the current nucleosynthesis models during the AGB phase is worthwhile to look into. As mentioned in the introduction chapter,

the nucleosynthesis models for low metallicity AGB stars overestimate the fluorine abundances. Since this reaction channel significantly modifies the fluorine abundances, lower cross section for this destruction channel, as found through this work, makes the theoretical model predictions more robust.

This could also possibly indicate towards a revision of major fluorine production channels in AGB stars at lowest temperatures, relevant only for astrophysics, $\sim T_9 = 0.007$ - 0.15 and E_{cm} = 19 keV - 146 keV to solve the discrepancy between theoretical predictions and observations, as these stars being also established sources of Galactic fluorine. The above temperature range has been found by using the following gamow energy window calculator (C. Iliadis, Pg - 176, 2010)

$$E_0 = 0.1220(Z_0^2 Z_1^2 \mu T_9^2)^{\frac{1}{3}} \ \ MeV$$

where, E_0 is the maximum of the Gamow peak in MeV, Z_0 and Z_1 is the atomic number of projectile and target respectively, μ is the reduced mass of projectile and target, and T_9 is the temperature in GK.

In the case of $^{18}O(p,\gamma)^{19}F$, the presence of several low energy states influence the determination of cross section. The major contribution due to E_{cm} = 150 keV resonance is the largest contributor to the reaction rate. However, the uncertainty in the reaction rate is 10 %, as adopted in Iliadis et al., 2010. For $^{15}N(\alpha,\gamma)^{19}F$, the rate is completely dominated by the contributions from several low lying states in the energy window of E_{cm}

= 0.6 MeV to 2.7 MeV. The uncertainty in this reaction rate is $\sim$ 15% (S. Cristallo, 2014). Therefore, an insight into these fluorine production channels could also show an effect on the understanding the abundance of fluorine.

Since the absolute cross section of the ^{19}F(p,α)^{16}O reaction is of importance in hydrogen burning in stars, this result has a potential to have an effect on the rates at which the CNO cycle is broken in explosive astrophysical scenarios. This branch of the reaction dominates the reaction rate over a wide temperature range and gives the largest contribution to the reaction rate of ^{19}F(p,α)^{16}O reaction for temperatures below $T_9 \sim 0.1$ (K. Spyrou, 2000). If the hydrogen burning of ^{19}F proceeds predominantly through ^{19}F(p,α)^{16}O reaction, the CNO catalytic material will remain in the cycle. However, if the competing reaction ^{19}F(p,γ)^{20}Ne is stronger, then the CNO catalytic material will be lost through this reaction and the various CNO cycles would eventually cease to be an energy source in the hydrogen burning. Therefore, an implication of the weaker ^{19}F(p,α)^{16}O channel indicates towards the breakout from the CNO cycle leading to leaking of the catalytic material that can be lost in the CNO cycle and becomes available for the NeNa cycle i.e. an early onset of NeNa cycle. This breakout from the cycle can also lead to a diversion of nuclear flow to heavier nuclei. In addition, ^{19}F(p,α)$^{16}O_{gs}$ also gives an insight into the mixing processes taking place inside AGB stars as the highest values of the observed ^{19}F enhancements in the stellar atmosphere are not matched by standard AGB models and require additional mixing.

A simultaneous production of fluorine and s-process elements is expected during the AGB phase, since, for both species, neutrons coming from the ^{13}C(α,n)^{16}O reaction,

which is active in the He-shell during the thermal pusle and interpulse phase, are required. A weaker fluorine destruction channel implies towards more nucleons available for synthesis of heavier elements via s-process and rp-process.

Future work still needs to be done trying to constrain this reaction better with more statistics to understand the destruction of fluorine in the universe. This result also suggests significant contribution of other fluorine destruction channels, e.g.

^{19}F(p,γ)^{20}Ne and ^{19}F(α,p)^{22}Ne

which might have a potential effect on solving the discrepancy between theoretical calculations and observations. A previous measurement of ^{19}F(p,γ)^{20}Ne at E_{cm} = 200 - 700 keV (A. Couture et al., 2008), corresponding to temperatures below $T_9 \sim 0.1$ suggests the need of measurement at higher energies to constrain the reaction cross section better. They mention the role of higher energy measurements of ^{19}F(p,α)^{16}O that will conclusively determine the (p,α) to (p,γ) branching at the end of the CNO cycle. The direct measurement of ^{19}F(p,α)^{16}O at E_{cm} = 2.35 MeV in this work serves as an attempt to reduce the uncertainties in the cross section of this reaction. This could also potentially help to reduce the nuclear origin of disagreements that occur while extrapolating down to lower energies. However, a complete information concerning the total cross section is the necessary requirement for the determination of the complete understanding of the reaction rate vs temperature.

To sum up, more statistics are required to make a firm conclusion on ^{19}F(p,α)$^{16}O_{gs}$ reaction. To extend further, investigations on other channels as preferred mechanism of de-

struction of fluorine in AGB stars should be considered. It would be reasonable to anticipate different stellar environments, each contributing, in terms of production and destruction of ^{19}F, to the total abundance observed.

Bibliography

1. A. Boeltzig, C. G. Bruno, F. Cavanna, S. Cristallo, T. Davinson, R. Depalo, R. J. deBoer, A. Di Leva, F. Ferraro, G. Imbriani, P. Marigo, F. Terrasi, and M. Wiescher *"Shell and explosive hydrogen burning"*, Eur. Phys. J. A, 52, 2016.

2. A. Couture, M. Beard, M. Couder, J. Gorres, L. L. Lamm, P. J. LeBlanc, H. Y. Lee, S. O'Brien, A. Palumbo, E. Stech, E. Strandberg, W. Tan, E. Uberseder, C. Ugalde, and M. Wiescher *"Measurement of the* $^{19}F(p,\gamma)^{20}Ne$ *reaction and interference terms from* E_{cm} *= 200 -700 keV"*, Physical Review C 77, 015802, 2008

3. A. C. Mueller and B. M. Sherrill *"Nuclei at the Limits of Particle Stability"*, Ann.Rev.Nucl.Part.Sci. 43, 529, 1993.

4. A. E. Lovell and F. M. Nunes *"Systematic uncertainties in direct reaction theories"*, Journal of Physics, Nuclear and Particle Physics 42, 034014, 2015.

5. A. E. Lovell, F. M. Nunes, J. Sarich, and S. M. Wild *"Uncertainty Quantification for Optical Model Parameters"*,

6. A. Isoya, H. Ohmura, and T. Momota *"The angular distributions of the long-range alpha particles from the reaction* $^{19}F(p,\alpha)^{16}O$", Nucl. Phys. 7, 116, 1959

7. A. J. Koning and J. P. Delaroche *"Local and global nucleon optical models from 1 keV to 200 MeV*", Nuclear Physics A, 713, 231-310, 2003

8. A. Jorissen, V. V. Smith, and D. L. Lambert *"Fluorine in red giant stars:evidence for nucleosynthesis* ", Astronomy & Astrophysics, 261, 164-187, 1992.

9. A. S. Chester *"Recoil Distance Method Lifetime Measurements of the 2+ Excited States in Kr-84 and Sr-94*", PhD Thesis, Simon Fraser University, Burnaby, B. C., 2013.

10. A. R. Choudhury *"Astrophysics for Physicists*", U. of Chicago P., 2010.

11. C. Abia, A. Recio-Blanco, P. De Laverny, S. Cristallo, I. Dominguez, and O. Straniero *"Fluorine in Asymptotic Giant Branch Carbon stars Revisited* ", The Astrophysical Journal, 694:971-977, A88, 2009.

12. C. Abia, K. Cunha, S. Cristallo, P. de Laverny, I. Dominguez, K. Eriksson, L. Gialanella, K. Hinkle, G. Imbriani, A. Recio-Blanco, V. V. Smith, O . Straniero, and R. Wahlin *"Fluorine Abundances in Galactic Asymptotic Giant Branch Stars*", The Astrophysical Journal Letters, 715:L94-L98, 2010

13. C. Abia, K. Cunha, S. Cristallo, and P. de Laverny *"The origin of fluorine : abundance in AGB carbon stars revisited*", Astronomy & Astrophysics 581, A88, 2015.

14. C. Iliadis (2010), *"Nuclear Physics of Stars"*, Wiley-VCH, Weinheim, 2010.

15. C. M. Perey and F. G. Perey, *"Compilation of Phenomenological Optical-Model Parameters"*, Atomic Data and Nuclear Data Tables, 17 1-101, 1976.

16. C. Rolfs and W. S. Rodney *"Cauldrons in the Cosmos"*, U. of Chicago P., Chicago, 561 pp., 1988.

17. D. Dell'Aquila and I. Lombardo *"An overview of the $^{19}F(p,\alpha)^{16}O$ reaction with direct methods"*, 8th European Summer School on Experimental Nuclear Physics, 703, 012015, 2016

18. D. J. Morrissey and B. M. Sherrill *"In-Flight Separation of Projectile Fragments"*, Lect. Notes Phys. 651, 113-135, 2004.

19. D. Montanni et al. *"Stella Experiment: A letter of intent for Andromede"*, 2016

20. D. W. Bardayan, *"Transfer reactions in Nuclear Astrophysics"*, J.Phys. G:Nucl. Part. Phys. 43, 2016.

21. F. D. Becchetti and G. W. Greenlees, *"Nucleon-Nucleus Optical-Model Parameters, $A>40$, $E<50$ MeV"*, Phy. Rev. 182, 1190, 1969.

22. F. G. Perey *"Optical-Model Analysis of Proton Elastic Scattering in the Range of 9 to 22 MeV"*, Phy. Rev. 131, 745, 1963.

23. G. Breuer *"$^{19}F(p,\alpha)^{16}O$ with direct methods"*, Z. Phys. 154, 339, 1959.

24. G. Breuer and L. Jahnke *"$^{19}F(p,\alpha)^{16}O$ with direct methods"*, Z. Naturf. 19a, 471, 1964.

25. G. C. Ball, G. Hackman and R. Krucken *"The TRIUMF-ISAC facility: two decades of discovery with rare isotope beams"*, J. Phys. G. 38, 024003, 2011.

26. G. F. Knoll, *"Radiation Detection and Measurement"*, John Wiley & Sons Inc., Hoboken, NJ, 4th edition, 2010.

27. G. R. Satchler (1983) *"Direct Nuclear Reactions"*, Oxford University Press

28. G. Sheffer, 2013 (private communication)

29. H. A. Bethe & C.L. Critchfield, *"The formation of Deuterons by Proton Combination"*, Phys. Rev. 54, 248, 1938.

30. H. Guo, Xinwu Su, H. Liang, Y. Xu, Y. Han, and Q. Shen *"Global phenomenological and microscopic optical potentials for alpha"*, Eur. Phys. J. 146, 12011, 2017.

31. H. Herndl, H. Abele, G. Staudt, B. Bach, K. Grun, H. Scsribany, H. Oberhummer and G. Raimann *"Direct Reaction Analysis of $^{19}F(p,\alpha)^{16}O$ below the Coulomb Barrier"*, Phys. Rev. C44, R952, 1991.

32. HE Jianjun, XU Shiwei, MA Shaobo, HU Jun, ZHANG Liyong, FU Changbo, ZHNAG Ningtao, LIAN Gang, SU Jun, LI Yunju, YAN Shengquan, SHEN Yangping, HOU Suqing, JIA Baolu, ZHANG Tao, ZHANG Xiaopeng, GUO Bing, KUBONO Shigeru, and LIU Weiping *"A proposed direct measurement of cross section at Gamow Window for key reaction*

$^{19}F(p,\alpha)^{16}O$ *in Asymptotic Giant Branch Stars with a planned accelerator in CJPL*“, Science China Physics, Vol. 58, No. 3, 5797, 2016.

33. H. Jonsson, N. Ryde, E. Spitoni, F. Matteucci, K. Cunha, V. Smith, K. Hinkle, and M. Schultheis *“Fluorine in the Solar Neighbourhood*”, The Astrophysical Journal, 835:50, 2017.

34. I. Iben *“Thermal Pulses: p-capture, alpha-capture, s-process nucleosynthesis; and convective mixing in a star of intemediate masses*“, The Astrophysical Journal, Vol. 196, 525-547, 1975.

35. I. Iben *“Neon-22 as a neutron source, light elements as modulators, and s-process nucleosynthesis in a thermally pulsing star*”, The Astrophysical Journal, Vol. 196, 549-558, 1975.

36. I. Iben *“Further adventures of a thermally pulsating star*“, The Astrophysical Journal, Vol. 208, 165-176, 1976.

37. I. J. Thompson *“Coupled Reaction Channels Calculations in Nuclear Physics*”, Computer Physics Reports 7, 167-212 , 1988

38. I. Lombardo, D. Dell’ Aquila, L. Campajola, E. Rosato, G. Spadaccini, and M. Vigilante *“The $^{19}F(p,\alpha)^{16}O$ Reaction at Low Bombarding Energy*“, Bulletin of the Russian Academy of Sciences (Physics), Vol. 78, No. 11, pp. 1093-1096, 2014.

39. I. Lombardo, D. Dell’Acquila, L. Campajola, E. Rosato, G. Spadaccini, M. Vigilante *“The $^{19}F(p,\alpha)^{16}O$ reaction at low bombarding energy*”, Bull. Rus. Acad. Sci. Phys. 78, 1093,

2014.

40. I. Lombardo, L. Campajola, D Dell'Aquila, M La Commara, E. Rosato, G. Spadaccini, and M. Vigilante *"Study of Nuclear Structure of 13C and 20Ne by Low Energy Nuclear Reactions*", J. Phys. Conf. Ser. 569, 012068, 2014.

41. I. Lombardo, D Dell'Aquila, A. Di Leva, I. Indelicato, M. La Cognata, M. La Commara, A. Ordine, V. Rigato, M. Romoli, E. Rosato, G. Spadaccini, C. Spitaleri, A. Tumino, and M. Vigilante *"Towards a reassessment of the $^{19}F(p,\alpha)^{16}O$ reaction rate at astrophysical temperature*", Phys. Lett. B 748, 178-182, 2015.

42. I. Indelicato, M. La Cognata, C. Spitaleri, V. Burjan, S. Cherubini, M. Gulino, S. Hayakawa, Z. Hons, V. Kroha, L. Lamia, M. Mazzacco, J. Mrazek, R. G. Pizzone, S. Romano, E. Strano, and A. Tumino *"New Improved Indirect Measurement of the $^{19}F(p,\alpha)^{16}O$ Reaction at Energies of Astrophysical Relevance*", The Astrophysical Journal, 845:19, 13pp, 2017.

43. Jian-Jun He, Ivano Lombardo, Daniele Dell' Acquila, Yi Xu, Li-Yong Zhang, Wei-Ping Liu *"Thermonuclear $^{19}F(p,\alpha)^{16}O$ reaction rate*", Chinese Physics C, 2017.

44. J. J. H. Menet et al., *"Total-Reaction-Cross-Section Measuerements for 30-60 MeV Protons and Imaginary Optical Potential*", Phys. Rev. C4, 1114, 1971.

45. J. M. D'Auria, *"A review of radioactive beam facilities in the world*", Nuclear Instruments and Methods in Physics Research Section B: Beam Interactions with Materials and Atoms,

vol. 99, no. 1-4, pp. 330-334, 1995.

46. K. S. Krane (1988) *"Introductory Nuclear Physics"*, John Wiley & Sons

47. K. Spyrou, C. Chronidou, S. Harissopulos, S. Kossionides, T. Paradelis, *"Cross section and resonance strengths of the 19F(p,alphagamma)16O reaction in the energy range Ep = 0.8 - 3.6 MeV"*, Z. Phys. A 357, 283-289, 1997.

48. K. Spyrou, C. Chronidou, S. Harissopulos, S. Kossionides, T. Paradelis, C. Rolfs, W. H. Schulte, L. Borucki *"Cross section and resonance strengths of the 19F(p,alphagamma)16O reaction in the energy range Ep = 0.2 - 0.8 MeV"*, Eur. Phys. J. A, 7, 79-85, 2000.

49. LISE++ *"http://lise.nscl.msu.edu"*

50. M. Arnould, S. Goriely, and M. Jorissen *"Non-explosive hydrogen and helium burnings: abundance predictions from the NACRE reaction rate compilation"*, Astronomy & Astrophysics, 347, 572-582, 1999.

51. M. E. Burbidge, G. R. Burbidge, William A. Fowler and F. Hoyle, *"Synthesis of the Elements in Stars"*, Reviews of Modern Physics, vol. 29, pp. 547-650, 1957.

52. M. Forestini, S. Goriely, A. Jorissen and M. Arnould *"Fluorine production in thermal pulses on the asymptotic giant branch"*, Astronomy & Astrophysics, 261, 157-163, 1992.

53. M. Schwarzschild & R. Harm *"Thermal Instability in Non-Degenerate Stars"*, The Astrophysical Journal, Vol. 142, p. 855, 1965.

54. M. Schwarzschild & R. Harm *"On the evolution of rapidly rotating massive white dwarfs towards supernovae or collapses*", The Astrophysical Journal, 150, 961, 1967.

55. Mesytec Nuclear Physics Tool *"https://www.mesytec.com/products/datasheets/MPR-16.pdf"*

56. Micron Semiconductors emph"http://www.micronsemiconductor.co.uk/"

57. N. Mowlavi, A. Jorissen, and M. Arnould *"Fluorine Production in Intermediate-Mass Stars*", Astronomy & Astrophysics, 311, 803-816, 1996.

58. O. B. Tarasov and D. Bazin *'PACE4"*, NIM B, 266, 4657-4664, 2008

59. P. Cuzzocrea, A. De Rosa, G. Inglima, E. Perillo, E. Rosato, M. Sandoli, and G. Spadaccini *"Quartet states in 20Ne*", Lett. Nuovo Cim. 28, 515, 1980

60. P. Cuzzocrea, A. De Rosa, G. Inglima, E. Perillo, E. Rosato, M. Sandoli, and G. Spadaccini *"Quartet states in 20Ne*", INFN/Be-80/5 4 (unpublished)

61. P. R. Fortier *"Development of a low-pressure ionization chamber for rare isotope experiments at IRIS*", M. Sc. Thesis, Saint Mary's University, Halifax, N.S., 2013.

62. P. W. Merrill, *"Spectroscopic Observations of Stars*", Astrophysical Journal, Vol. 116, p. 21, 1952.

63. R. Caracciolo, P. Cuzzocrea, A. De Rosa, G. Inglima, E. Perillo, M. Sandoli, and G. Spadaccini *"The 13.645 MeV state in 20Ne*", Lett. Nuovo Cim. 28, 515 , 1980.

64. R. Diehl, *"Gamma-Ray-Line Observations with CGRO-COMPTEL"*, 1995.

65. R. Diehl, *"Radioactive Al-26 and massive stars in the Galaxy"*, 2006

66. R. J. Stancliffe *"The evolution and nucleosynthesis of thermally pulsing asymptotic giant branch stars"*, PhD Thesis, University of Cambridge, 2005

67. R. J. Stancliffe, R. G. Izzard, C. A. Tout *"Third Dredge-up in low-mass stars"*, Monthly Notices of the Royal Astronomical Society, 356, 1-5, 2005.

68. R. Kanungo *"IRIS: The ISAC charged particle reaction spectroscopy facility for reaccelerated high-energy ISOL beams"*, Hyperfine Interactions, vol. 225, no. 1, pp 235240 , 2013.

69. R. L. Clarke and E. E. Paul *"The angular distribution and yield of the reaction* $^{19}F(p,\alpha)^{16}O$", Can. J. Phys. 35, 155, 1957

70. S. Baker and R. D. Cousins *"Clarification of the use of chi-square and likelihood functions in fits to histograms"*, Can. J. Phys. 35, 155, 1957

71. S. -C. Yoon & N. Langer *"On the evolution of rapidly rotating massive white dwarfs towards supernovae or collapses"*, Astronomy & Astrophysics 435, 967-985, 2005

72. S. Cristallo, A. Di Leva, G. Imbriani, L.Piersanti, C. Abia, L. Gialanella, and O. Straniero *"Effects of nuclear cross sections on* ^{19}F *nucleosynthesis at low metallicties"*, Astronomy & Astrophysics A46, 2014

73. S. Edwards, D. Robson, T. L. Talley, W. J. Thompson and M. F. Werby *"Multi-*

Interaction, Finite-Range, Two-Mode, DWBA Analyses of Direct Nuclear Reactions", Phys. Rev. C8, 456, 1973

74. S. Lucatello et al. *"Fluorine and Sodium in C-Rich Low Metallicity Stars*", Astrophysics. J. 729, 40, 2011

75. S. Morita *"On the reaction $^{19}F(p,\alpha)^{16}O$ in the range of bombarding energy from 2.2 to 3.4 MeV*", J. Phys. Soc. Japan 21, 2435, 1986

76. S. Rubin *"A Photographic Apparatus for Angular-Distribution Measurements*", Phys. Rev. Vol. 72, No. 12, 1947

77. V. Avrigeanu, P. E. Hodgson and M. Avrigeanu *"Global optical potentials for emitted alpha particles*", Phys. Rev. C, Vol. 49, No. 4, 2136, 1994.

78. W. A. Mahoney, J. C. Ling, A. S. Jacobson, R. E. Lingenfelter *"Diffuse galactic gamma-ray line emission from nucleosynthetic Fe-60, Al-26, and Na-22 - Preliminary limits from HEAO 3* ", Astrophysical Journal, Vol. 262, p. 742-748, 1982.

79. W. A. Mahoney, J. C. Ling, A. S. Jacobson, R. E. Lingenfelter *"Diffuse galactic gamma-ray line emission from nucleosynthetic Fe-60, Al-26, and Na-22 - Preliminary limits from HEAO 3* ", Astrophysical Journal, Vol. 262, p. 742-748, 1982.

80. X. D. Liu, M. A. Famiano, W. G. Lynch, and M. B. Tsang *"Systematic Extraction of Spectroscopic Factors from 12C(d,p)13C and 13C(p,d)12C reactions*", Physical Review C 69, 064313, 2004.

81. Y. Jading and K. Riisager *"Systematic errors in χ^2-fitting of Poisson distributions*", Nuclear Instruments and Methods in Physics Research A, 372, 289-292, 1996.

82. Y. Yamashita and Y. Kudo *"Finite-Range DWBA Analysis of (p,alpha) Reaction below the Coulomb Barrier*", Progress of Theoretical Physics, Vol. 90, No. 6, 1993.